THESIS FOR THE DEGREE OF DOCTOR OF PHILOSOPHY

Nanoconfined imidazolium ionic liquids

Long-chain ionic liquids as electrolytes and templates

Szilvia Vavra

Department of Chemistry and Chemical Engineering
CHALMERS UNIVERSITY OF TECHNOLOGY

Gothenburg, Sweden 2022

Nanoconfined imidazolium ionic liquids
Long-chain ionic liquids as electrolytes and templates

SZILVIA VAVRA

ISBN 978-91-7905-612-4

Doktorsavhandlingar vid Chalmers tekniska högskola
Ny serie Nr. 5078
ISSN 0346-718X

Department of Chemistry and Chemical Engineering
Chalmers University of Technology
SE-412 96 Gothenburg
Sweden
Telephone: +46 (0)31-772 1000

Cover
Illustrative summary of the highlights of this thesis. The central section was prepared by Ella Marushchenko for Paper II.

Printed by Chalmers digitaltryck
Gothenburg, Sweden 2022

Nanoconfined imidazolium ionic liquids
Long-chain ionic liquids as electrolytes and templates
SZILVIA VAVRA
Department of Chemistry and Chemical Engineering
Chalmers University of Technology

Abstract

Long-chain ionic liquids are attracting interest as alternatives to their short-chain analogues as electrolytes. At the same time, they are also considered as alternatives to mesogens and conventional surfactants as templates. Interestingly, the nanoconfinement of long-chain ionic liquids in a solid and porous matrix (to result in a macroscopically solid hybrid material) can in some cases result in improved properties. This is due to the different chemical and steric environment to which the ionic liquid is exposed in confinement.

In this work, the effect of nanoconfinement on the mechanism of proton transport and the capacitive behaviour of the protic ionic liquid HC_8imTFSI (1-octylimidazolium bis(trifluromethane-sulfonyl)imide) was studied. With this aim, proton conduction was investigated by broadband dielectric spectroscopy and pulsed-field gradient nuclear magnetic resonance spectroscopy, considering a mixture of imidazole and HC_8imTFSI inside hydrophobised mesoporous silica. Results show that even inside narrow pores only ca 5 nm wide, the self-diffusion of the confined ionic liquid is unrestricted, due to weak interactions between the cations and the pore walls. By contrast, when pure HC_8imTFSI was confined in the pores of hydrophilic silica, ca 3.5 nm wide, results from electrochemical impedance spectroscopy combined with equivalent circuit modelling indicated a high in-pore resistance. A further important finding is that at the in-pore protic ionic liquid/electrode interface an increased specific capacitance was measured, suggesting a higher charge density than for the interface between the electrode and the bulk protic ionic liquid.

Another aspect that has been considered in this thesis, is the ability of long-chain ionic liquids to function as a templating agent. The templating mechanism, the limitations associated to the chemical structure and the resulting pore morphology have been investigated. Results have revealed that tetradecyl- and hexadecyl-methylimidazolium cloride are suitable soft-templates for the formation of vertically aligned, uniform, channel-like pores, running through the entire thickness of a silica film deposited with the electrochemically assisted self-assembly method. By contrast, dodecyl-methylimidazolium cloride as well as the protic analogue hexadecyl-imidazolium cloride do not show a templating function under the investigated synthetic conditions. In all cases studied, the mechanism of pore formation is critically discussed.

Keywords: protic ionic liquids, surface active ionic liquids, nanoconfinement, oriented and parallel nanochannels

List of publications

This thesis is based on the following appended papers

Paper I:
An imidazolium ionic liquid as effective structure-directing agent for the fabrication of silica thin films with vertically aligned nanochannels
Szilvia Vavra, Neus Vilà, Antiope Lotsari, Alain Walcarius, and Anna Martinelli
Microporous and Mesoporous Materials, 2020, Art. nr. 110407

Paper II:
Transport properties and local structure of an imidazole/protic ionic liquid mixture confined in mesopores of hydrophobic silica
Szilvia Vavra, Khalid Elamin, Lars Nordstierna, and Anna Martinelli
Journal of Physical Chemistry C, 2021, 125(4), pp. 2607-2618

Paper III:
Surface active alkyl-imidazolium ionic liquids studied as templates to form vertically oriented pores in silica thin films
Szilvia Vavra and Anna Martinelli
Under revision for publication in the Journal of Molecular Liquids

Paper IV:
Charge transfer and electrical double layer of an amphiphilic protic ionic liquid in bulk and when confined in nanochannels
Szilvia Vavra, Elisabet Ahlberg, and Anna Martinelli
Manuscript

My contribution

Paper I:
I conceptualized the work and designed the experiments. I carried out the material synthesis and the characterization with GISAXS, Infrared spectroscopy, SEM, and cyclic voltammetry (CV). I performed data analysis and interpretation in cooperation with co-authors. I wrote the first draft of the manuscript and participated to the whole publication process.

Paper II:
I prepared the samples and carried out characterization with SEM, nitrogen adsorption, Infrared spectroscopy, SAXS, and jointly Raman spectroscopy. I performed data analysis and interpretation together with co-authors. I co-wrote the manuscript and participated to the whole publication process.

Paper III:
I conceptualized the work and designed the experiments. I carried out the material synthesis and characterization with GISAXS, Infrared spectroscopy, and cyclic voltammetry (CV). I performed data analysis and interpretation. I wrote the first draft of the manuscript and participated to the whole publication process.

Paper IV:
I partially conceptualized the work and designed the experiments with Anna Martinelli and Elisabet Ahlberg. I synthesized and verified the structure and morphology of the used thin film with GISAXS, Infrared spectroscopy, and cyclic voltammetry (CV) and performed the impedance spectroscopic measurements. I contributed to the discussion of the results and equivalent circuit modelling as well as I contributed actively during the whole process of writing the manuscript.

Additional publications not included in the thesis

Acidity as descriptor for methanol desorption in B-, Ga- and Ti-MFI zeotypes
Creci, S., Martinelli, A., Vavra, S., Carlsson, P.-A., Skoglundh, M.
Catalysts, 2021, 11(1), pp. 1–12, 97

Formulation of polyphthalaldehyde microcapsules for immediate UV-light triggered release
Eriksson, V., Andersson Trojer, M., Vavra, S., Hulander, M., Nordstierna, L.
Journal of Colloid and Interface Science, 2020, 579, pp. 645–653

Local anisotropy in single crystals of zeotypes with the MFI framework structure evidenced by polarised Raman spectroscopy
Martinelli, A., Creci, S., Vavra, S., Carlsson, P.-A., Skoglundh, M.
Physical Chemistry Chemical Physics, 2020, 22(3), pp. 1640–1654

List of abbrevations

IL	ionic liquid
SAIL	surface active ionic liquid
PIL	protic ionic liquid
EASA	electrochemically assisted self-assembly
Im-SAIL	imidazolium-based SAIL
SEM	scanning electron microscopy
FIB/SEM	focused ion-beam coupled SEM
TEM	transmission electron microscopy
SAXS	small-angle X-ray scattering
GISAXS	grazing incidence SAXS
BET	Brunauer-Emmett-Teller
BJH	Barrett-Joyner-Halenda
XPS	X-ray photoelectron spectroscopy
IR	Infrared
FT-IR	Fourier-transform Infrared spectroscopy
ATR-IR	attenuated total reflectance IR specroscopy
UV	ultraviolet
LWD	long working distance
CCD	charge-coupled device
CV	cyclic voltammetry
EIS	electrochemical impedance spectroscopy
BDS	broadband dielectric spectroscopy
CPE	constant phase element
NMR	nuclear magnetic resonance
PFG-NMR	pulsed-field gradient NMR
RF	radio frequency
CPMG	Carr-Purcell-Meiboom-Gill
SI	Supporting Information
EISA	evaporation induced self-assembly
VFT	Vogel-Fulcher-Tamman

List of chemical compounds and materials

HC_8imTFSI	1-octylimidazolium bis(trifluromethanesulfonyl)imide
$C_n$mim$^+$	alkyl-methylimidazolium (n = number of carbons in the linear alkyl chain)
$C_n$mimCl	alkyl-methylimidazolium chloride (n = number of carbons in the linear alkyl chain)
C_4mimCl	butyl-methylimidazolium chloride
C_6mimCl	hexyl-methylimidazolium chloride
C_8mimCl	octyl-methylimidazolium chloride
C_{10}mimCl	decyl-methylimidazolium chloride
C_{12}mimCl	dodecyl-methylimidazolium chloride
C_{14}mimCl	tetradecyl-methylimidazolium chloride
C_{16}mimCl	hexadecyl-methylimidazolium chloride
PF_6^-	hexafluorophosphate
BF_4^-	tetrafluoroborate
TFSI$^-$	bis(trifluromethanesulfonyl)imide
Cl$^-$	chloride
TBS	tributylsilyl group
$C_n$mimPF_6	alkyl-methylimidazolium hexafluorophosphate (n = number of carbons in the linear alkyl chain)
C_3mimPF_6	propyl-methylimidazolium hexafluorophosphate
C_4mimPF_6	butyl-methylimidazolium hexafluorophosphate
C_8mimPF_6	octyl-methylimidazolium hexafluorophosphate
$C_n$mimTFSI	alkyl-methylimidazolium bis(trifluromethanesulfonyl)imide (n = number of carbons in the linear alkyl chain)
C_2mimTFSI	ethyl-methylimidazolium bis(trifluromethanesulfonyl)imide
C_4mimTFSI	butyl-methylimidazolium bis(trifluromethanesulfonyl)imide
C_6mimTFSI	hexyl-methylimidazolium bis(trifluromethanesulfonyl)imide
C_4mimBF_4	butyl-methylimidazolium tetrafluoroborate

$C_n$mimBr	alkyl-methylimidazolium bromide (n = number of carbons in the linear alkyl chain)
C_{16}mimBr	hexadecyl-methylimidazolium bromide
MCM-41	mobil composition of matter no. 41
MCM-48	mobil composition of matter no. 48
$(RO)_4Si$	tetraalkoxysilane (R = alkyl)
$(RO)_xSiOH_{4-x}$	alkoxysilane
TEOS	tetraethoxysilane (tetraethyl orthosilicate)
$SiOH_4$	orthosilicic acid
5-C8-SiO_2	mesoporous silica microparticles hydrophobized with trioctylsilyl-groups
Im/PIL mixture	imidazole/HC_8imTFSI mixture
CNT	carbon nanotube
CTAB	cetyltrimethylammonium bromide
DTAB	dodecyltrimethylammonium bromide
TTAB	tetradecyltrimethylammonium bromide
EtOH	ethanol
ITO	indium tin oxide
$Ru(NH_3)_6Cl_3$	hexaammineruthenium(III) chloride
$K_3[Fe(CN)_6]$	potassium hexacyanoferrate(III)
FcMeOH	α-methylferrocenemethanol
$NaNO_3$	sodium nitrate
Ag	silver
Pt	platinum
Si	silicon
Cu	copper
Au	gold
AgCl	silver chloride
HDO	(O-$^2H_1$)water (semiheavy-water)
D_2O	($^2H_2$)water (heavy-water)
(Et_2NH)	diethylamine
$((BuO)_2POOH))$	di-n-butylphosphate
PET	polyethylene terephthalate

Contents

1 Introduction

Ionic liquids (ILs) have been drawing attention as ion conductive electrolytes with potential applicability in electrochemical devices, e.g. supercapacitors and fuel cells. This interest mainly comes from their intrinsically high ion density, however there are some obstacles for their commercial application. One is that many ionic liquids with suitably high ionic conductivities, typically short-chain ionic liquids, are hygroscopic and their performance deteriorates when they absorb water, e.g. from air. Thus, in the exploration of new ionic liquid groups, such as long-chain ionic liquids, one of the relevant questions is whether they show sufficient electrochemical stability also when exposed to air. Besides stability in air, another appealing aspect of research in long-chain ionic liquids is their nanosegregation into polar/apolar domains [1–5]. It has been revealed that this nanosegregation influences their structuration in bulk and in confinement, affecting properties such as ionic conductivity and double layer charge density. However, the available literature is still limited.

Another group of ILs that are also increasingly studied as ion conductive electrolytes is that of protic ionic liquids (PILs), as their synthesis is typically simpler and cheaper than their aprotic analogues [6], an important aspect for the wider use of ILs. Also, a unique ion transport mechanism is investigated in PILs, namely decoupled proton transport (also called proton hopping), which allows faster diffusion of the protons than the parental molecules [7–9]. Even though long-chain ionic liquids and protic ionic liquids are both emerging classes, the sub-class of long-chain protic ionic liquids is less studied and discussed, although combining their advantages (e.g. stability in air, affordable production, fast decoupled proton transport) is intriguing.

Another limitation in using ionic liquids in electrochemical devices is connected to the liquid nature of ILs, which can translate into leakage in the context of real applications. A common strategy to overcome this is by confinement of the IL into a solid mesoporous matrix, e.g. by formation of an IL/silica hybrid material. Next to ensuring sufficient mechanical stability, it has also been revealed that as the IL is exposed to different chemical and steric environment provided by the confinement compared to the bulk state, ionic liquids in confining space can show even improved performance. As prominent examples, higher catalytic activity and faster charge transport have been observed for confined ILs [5, 10].

The scope of this thesis is twofold. In one aspect, it aims to investigate the

effect of nano-confinement on the desired physical and chemical properties of a long-chain imidazolium PIL for use as ion conducting electrolyte. From another point of view, the focus is on studying the synthesis and properties of IL/silica hybrid materials prepared *via* electrochemically assisted self-assembly (EASA) method with using long-chain ILs as templates.

2 Background

2.1 Ionic liquids

Ionic liquids (ILs) ideally consist of ionic species only, with significant molecular asymmetry in at least one of the ions, and form a liquid phase with a melting temperature lower than 100 °C [11–13]. In ionic liquids, especially in imidazolium-based ILs, the ordering of the ions into a solid crystalline phase is hindered not only by the molecular asymmetry, typically achieved by addition of an alkyl-chain onto the imidazolium cation, but also by the hydrogen bonded network established between the cations and suitable anions, which influences the dynamic structural directionality within the ionic liquid [11, 14]. For ionic liquids, the term "designer solvents" is sometimes also used, since by choice of the constituting ions they can be designed to provide physical and chemical properties matching the requirements of the envisioned application [13, 15]. As estimatedly 10^{18} pure ionic liquids are theoretically accessible, there are vast undiscovered areas in the field and the classification of ionic liquids is still changing while established classes oftentimes overlap. In this thesis, HC_8imTFSI and the group of alkyl-imidazolium ionic liquids are studied with a specific focus on protic ionic liquids (PILs) (covered in Subchapter 2.1.1) and surface active ionic liquids (SAILs) (covered in Subchapter 2.1.2).

2.1.1 Protic ionic liquids

Protic ionic liquids (PILs) constitute a class of ionic liquids that are distinct from conventionally known ionic liquids by possessing an exchangeable proton, most commonly on the cation [6–8, 16, 17]. As an example for protic ionic liquids, the chemical structure of HC_8imTFSI is shown in Figure 2.1.

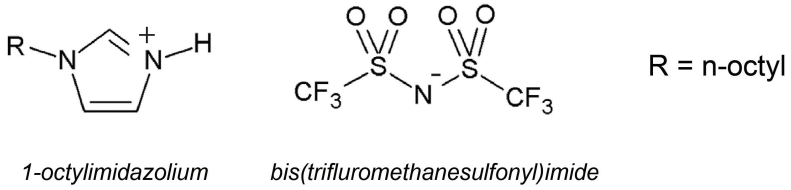

Figure 2.1: *Example of a protic ionic liquid (PIL); i.e. the 1-octylimidazolium bis(trifluromethanesulfonyl)imide, HC_8imTFSI.*

Besides the difference in chemical structure and related properties, in general, PILs are considered as cheaper alternatives to their aprotic analogues (in which in place of the proton another chemical group, typically an alkyl-group, is attached to the nitrogen of the heterocycle). PILs are also defined as ionic liquids formed by proton transfer from a Brönsted acid (HA) to a Brönsted base (B) with sufficiently high pKa difference between them, necessary for the formation of ionic species (A^- and HB^+) [6, 18]:

$$HA + B \rightleftharpoons A^- + HB^+$$

In the context of developing electrochemical devices that utilise proton conduction, there is a high interest in PILs, since the presence of the exchangeable protons offer the possibility to contribute to the overall proton conduction *via* the Grotthuss mechanism (also called proton hopping), in addition to the vehicular type of charge transport typical of liquid electrolytes [7–9]. During the vehicular type of charge transport, the proton is chemically bound to the cation and transfers together with it [8]. Therefore, in this case the ionic conductivity is limited by the diffusion rate of the cationic species [8]. However, when provided an appropriate hydrogen bonded network in the PIL, the exchangeable protons can move to acceptor sites *via* the Grotthuss mechanism, and by means of a dynamic reorganisation of the involved hydrogen bonds, much faster than the diffusing parent molecules [7–9]. In the case of alkyl-imidazolium based PILs, the imidazolium head of the cation can provide proton donor sites, while proton acceptor sites can be included, for example, by the addition of amphoteric molecules (e.g. imidazole) [5, 7, 19].

2.1.2 Surface active ionic liquids

Surface active ionic liquids (SAILs), showing enhanced amphiphilic nature, are drawing increasing interest as alternatives to mesogens and conventional surfactants, just as well as alternatives to short-chain ionic liquids [3, 20–23]. As an example for surface active ionic liquids, the chemical structure of C_{16}mimCl is shown in Figure 2.2, the cation having an imidazolium "head", just like a conventional imidazolium ionic liquid, and an alkyl "tail", just like a conventional surfactant. As the review study by Cao et al. has shown, imidazolium-based SAILs (Im-SAILs) can provide higher surface activity and more diversified aggregation behaviour compared to conventional surfactants [21]. At the same time, Im-SAILs are also studied for applications already at focus for conventional imidazolium based ionic liquids, for example as electrolytes and catalysts [3, 22, 24].

In SAILs, the elevated amphiphilicity is most commonly achieved by having a longer alkyl chain on the cation and upon increasing the chain length the behaviour of the ionic liquid approaches that of surfactants. Before focusing only

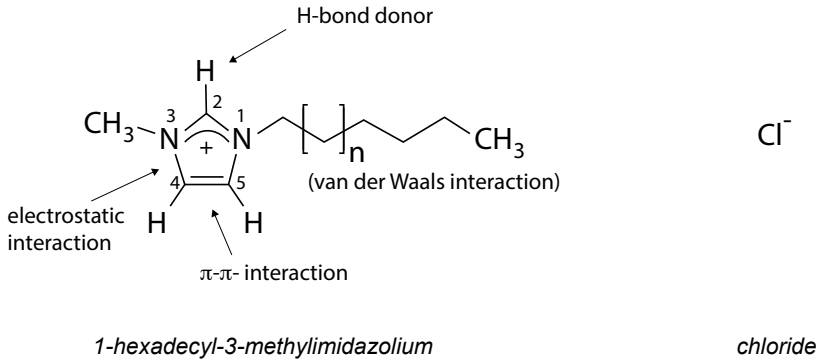

Figure 2.2: *Example of a surface active ionic liquid (SAIL); i.e. the 1-alkyl-3-methylimidazolium chloride, C_{16}mimCl. The interactions this cation is able to establish are also indicated. Created based on reference [25].*

on SAILs, it is worth to take a look at the melting temperature (T_m) of $C_n$mim$^+$-based ionic liquids, shown in Figure 2.3, which is closely related to the established intermolecular interactions. In the region of low number of carbon atoms in the alkyl chain, the chain must be long enough to reduce Coulombic forces (i.e. the electrostatic interactions between the charged ions) and disrupt lattice packing to form an ionic liquid instead of a salt. Accordingly, in this region the increase of the

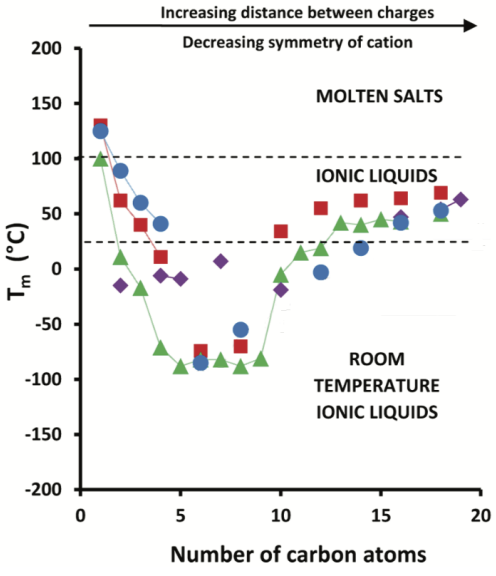

Figure 2.3: *Melting temperature (T_m) of $C_n$mim$^+$-based ionic liquids with different chain length and anions: hexafluorophosphate (PF_6^-, red square), tetrafluoroborate (BF_4^-, green triangle), bis(trifluromethanesulfonyl)imide ($TFSI^-$, purple diamond), and chloride (Cl^-, blue circle). The figure is reproduced from reference [14] with permission from the American Chemical Society.*

chain length results in a decrease of the melting point [14]. Another interesting aspect is that by increasing the chain length, nanostructuration in the bulk ionic liquid can be observed with the formation of dynamic polar and apolar domains, see Figure 2.4 [14, 26]. Such structuration can be characterised with X-ray scattering, with which the chain-chain segregation has been observed in imidazolium ionic liquids $C_n$mimCl with $n \geq 4$ [1]. In addition, Abdurrokhman et al. have found the same trend in the protic analogue HC_nimTFSI ionic liquid series with $n \geq 4$ [2]. Within the subgroup of alkyl-imidazolium ionic liquids coupled with the chloride anion, C_6mimCl is considered to be the "transitional ionic liquid" as it shows surface activity but no self-assembly in water [20, 27]. Accordingly, in this thesis, imidazolium ionic liquids with an alkyl chain equal or longer than the hexyl ($n = 6$) are referred to as long-chain ionic liquids or SAILs, interchangeably. Moreover, Figure 2.3 shows that by further increasing the chain length, beyond the minimum point, T_m increases reflecting the increase in cohesive interactions between the alkyl chains, like in linear alkanes [14]. In fact, $C_n$mimCl ionic liquids with an alkyl chain equal to an octyl or longer ($n \geq 8$) form micelles in water and, for a sufficiently long chain, Im-SAILs can even pack into liquid crystalline phases ($n \geq 10$) [14, 21, 23, 28, 29].

The ability of Im-SAILs to assemble can be extremely useful for applications. As alternatives to surfactant templates, Im-SAILs have been used as soft-templates for the synthesis of mesoporous inorganic matrices, e.g. mesoporous silica [30, 31]. Meanwhile, as alternatives to short-chain ionic liquids, the use of SAILs as electrolytes is highly motivated by their non hygroscopic nature, which can be compared to the case of many short-chain ionic liquids that readily absorb water from air resulting in poorer electrochemical properties. Even though ionic conductivity decreases in Im-SAILs with the increase of chain length, the amphiphilic nature can still be advantegous [2, 3]. As a prominent example, the experimental

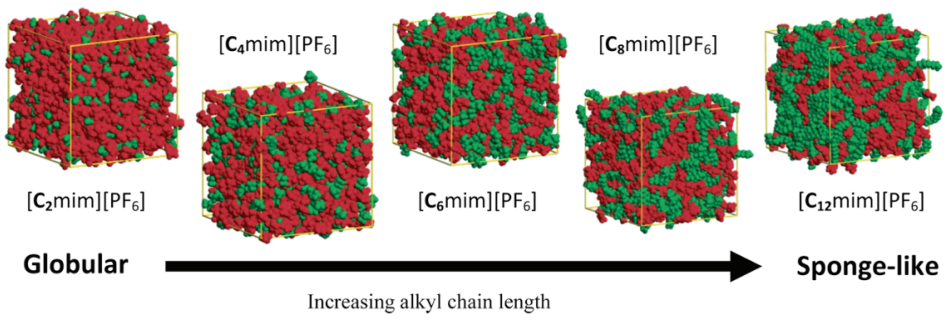

Figure 2.4: *Snapshots of the bulk structure of $C_n$mimPF_6 ionic liquids (n = 2–12). The red domains consist of anions and imidazolium rings of the cations, while the green domains show the nonpolar alkyl chains. The figure is based on reference [26] and reproduced from reference [14] with permission from the American Chemical Society.*

study by Su et al. has shown that the amphiphilic assembly of Im-SAILs at the electrode surface leads to characteristic maxima in the differential capacitance [3].

2.2 Nanoconfinement

Fluids confined in nanometre-scaled space can show different structure and properties compared to their bulk state. This has generated high interest in a broad range of fields that are often far from each other, yet the knowledge of confinement effects can be interchangeable [5, 15, 32–37]. The diversity of systems in which nanoconfinement has key importance is also demonstrated by some well-known examples. In biological ionic channels, fast transfer of ions and water has been observed to proceed in the form of single molecular strand; similarly, water confined in artificial CNTs (carbon nanotubes) has shown enhanced diffusion and wire-like ordering [38]. Besides being of high scientific interest, investigating nanoconfinement effects is also relevant for technical applications, for example in catalysis [10, 34, 38], energy storage [24, 39] and separation [38, 40].

IL/silica hybrid materials, in which the ionic liquid is confined in the solid porous silica matrix at the nanometre scale (by definition smaller than 1 μm), have been synthesised and studied in different contexts [41]. From a rather practical point of view (e.g. in heterogeneous catalysis, solid-phase micro-extraction and ion-conductive membranes), confinement of ionic liquids into a solid porous matrix is a strategy to overcome the limitations associated to the liquid nature of ILs, in practice leakage. In some studies, IL/silica hybrid materials are also called supported ILs [10, 15, 24, 40, 42, 43]. At the same time, due to the different chemical and steric environment provided by the confinement, it has been proven that ionic liquids can show improved performance upon confinement, for example higher catalytic activity and faster charge transport of ILs have been observed in porous silica [5, 10, 15]. In addition, some IL/silica hybrid materials can serve as suitable model systems for studying structures and properties in nanoconfinement. This is because silica is a versatile material, which can be prepared with known methods that allow modifying its chemical properties as well as tuning its pore morphology; in addition, silica can be prepared to achieve different macroscopic forms, like gels or films [24, 38, 40, 42, 44, 45].

2.2.1 Structure and properties of ionic liquids in confinement

As an initial simplified concept, one can assume that molecules in a pore partition into two layers: (i) a surface layer which is affected by the interactions with the pore wall and (ii) an inner layer at the centre of the pore which is independent from the surface, see Figure 2.5 [15]. While the inner layer shows bulk-like structure and properties, the molecules close to the pore wall can show different structuration and changed physical and chemical properties compared to that of bulk molecules.

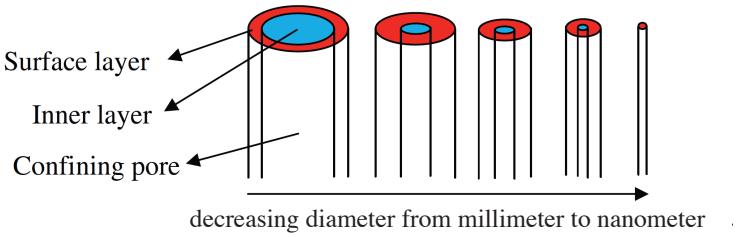

Figure 2.5: *Schematic of confined liquids in a cylindrical pore with a decreasing pore-size approaching the nanometre scale. The figure is reproduced from reference [15] with permission from Elsevier.*

By decreasing the size of the confining space to the nanometre range, the molecules of the surface layer become more dominant in determining the overall properties.

In the case of nanoconfined ILs, the proportion of the ions that are affected by the pore wall and the ions with bulk-like structuration and properties has been shown to be dependent on the intrinsic nano-structuration of the IL [15, 39], the shape and size of the pore [15, 39], and the chemistry of the pore wall [5, 46]. Similar to the IL/silica hybrid materials discussed in this thesis, Elola et al. have simulated the structuration of a long-chain ionic liquid, C_6mimTFSI,

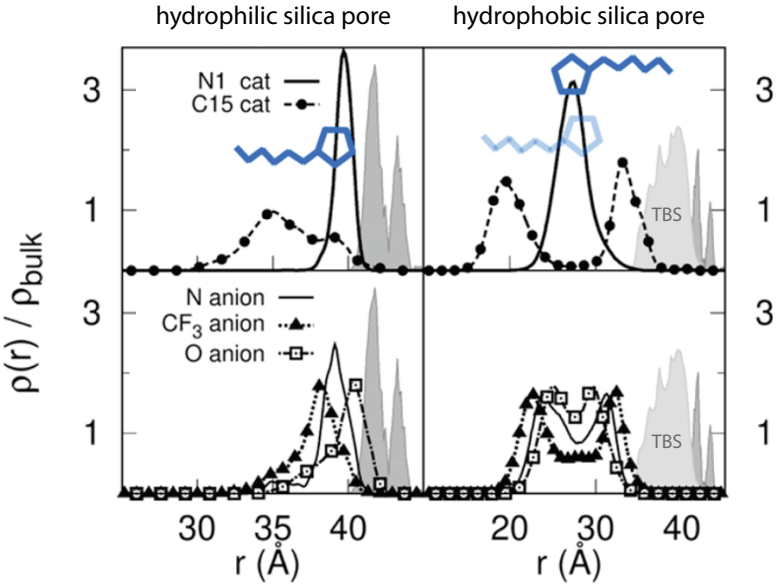

Figure 2.6: *Local density distribution for selected atoms: N and C of the cation located in the imidazolium ring and the end of the alkyl chain, and N, CF_3, and O sites of the anion. The top panels correspond to cation sites and bottom ones correspond to the anion ones. Left and right panels correspond to systems conaining hydrophilic and hydrophobic silica pore, respectively. Reprinted (adapted) with permission from reference [46]. Copyright 2022 American Chemical Society.*

in hydrophilic and hydrophobic silica pores (the hydrophobic silica was realised with the addition of tributylsilyl groups), as summarised in Figure 2.6. As their results show, the hydrophilic character of the pore resulted in the accumulation of the imidazolium heads at the pore wall, while in hydrophobic pores the cations organise with their alkyl tails pointing toward the wall. As it is shown by the density distributions, the population of cations and anions returns to the bulk value within a few nanometres.

As confinement affects local structure and properties, a wide range of physical and chemical properties of ILs have been studied in nanoconfinement. For this, various experimental and computational studies have been used, revealing that nanoconfined ionic liquids show changed phase transition temperatures, thermal stability, and molecular dynamics [15, 39]. Ionic conductivity and capacitance are among the most studied properties of nanoconfined ILs and are, in this thesis, discussed in more detail in Subchapter 2.2.2 and Subchapter 2.2.3, respectively.

2.2.2 Charge transport in ionic liquids in confinement

The charge transport properties of both aprotic and protic ionic liquids have been studied in nanoconfinement [5, 24, 37, 39, 47, 48]. Even though charge transfer of PILs can show differences from that of aprotic ionic liquids, because the vehicular is the typically dominant mechanism in both PILs and aprotic ionic liquids it can be beneficial to discuss their charge transport properties comparably. Besides, they show similar nano-structuration in bulk [2, 14] and it has been revealed also that their local structure in nanoscale confinement can be influenced similarly by the chemistry of the pore wall [5, 37, 47, 48].

In the case of IL/silica hybrid materials consisting of imidazolium ionic liquids, diffusivity and network of hydrogen bonds within the pores have been primarily studied for the case of aprotic ionic liquids [15, 37, 39, 46–48], while only a limited number of contributions have focused on the PIL analogues [5, 48, 49]. In common to aprotic and protic ionic liquids based on the alkyl-imidazolium cation is that both show nanosegregation into polar and non-polar domains when the alkyl chain on the cation is equal or longer than the butyl due to the increased amphiphilic nature of the cation [1, 2, 14]. Also, their ionic conductivity is similarly affected by the chemistry of the pore walls in silica. When the silica walls are chemically untreated, the non-bridging oxygens (-SiO$^-$) and silanol groups (-SiOH) covering the surface of the wall, interact with the polar domains of the ionic liquid (primarily with the imidazolium head) resulting in a drastic decrease of self-diffusivity and ionic conductivity, which has been observed in the case of both aprotic and protic long-chain alkyl-imidazolium ionic liquids [5, 37, 46–48]. In contrast, hydrophobisation of the silica walls leads to that the non-polar domains of the cation (i.e. the alkyl chains) assemble at the pore wall instead. Such structure is schematically shown in Figure 2.7, for the case of the HC$_8$imTFSI/imidazole mixture confined

in hydrophobised silica. As there are only weak dispersion forces between the alkyl chains of the cations and the hydrophobic groups covalently attached onto the silica walls, unrestricted high self-diffusivities of the ions have been observed in both aprotic and protic long-chain alkyl-imidazolium ionic liquids confined in hydropobised mesoporous silica [5, 37, 47, 48]. In addition, Garaga et al. have reported that the HC_8imTFSI/imidazole mixture shows not only a higher cation diffusivity than in bulk, but also an enhanced decoupled proton motion when the HC_8imTFSI/imidazole mixture is confined in hydrophobised mesoporous silica, highlighting an important additional charge transport mechanism of PILs being enhanced in confinement [5].

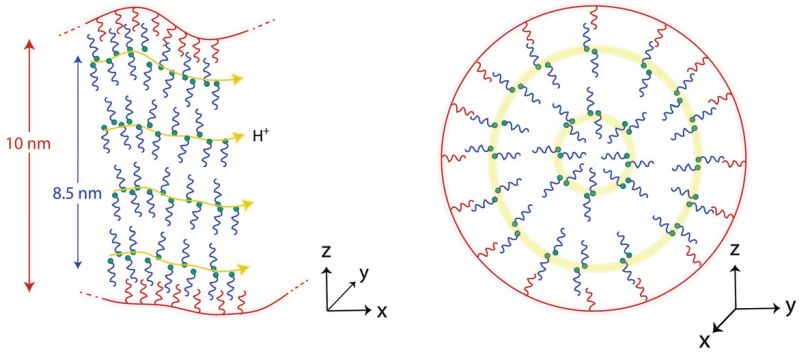

Figure 2.7: *Schematic picture of the nanostructuration in the HC_8imTFSI/imidazole mixture when confined in the nanopores of hydrophobic silica (achieved by covalent bonding of trioctylsilyl-groups onto the pore wall), showing the molecular organisation along the pores (left) and across a pore section (right). The figure is reproduced from reference [5] with permission from The Royal Society of Chemistry.*

2.2.3 Capacitance of ionic liquids in confinement

Ionic liquids are highly researched as electrolytes for supercapacitors and other electrochemical devices [16, 50]. For use in supercapacitors, primarily short-chain aprotic ionic liquids have been studied. The main reason for not considering PILs as electrolytes for supercapacitors is that aprotic ILs show larger electrochemical window while PILs, possessing an exchangeable proton, can be reduced at a less negative cathodic potential [50, 51]. Despite this, there is a growing interest towards PILs for use as capacitor electrolytes, because their synthesis is typically simpler and more affordable than in the case of aprotic ILs; also, while PILs are safer than organic solvent-based electrolytes and still provide wider electrochemical windows than aqueous electrolytes [6, 50, 51]. Another group of ILs, namely surface active ionic liquids (SAILs) are also drawing interest for their distinct ion structuration at the electrode/electrolyte interface, which is not fully understood yet and the relevant literature is very limited. Moreover, even though the ionic

conductivity of SAILs are much lower than that of their short-chain analogues, they have the advantage of not absorbing moisture from air [2].

The high charge density of ILs make them unique among ion-conductive electrolytes; at the same time, however this leads to the formation of electrical double layers that can not be described by classical models. In other words, the assumptions of classical models do not hold; ion-ion interactions are not negligible (in fact, they fundamentally determine the physical and chemical properties of ILs) and the ions can not be treated as point charges [50, 52–54]. Instead, to determine the structure of the double layer theoretical modelling and surface-sensitive measurements are used [3, 52, 54, 55]. With them, nanoscale structuration of ILs at charged electrode surfaces has been observed. At low potentials, ILs show an overscreening effect, during which the first layer of counter-ion contains more counter-charge than is on the electrode which leads to a double layer structure that consists of an alternation of counter-ion-rich and co-ion-rich layers until a point where the bulk structure is recovered. At higher potentials, the first adsorbed layer can not contain enough counter-ions to balance the electrode charge, and instead of forming alternating layers of counter- and co-ions, accumulation of the counter-ions proceeds, also referred to as the crowding regime [52–54].

In the case of SAILs, the structure of the electrical double layer at the electrode has been studied only experimentally and in a very limited number of studies. Su et al. have revealed that the differential capacitance measured as a function of the applied voltage depends on the chain length in the case of $C_n$mimPF_6 ionic liquids [3]. While C_3mimPF_6 and C_4mimPF_6 show a "bell"-shaped curve, C_8mimPF_6 shows a "camel"-shaped differential capacitance curve [3]. The authors related the capacitance maxima to changes in the structuration of the ions at the electrode surface; the first maximum (at around -0.6 V vs Pt) has been associated to the formation of stripe-like double-row adsorbates of assembled imidazolium cations (*via* polar/apolar nanosegregation with the alkyl chains pointing towards each other in a stripe-like assembly laying on the electode surface). By increased voltage, a second maximum (at -1.6 V vs Pt) has been observed only in the case of C_8mimPF_6 that has been assigned to an order-disorder structure transformation [3].

The electrical double layer of ILs in confined space has been investigated more extensively for systems containing short-chain ionic liquids, while in the case of SAILs the effect of confinement on capacitance has been studied only by computational approaches [4, 50, 55, 56]. In the case of short-chain ionic liquids, Largeot et al. have shown for the case of C_2mimTFSI that, similar to conventional electrolytes, the sieving effect can be observed also with ILs, namely that the specific capacitance reaches a maximum when the pore size of the porous electrode is very close to the size of the ions [56]. Focusing on the effect of increased chain length, Yang et al. have shown for the case of $C_n$mimTFSI (n = 2, 4, 6) ionic liquids, with the use of classical density functional theory, that ionic liquids with a longer

chain showed a higher differential capacitance at low potentials (i.e. smaller than ±0.5 V) in electrodes having 4 nm wide pores [4].

2.3 Nanoscale templating

Besides as alternatives to short-chain ionic liquids, SAILs are also considered as alternatives to conventional surfactants. Since they can show self-organisation in dissolved or in pure form, SAILs can be used as soft-templates in the synthesis of mesoporous materials [21, 30]. Zhou et al. have already showed that not only SAILs can form mesoporous structure, but as an exceptional case the ionic liquid C_4mimBF_4 too [57]. Thus, investigating the templating function of ILs is highly motivated by the idea of preparing ionic liquid-based hybrid materials in a one-step process. In a larger context, this may open up the possibility to synthesise IL-based functional hybrid materials in which the organic ionic liquid provides an added function besides templating the inorganic matrix [30, 31, 40].

2.3.1 Sol-gel synthesis of silica

Templating of silica with a molecular soft-template is commonly carried out in parallel with the formation of a silica network *via* the sol-gel synthesis, during which the amorphous silica network is formed by the hydrolytic polycondensation of tetraalkoxy silane precursors [58]. The sol-gel method has several advantages, for example that both chemical and physical parameters can be used to control the reaction sequence, allowing to tune the properties of the final product [58, 59]. The basic steps of the synthesis using tetraalkoxy silanes are (i) hydrolysis of the precursor resulting in the formation of silanol groups and (ii) condensation of the monomers having these silanol groups that results in the formation of siloxane (Si-O-Si) linking groups and by further condensation an extended silica network [59]. The mechanism and reaction rate of hydrolysis in aqueous media are highly dependent on the pH; in the case of tetraalkoxy silanes both acid and base catalysed reactions proceed through the S_N2 mechanism, Figure 2.8.

The acid-catalysed hydrolysis is initiated by the protonation of the alkoxide group that results in the silicon atom being more electrophilic and susceptible to nucleophile attack by the surrounding water molecules. On the next step, water - acting as a nucleophile - attacks the silicon centre forming a bimolecular intermediate, typical for the S_N2 mechanism. This transition state is consumed by displacement of alcohol along with the inversion of the silicon tetrahedron. In addition, base-catalysed hydrolysis also proceeds by the S_N2 mechanism, but with a different nucleophile attack and intermediate, therefore the inversion of silicon tetrahedron occurs in this reaction pathway as well. As both acid and base can catalyse the hydrolysis, reaction rates are increasing at both pH extremes, as presented in Figure 2.8 [59].

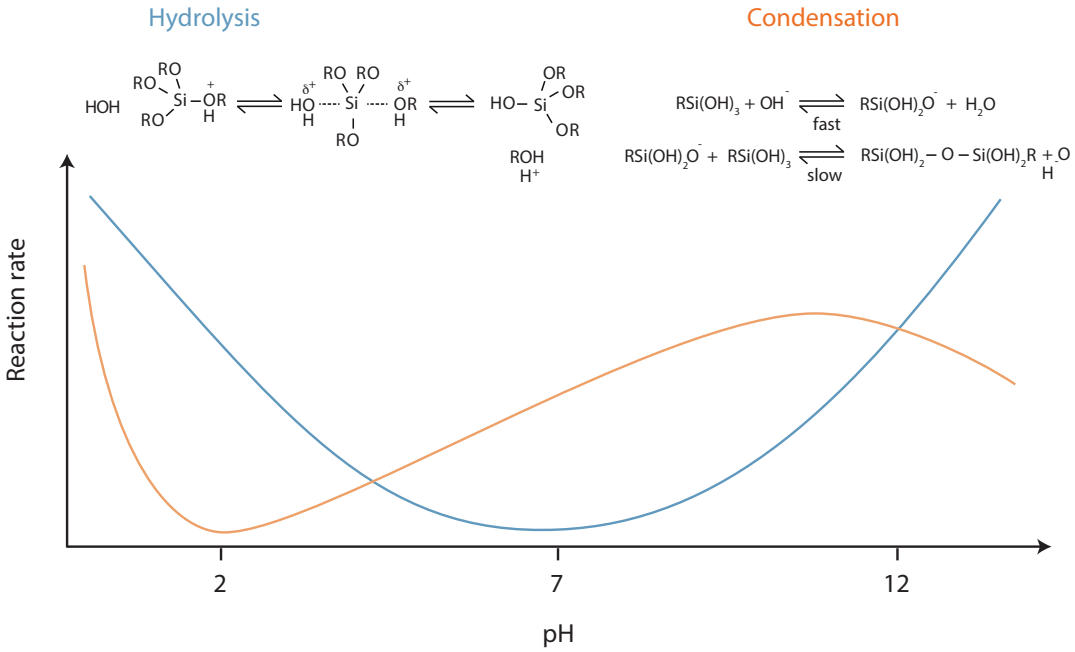

Figure 2.8: *Reaction mechanism of acid catalysed hydrolysis and base catalysed condensation during sol-gel silica synthesis from tetraalkoxy silanes [59]. The plot shows the pH dependence of the reaction rates of hydrolysis and condensation reactions, recreated based on reference [60].*

The condensation reaction of the hydrolysed silica precursor is dependent on the pH as well, see Figure 2.8. Above the isoelectric point of silica (>pH 2-4.5), the silanol group is deprotonated. Therefore, the deprotonated silanol can act as a nucleophile and attack on a neutral silicate species. The condensation rate shows a maximum at basic pH and a minimum rate near the isoelectric point. It is generally believed that during the base-catalysed condensation mechanism penta- or hexacoordinated silicons are formed as intermediates or transition states. In addition, pH also has an effect on the growth of the silica products; at acidic pH and pH = 7-10 in the presence of salts, a three-dimensional network of amorphous silica is formed, while in a basic solution the growth of nanoparticles has been observed [59].

2.3.2 Ionic liquids as templates

Even though nano-structuration can occur in ILs at different extents depending on the chemical structure, using ionic liquids as soft-templates during the synthesis of mesoporous silica is not straightforward. Experiments have shown that the intrinsic structuration of the ionic liquids can not always be preserved for the formation of mesopores within the silica network [1, 2, 61, 62]. Moreover, coop-

erative interaction between the template and the silica-network forming species is essential to achieve a desired mesoporos structure [61, 62]. As a well-known example, despite of the present supramolecular (e.g. ion cluster) and mesoscopic range (e.g. micro-phase separation, hydrogen-bond network) on structurations in imidazolium ionic liquids, using them as the co-solvent during the sol-gel synthesis of silica typically results in the formation of ionogels (when the alkyl chain of the cation is shorter than dodecyl). Ionogels contain non-porous silica particles that form disordered mesopores and macropores, an example is shown in Figure 2.9 a [14, 25, 63, 64]. However, Zhou et al. have reported a very unique exception: C_4mimBF_4, which has successfully been used as molecular soft-template in the sol-gel synthesis of mesoporous silica, forming a monolith with a sponge-like pore structure, see Figure 2.9 b [62]. The templating mechanism was explained by what the authors called hydrogen bond-co-π-π stack mechanism involving hydrogen bonds formed between the $[BF_4]^-$ anions and the silanol groups of silica and the presence of π-π stack interactions between the neighbouring imidazolium rings of the cations. Accordingly, in the obtained mesoporous monolith the $[BF_4]^-$ anions are assumed to be located along the pore walls and the imidazolium rings of the cations next to the anions due to electrostatic attractions at the same time stacked parallel to each other due to π-π interactions and their hydrophobic alkyl chains pointing towards the centre of the pores [62].

Among imidazolium ILs there are more, yet still limited in number, examples of syntheses with Im-SAILs being used as soft-templates to obtain mesoporous silicas. Having water as solvent, amphiphilic ionic liquids that show amphiphilic self-assembly in aqueous medium, are more suitable soft-templates for the formation of mesopores with a well-defined pore width [31, 66]. Templating with $C_n$mimBr ionic liquids has showed a chain length dependence in forming worm-

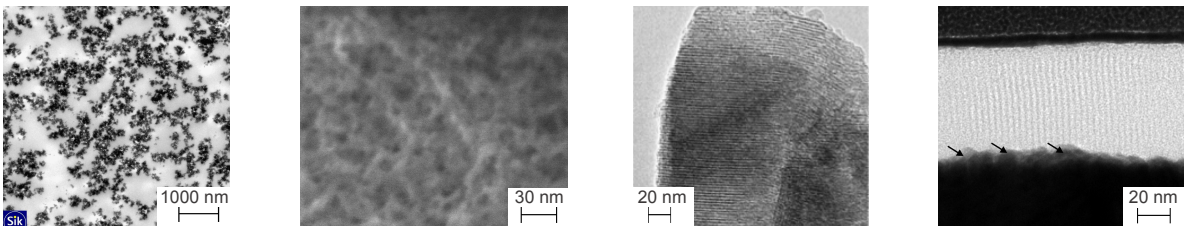

Figure 2.9: *IL-templated mesoporous silicas. a) SEM of a $C_6mimTFSI$-based ionogel. The image is reproduced from reference [64] with permission from The Royal Society of Chemistry. b) SEM image of a C_4mimBF_4-templated mesoporous monolith synthesised according to reference [62]. c) TEM image of a $C_{16}mimBr$-templated mesoporous silica particle. The image is reproduced from reference [65] with permission from Springer. d) A $C_{16}mimCl$-templated mesoporous silica thin film [31]*

like (n = 8-12) and hexagonal (n = 14-16) mesoporous silica particles, see Figure 2.9 c [65]. With C_{16}mimCl as soft-template, MCM-type hexagonal (MCM-41, with p6mm symmetry) and cubic gyroid (MCM-48, with Ia3d symmetry) silica particles could be obtained by tuning the concentration of the IL in the aqueous reaction solution [66]. Besides particles, $C_n$mimCl ionic liquids were able to form a lamellar pore structure in monolithic mesoporous silica, with the pore diameter being determined by the varying alkyl chain length ranging from 1.2 nm (n = 14) to 1.5 nm (n = 18) [57, 67]. As discussed in Paper I and III, $C_n$mimCl ionic liquids are also suitable to form vertically-aligned and hexagonally ordered discrete nanochannels in silica thin films preapred with the EASA method, shown in Figure 2.9 d.

Despite the increasing number of publications on SAILs as soft-templates, the underlying templating mechanism during the sol-gel synthesis of mesoporous silica is often not studied nor even discussed. Fortunately, C_{16}mimCl has many similarities with CTAB (cetyltrimethylammonium bromide), which comes handy in experimental design and basic understanding. However, there are also relevant differences between them, namely that in Im-SAILs the imidazolium head, being an aromatic heterocycle, is capable of establishing further interactions [25]; as illustrated in the schematic of Figure 2.2. Besides electrosctatic attraction, the imidazolium heads are able to establish hydrogen bonds and π-π interactions between each other [25, 61, 66]. In addition, the imidazolium heads are able to arrange parallel to each other resulting in a higher packing density and a tendency to form mesostructures with a lower curvature [61, 66]. However, it is important to note that the contribution of these additional interactions is weak, and in fact CTAB (in which the binding affinity of the bromide ion is high) and C_{16}mimCl show very similar critical micellar concentrations (c.m.c.) and enthalpies of micellisation [61].

2.3.3 Electrochemically assisted self-assembly (EASA)

For the preparation of soft-templated mesoporous silica thin films typically two robust techniques are used, both of them being based on sol-gel synthesis. These are the (i) evaporation-induced self-assembly (EISA) and the (ii) electrochemically assisted self-assembly (EASA) [68]. A huge advantage of the EASA method is that vertical aligment of mesochannels with respect to the substrate can be achieved during an extremely rapid synthesis (in a time scale of seconds). However, a limitation is the required conductivity of the substrate.

The preparation of the mesoporous silica film with the EASA method is schematically shown in Figure 2.10. First, an aqueous solution is prepared (in which the solvent is an EtOH:water = 1:1 mixture) containing the tetraalkoxy silane precursor (TEOS) and the template (CTAB or Im-SAIL) [31, 69]. Then, after setting acidic pH (pH = 3), the precursor is let to be hydrolysed *via* acid catalysis [70].

Then, the solution is poured into a three-electrode cell. The cell contains a working electrode, a counter electrode, and a reference electrode. The deposition of the silica film proceeds by applying a cathodic potential to the working electrode, which results in an electrochemically induced pH increase at the working electrode-solution interface. The produced hydroxyl ions catalyze a rapid condensation of silica onto the electrode surface, see also Figure 2.8. As the pH change proceeds in the close vicinity of the working electrode, acceleration of the polycondensation happens only close to the electrode surface [68]. Combined with the presence of the soft-template, mesostructured silica thin film with pore channels oriented perpendicular to the electrode surface can be synthesised in this way [68]. As proposed by Herzog et al., hydroxyl ions are produced at the flat electrode surface concomitant to the orientation of the cationic surfactant [70].

The working electrode can be chosen according to the application in mind and various materials have been reported with different morphologies, e.g. ITO surface, and other conducting supports like macro discs or non-flat supports like gold CD-trodes and microelectrodes (e.g. platinum wires, platinum microdiscs, and carbon fibers) [70, 71]. Next to the preparation of discrete nanochannels in a hexagonal arrangement, another mesostructural order, namely three-dimensional cubic arrangement could also be observed (in this case the template was CTAB) [68].

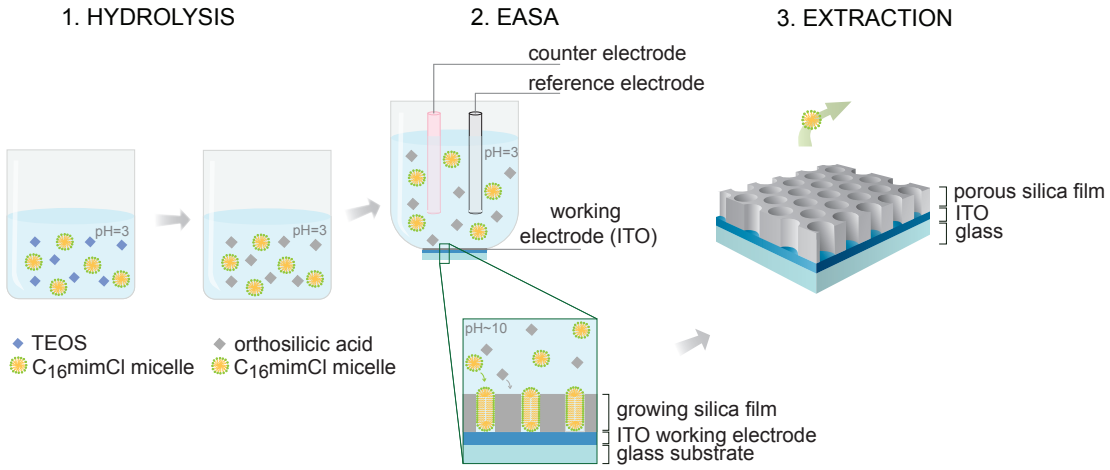

Figure 2.10: *Schematic illustration of the subsequent steps involved in the EASA synthesis method, here shown in the case of C_{16}mimCl-templated mesoporous silica thin films.*

3 Characterisation and methods

3.1 Electron microscopy

3.1.1 Scanning electron microscopy (SEM)

In scanning electron microscopy (SEM), a focused beam of high-energy electrons, hitting the material, generates a variety of signals at the surface of the studied sample specimen [72]. For imaging, the acceleration voltage of the incident electron beam is typically set to 2–25 keV to obtain the scanning electron micrograph (i.e. the image) for which most often secondary electrons are collected. Secondary electrons are emitted from the sample as a result of interaction of the primary electron beam with the sample and as the energy of secondary electrons is relatively small (several 10 eV) only those generated from the upper surface of a few nanometres are able to escape from the sample and be collected. Thus, the use of secondary electrons for imaging is ideal for examining topography. For insulating samples, like silica, sputter coating with a good conductor (e.g. palladium or gold) is necessary to avoid charging effect (accumulation of electrons on the sample surface).

The SEM images presented in this thesis and in Paper I were obtained with a JEOL 7800F Prime microscope in the secondary electron imaging mode. The samples were coated with palladium before imaging, for which an EMITECH K550x sputter coater was used. Cross sectional images of thin films were prepared by breaking the substrate after sputtering then imaging the broken surface using a specific tilted SEM stage.

3.1.2 Transmission electron microscopy (TEM)

In transmission electron microscopy (TEM), the incident beam of electrons is accelerated to an energy higher than in SEM, typically to hundreds of keV [72]. This incident beam of electrons is focused by an array of magnetic lenses into a small probe that is transmitted through the sample and an image of the specimen is generated from the collected transmitted electrons. TEM is an excellent tool for imaging nanostructures as the theoretical resolution limit is extremely low due to the small de Broglie wavelength of the incident electrons which is in the range of only 10^{-2} Å. In practice, the resolution of TEM instruments is much lower, but due to rapid instrumental improvement by date subnanometre resolution can be

achieved. As a rule of thumb, an important requirement from the sample is that it should not be thicker than 100 nm. In case of thin films, like the ones studied in this thesis, a cross-sectional sample with the thickness of tens of nanometres can be prepared with lift-out technique using FIB/SEM (focused ion-beam coupled SEM). Basically, first a cross-sectional cut out of the film is prepared with ion-beam milling then this cut out is attached to a copper TEM grid with deposited platinum.

The top view TEM micrographs of thin films presented in this thesis and Paper I were obtained on samples prepared by placing a droplet of an aqueous suspension of the extracted, grinded films on a carbon-coated Cu TEM grid that were then dried overnight under ambient conditions. The TEM experiments were performed on a FEI Tecnai T20 instrument operating at 200 kV. The obtained images were processed with the Digital Micrograph software. For the cross-sectional TEM study, a sample of a thin film was prepared with the lift-out technique using a FEI Versa Dual FIB/SEM instrument.

3.2 Small-angle X-ray scattering (SAXS)

3.2.1 Transmission small-angle X-ray scattering

Small-angle X-ray scattering (SAXS) is suitable to characterise structural features with typical dimensions in the nanometre range, based on the scattering X-ray signal generated by fluctuations in the average electron density on scales significantly larger than that of atomic radii [73]. The typical measurement setup with the so-called transmission geometry is schematically shown in Figure 3.1. The intensity of the scattered X-ray at a point, defined by the wave vector q, is proportional to the following variables:

$$I(q) \propto NV^2(\Delta\rho)^2F(q)S(q) \tag{3.1}$$

where N is the number of scattering objects with volume V, $\Delta\rho$ is the electron-density contrast, $F(q)$ is the form factor, $S(q)$ is the structure factor [74]. In our studies, information on the size of scattering objects were obtained from their diffraction peaks extracted from 2D scattering patterns based on Bragg's law. Thus, the size of a structural feature was determined from the calculated correlation length, d, where q_{max} is the position of the diffraction peak:

$$d = 2\pi/q_{max} \tag{3.2}$$

Small-angle X-ray scattering (SAXS) measurements in transmission mode, presented in this thesis and Paper II were performed on a Mat:Nordic instrument from SAXSLAB/Xenocs. The X-ray beam was produced by a Cu-radiation source and focused with a Micro-Max 003 X-ray generator from Rigaku. The dector was

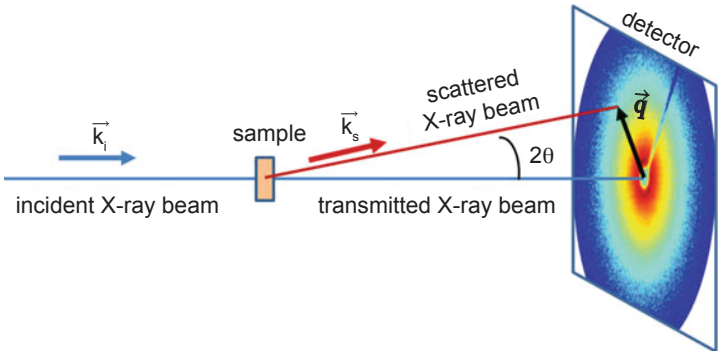

Figure 3.1: *Schematic of a SAXS experiment using the transmission geometry. The figure is reproduced from reference [75] with permission from Springer.*

a Pilatus 300K from Dectris. The X-ray scattering patterns of samples containing bulk ionic liquids and mesoporous silica particles were measured in quartz capillary with an inner diameter of 0.15 mm. The calibration was done with silver behenate. The sample to detector distance was 134 mm and the exposure time 480 s. The collected 2D scattering patterns were transformed into 1D scattering graphs using the SAXSGUI (Rigaku) software.

3.2.2 Grazing-incidence small-angle X-ray scattering (GISAXS)

In grazing-incidence small-angle X-ray scattering (GISAXS) mode the X-ray beam impinges on the sample surface under a shallow incident angle (typically a few tenths of a degree) [74]. Then, the X-ray photons scattered by the sample are col-

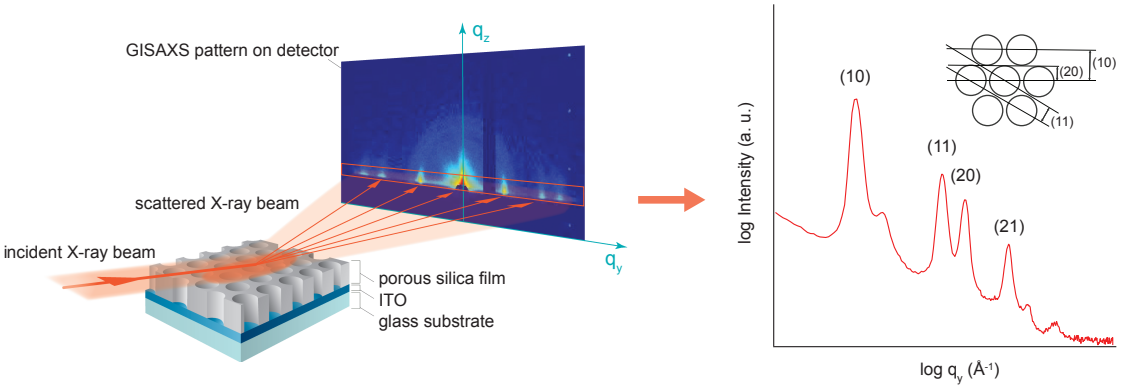

Figure 3.2: *Left: Schematic of a GISAXS experiment and a typical 2D GISAXS scattering pattern recorded from a mesoporous silica containing vertically-aligned hexagonally ordered nanochannels. Right: X-ray scattering intensities integrated along the horizontal axis attained from the 2D scattering pattern labelled with the related Miller-indices characteristic of the hexagonal order.*

lected with a two-dimensional detector, Figure 3.2. A silica thin film that contains vertically oriented, hexagonally ordered channel-like pores gives the same characteristic peak positions in GISAXS mode on the horizontal axis of its scattering pattern as described in literature for hexagonal pore structures in particles measured in transmission geometry [76, 77]. Namely, the reflections of the hexagonal lattice of the pores appear in the same relation of the scattering peak positions $q_y(10)$:$q_y(11)$:$q_y(20)$:$q_y(21) = 1{:}\sqrt{3}{:}\sqrt{4}{:}\sqrt{7}$, characteristic of the hexagonal symmetry. This allows to determine the cell parameter, a, from the correlation length $d(11)$:

$$a = 2 \cdot d(11) \tag{3.3}$$

The GISAXS measurement on the studied thin films, presented in this thesis and in Paper I, Paper III, and Paper IV, were performed in grazing incidence mode using a Mat:Nordic instrument from SAXSLAB/Xenocs (containing Cu-radiation source and Pilatus 300K detector), by placing the samples on a GISAXS holder and aligning before each measurement. The sample to detector distance was set to 305 mm, the incidence angle to 0.2°, and the exposure time to 6 h or 20 h. A scattering pattern was collected before and after measurement for 20 min to make sure that no radiation damage occurred. The collected 2D scattering patterns were further processed with the SAXSGUI (Rigaku) software by horizontal integration of scattering intensities between $q_z = 0.01$ Å^{-1} and $q_z = 0.06$ Å^{-1}, and plotted as a function of q_y, see Figure 3.2.

3.3 Nitrogen adsorption

By nitrogen adsorption it is possible to characterise porous structures at nano- and micrometre scale. During the measurement, a nitrogen adsorption isotherm (at $T = 77$ K) is recorded that is in practice plotted as volume of adsorbed nitrogen gas versus the relative pressure (i.e. pressure/saturation vapor pressure). From the obtained adsorption isotherm, parameters as surface area, pore volume, and pore size distribution can be determined. Moreover, it can provide information on enthalpy of nitrogen desorption and, based on the adsorption hysteresis, the pore morphology of the studied porous material [78] [79]. In case of mesoporous silica, the surface area is commonly determined by the use of the BET (Brunauer-Emmett-Teller) method. To do so, several assumptions are made; (i) gas is considered ideal, (ii) first a monolayer of nitrogen molecules forms during adsorption on the surface, (iii) adsorbed molecules do not move on the surface, (iv) enthapy of adsorption is uniform on the sample surface while adsorbate-adsorbate interaction is neglected and the enthalpy of adsorption for the second molecular layer equals the enthalpy of vaporisation. Thus, from the volume of the nitrogen monolayer adsorbed on the sample, V_m, surface area is calculated by using

the area occupied by an adsorbed molecule. To determine V_m, the BET equation is fitted in the linear range of the isotherm typically at p/p_0 = 0.05-0.3 and interpolated to the ordinate;

$$\frac{p}{V\left(p_0 - p\right)} = \frac{1}{V_m C} + \frac{C-1}{V_m C}\left(\frac{p}{p_0}\right) \tag{3.4}$$

where p (partial pressure of the nitrogen) and V (volume of nitrogen adsorbed) are known from the adsorption isotherm while p_0 (saturation vapor pressure) is a well-defined parameter for a given temperature. V_m and C-value are determined from the slope and intersection. The C-value has relevance considering its theoretical relation to the enthapy of desorption ($\Delta_{des}H$) and enthalpy of vaporisation ($\Delta_{vap}H$);

$$C = e^{\frac{\Delta_{des}H - \Delta_{vap}H}{RT}} \tag{3.5}$$

Even though $\Delta_{ads}H$ could be technically calculated by assuming that desorption and adsorption enthalpies are equal ($\Delta_{des}H = \Delta_{ads}H$), determining it from the C-parameter is known to be inaccurate and for its exact measurement calorimetric methods are preferred. However, it is worth to keep in mind that a higher C-value indicates a higher difference between $\Delta_{des}H$ and $\Delta_{vap}H$ and in such case the assumption of monolayer formation on the surface is more valid. Accordingly, BET method is used if $C > 2$. From the nitrogen adsorption measurement the pore size distribution can be determined as well. For this, the BJH (Barrett-Joyner-Halenda) method is typically applied to the adsorption isotherm. The BJH method is based on the modified Kelvin equation with the assumption of cylindrical pores. As a commonly used method, its validity has been studied and discussed widely and confirmed for various mesoporous materials; it has also been observed that for narrow mesopores the pore size can be slightly underestimated. Furthermore, the total pore volume can be determined as well, for this commonly the Gurvich rule is applied. The Gurvich rule assumes that when the pores are filled ($p/p_0 > 0.95$), the adsorbed amount of nitrogen is in liquid state and therefore its volume in the pores is quantifiable.

Nitrogen adsorption, presented in this thesis and Paper II, was measured on a TriStar 3000 instrument from Micromeritics. Beforehand, the samples were exposed to outgassing treatment for overnight at 120 °C under a nitrogen flow. Their surface areas were determined by applying the BET (Brunauer-Emmett-Teller) method, the pore size distribution by the BJH (Barrett-Joyner-Halenda) method, and the total pore volume by the Gurvich rule at $p/p_0 = 0.98$.

3.4 X-ray photoelectron spectroscopy (XPS)

X-ray photoelectron spectroscopy (XPS) is a surface sensitive analytical technique suitable for quantitative and qualitative chemical analysis and electronic structure study of the sample's material [80]. The technique is based on the photoelectric effect during which electrons (photoelectrons) are emitted from the material as a result of energy uptake from the absorption of incident X-ray radiation with sufficiently high frequency, see Figure 3.3. The excited photoelectrons travel through the sample to the surface and escape into the vacuum where they are collected and their kinetic energies are measured. From the kinetic energy the binding energy can be calculated as follow:

$$h\nu = E_B + E_K + \Phi \tag{3.6}$$

where hν is the energy of the incoming X-ray photon, E_B is the binding energy, E_K is the kinetic energy of the photoelectron, and Φ is the work function term. The electron binding energy, also called ionisation energy, is characteristic to the element from which the electron is emitted. Therefore elemental compostiton of the surface can be determined. Huge advantage of XPS method is that most, even lighter, elements can be detected. As the typical escape depth of the photoelectrons is on the nanometre scale, XPS is a surface sensitive method providing information on the topmost few nanometres of a solid sample.

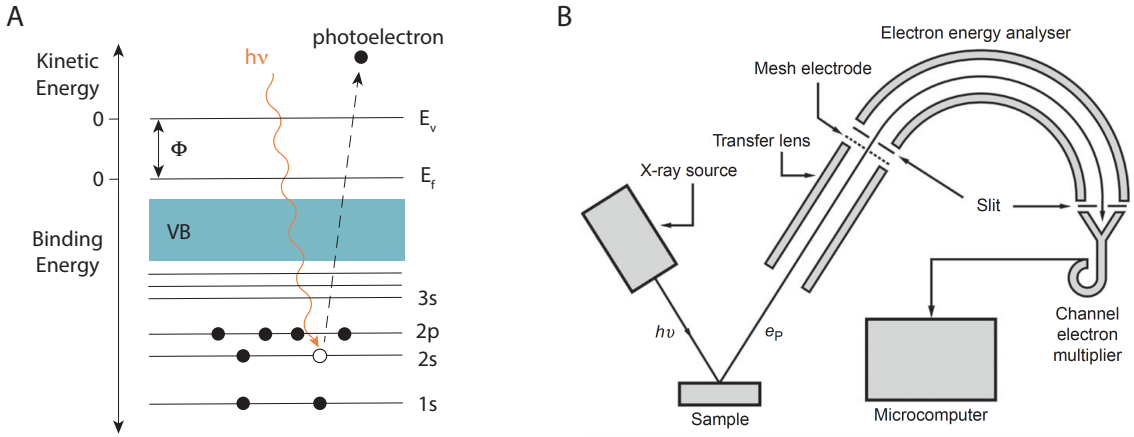

Figure 3.3: *XPS. A: Example of photoelectron emission process presented on an energy level diagram of an oxygen atom. B: Schematic of an X-ray photoelectron spectroscope. The figure is reproduced from reference [80] with permission from Springer.*

X-ray photoelectron spectroscopic measurements, presented in this thesis and Paper II, were carried out on a Quantum 2000 scanning ESCA microprobe from Physical Electronics with AlKα (1.486 keV) beam with an incidence angle of 45°. To determine the atomic concentration, the MultiPAK software package was used. Photoelectrons were collected on approximately 500 x 500 μm^2 large sample areas.

3.5 Vibrational spectroscopy

The energy in a molecule is quantised and allowed to only be in a discrete number of levels, ϵ_i, which are the sum of different modes of motion and electronic contributions, as follows [79]:

$$\varepsilon_i = \varepsilon_i^T + \varepsilon_i^R + \varepsilon_i^V + \varepsilon_i^E \tag{3.7}$$

In eq. 3.7, T denotes translation, R rotation, V vibration, and E the electronic contribution. The magnitude of the excitation energy depends on the type of transition and in case of vibrational modes this is around the energy of an electromagnetic wave with 10^2-10^3 cm^{-1} wavelength (belonging to the Infrared range of the electromagnetic spectrum).

By vibrational spectroscopy vibrational excitations can be studied, which are induced by photon irradiation. These vibrational modes are characteristic of chemical groups and also depend on the chemical environment [81]. The modes of vibrations are listed in Table 3.1 while the number of vibrational modes of a given molecule is determined by the number of atoms that it contains (N). Non linear molecules possess $3N$-6, linear ones possess $3N$-5. Their vibrational energies usually have the following order: ν(stretching)> δ(in-plane bending)> γ(out-of-plane bending)> τ(torsion).

Table 3.1: *Vibrational modes*

Symbol	Name	Mode of deformation
ν	stretch	stretching of covalent bond
δ	in-plane bend	one or more bond angle changes, constant bond length
γ	out-of-plane bend	at least one atom oscillates through a plane
τ	torsion	dihedral angle is changed

3.5.1 Infrared spectroscopy (IR)

In case of Infrared spectroscopy, the necessary energy for vibrational excitation is supplied by absorption of Infrared light that at room temperature induces v = 0→1 transition in most vibration modes due to high population of the ground state (v = 0) (however, weak overtone bands might also appear on the spectra originating from v = Δ2 transitions) [79]. For obtaining vibrational excitation by absorption of electromagnetic wave the resonance condition requires that the frequency of the radiation equals that of the vibration and that there is an electrical dipole that can couple with the sinusoidally changing electromagnetic field of the incoming radiation. Therefore, polar bonds display high intensity of Infrared absorption.

Modern Infrared spectrometers contain interferometers that allow the use of a high intensity polychromatic beam, ensuring excellent signal-to-noise ratio and fast data acquisition. In the interferometer the incident beam is first splitted: one part of it is reflected towards a fixed mirror and the other is transmitted towards a moving mirror. After that, they are reflected from the two mirrors back to the beam splitter where they recombine and the combined beam containing the interference patterns (generated by the optical path difference of the splitted beams controlled by setting the moving mirror) is directed to the sample. After passing the sample, where the characteristic wavelength components are absorbed simultaneously, the modified interferogram is collected on the detector. Then, the interferogram is converted to transmittance spectrum with Fourier-transformation; thus the described method is called Fourier-transform Infrared spectroscopy (FT-IR).

Attenuated total reflectance IR specroscopy (ATR-IR)

In attenuated total reflectance IR specroscopy (ATR-IR) an ATR accessory is placed in the pathway of the IR beam. The accessory contains a so-called ATR crystal with a good Infrared transmission and a high refractive index, which at suitable incident angle of the IR beam allows internal reflections of the beam within the crystal. The sample is placed in contact with the crystal and at the reflection points the incident light penetrates into the material of the sample as an evenescent wave, see Figure 3.4. IR photons with frequencies far from the absorption region will be totally reflected, while the reflection will be attenuated if the frequency of the incident photon is within the range of the absorption frequencies [82]. Thus, an absorption spectrum can be obtained from the IR beam leaving the ATR accessory and collected on the detector. The penetration depth in the sample, d_p, from which the chemical information is collected, is usually in the order of micrometres.

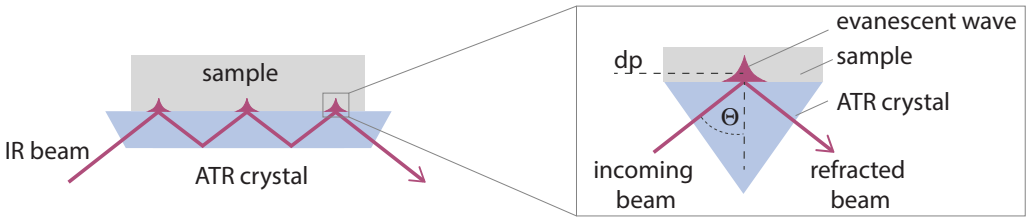

Figure 3.4: *Schematic of attenuated total reflectance occuring during ATR-IR measurement.*

The ATR-IR spectra, presented in this thesis and in Paper II, were recorded on a PerkinElmer Fourier transform Infrared (FT-IR) spectrophotometer. The ATR accessory contained a single reflection diamond ATR crystal (GladiATR, Pike Technologies), thus the spectra were cut between 2600 and 1900 cm^{-1}. The full optical range was obtained from 4000 cm^{-1} to 400 cm^{-1}, the resolution was

set to 1 cm^{-1}. For all experiments 64 scans were collected and averaged and the recorded spectra were subjected to baseline correction.

Transmission-reflection IR spectroscopy

Transmission-reflection IR spectroscopy is a spectroscopic technique especially suitable for studying films on a smooth, reflective substrate like gold or ITO [31]. During the measurement most of the incoming IR beam penetrates the surface of the film and is then reflected at the substrate. In this way, the light passes through the surface layer twice, leading to an absorption spectrum similar to a conventional transmission spectrum.

Vibrational spectra of the studied thin films, presented in this thesis and in Paper I, Paper III, and Paper IV, were recorded with a PerkinElmer Fourier transform Infrared (FT-IR) spectrophotometer. The measured spectral range was from 4000 cm^{-1} to 400 cm^{-1} with the resolution set to 4 cm^{-1}. For all experiments, 64 scans were collected and averaged and the recorded data were baseline corrected.

3.5.2 Raman spectroscopy

During Raman spectroscopic measurements vibrational excitation in the studied material is induced through inelastic scattering of a monochromatic, high intensity, coherent light beam with suitable wavelength (UV to near-Infrared laser) [83]. During Raman scattering, inelastic photon scattering occurs; the energy of the scattered photon changes according to the energy input or output related to the change in vibrational state of the material, as shown on a Jablonski diagram in Figure 3.5. When the material is excited to a higher vibrational state the energy of the scattered light gets lowered with the energy difference of these states (called the Stokes scattering). In contrary, when the material is already at higher vibrational state and gets to a lower one during the scattering process, the excess energy is taken up by the scattered photon (called anti-Stokes scattering). Elastic scattering without energy change of the photon also occurs. This is called the Rayleigh scattering and most of the incoming photons scatter in this way. Therefore, to gain high enough flux of inelastically scattered photons, a laser is used. In addition, Stokes scattering has a higher probability than anti-Stokes scattering since at room temperature most of the molecules are in the ground vibrational state. Thus, the energy shift (Raman shift) relative to the energy of the incoming photon is typically measured from the energy of the Stokes scattered photons.

The intensity of the Raman scattered radiation is defined by the following relation:

$$I_R \propto \nu^4 I_0 N \left(\frac{\delta\alpha}{\delta Q}\right)^2 \tag{3.8}$$

where ν is the frequency of the exciting laser, I_0 is the incident laser intensity, N is the number of scattering molecules, Q is the vibrational amplitude, and α is the polarizability of the molecular bond. The polarizability of the bond, α, determines the Raman activity of the molecular vibration; the Raman active vibrational modes are usually inactive in Infrared spectroscopy and *vice versa*. Therefore, Raman and Infrared spectroscopies are typically used complementary.

Confocal Raman spectroscopy is an excellent method for chemical mapping in 2D and 3D with micrometre scale resolution. In our studies (Paper II), it has been used for chemical mapping of IL-filled mesoporous silica microparticles. The measurement steps are shown schematically in Figure 3.6 [5]. In brief, over a selected area covered with the microparticles the confocal point is set at half-diameter height of the particles (approximately 3 μm) and the most intense Raman peak of the ionic liquid was used as the probe signal to obtain information on the location and chemistry of the liquid phase. The shown 2D map, Figure 3.6 C, is created by transforming the integrated intensity of the selected peak into a color code at every collection point (black for less intense and red for more intense).

For chemical characterisation of IL/silica hybrid materials, presented in this thesis and in Paper II, Raman point-spectra were obtained with a Renishaw InVia Reflex Raman spectrophotometer equipped with an X100 LWD Leica objective and a CCD detector. A 532 nm wavelength diode laser was used for vibrational excitation covering the spectral range 100-4000 cm^{-1} and the grating used had 2400 grooves/mm. The confocal Raman mapping was carried out with the same equipment and with the use of 532 nm wavelength diode laser. Before each measurement, the spectrophotometer was calibrated to the 1^{st} order band of a Si wafer at 520.6 cm^{-1}.

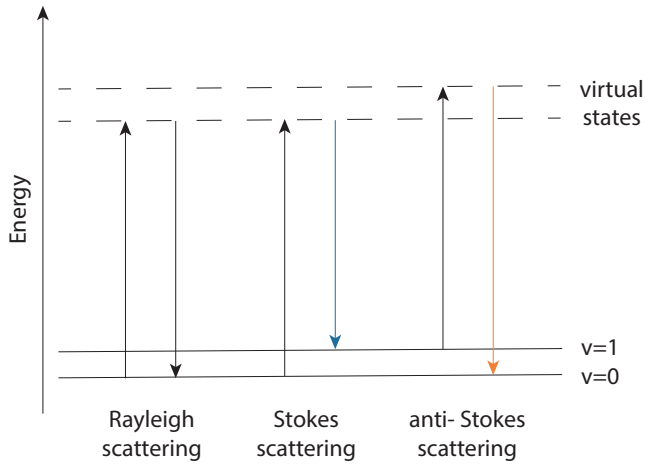

Figure 3.5: *Elastic (Rayleigh) and inelastic scattering (Stokes and anti-Stokes) of an incoming photon with suitable wavelength for vibrational excitation presented on a Jablonski diagram.*

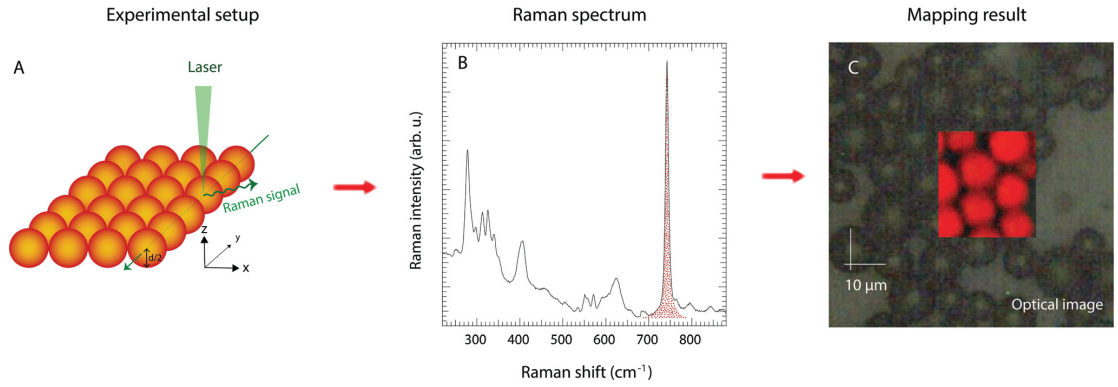

Figure 3.6: *Chemical mapping experiment performed with confocal Raman spectroscopy over mesoporous silica particles filled with an ionic liquid. The figure is reproduced from reference [5] with permission from The Royal Society of Chemistry.*

3.6 Cyclic voltammetry (CV)

Cyclic voltammetry (CV) is a powerful tool to study charge transfer involved in an electrochemical process, since it can provide information on the occuring process itself and also on other related parameters [84, 85]. CV measurements are typically carried out in a three-electrode cell, which consists of an inert counter electrode, a reference electrode with well-defined and stable equilibrium potential, and a working electrode all immersed in an electrolyte solution, see schematic shown in Figure 3.7 A.

When the aim is to study the working electrode, a substance with a known electrochemical behaviour, i.e. an electrochemical probe or redox probe, is added to the electrolyte. Metal complexes are often used as redox probes. The redox reaction of the probe on the working electrode is followed by recording a voltammogram; e.g. recording the current as a function of the sweeping voltage applied to the working electrode relative to the reference electrode. A typical voltammogram of a redox probe with an oxidation number change of one is plotted in Figure 3.7 B [84]. The equilibrium between the reduced and the oxidised forms of the probe is described with the Nernst equation:

$$E = E^0 + \frac{RT}{F} ln \frac{(a_{ox})}{(a_{red})} \approx E^{0\prime} + \frac{RT}{F} ln \frac{[ox]}{[red]} \tag{3.9}$$

where E^0 is the standard potential, R is the universal gas constant, T is the temperature, F is Faraday constant, $E^{0\prime}$ is the formal potential, and the relative activities (a) of the oxidised (ox) and reduced (red) forms of the probes in the system at equilibrium are approximated with their concentrations, [ox] and [red], respectively. As shown in Figure 3.7 B, oxidation and reduction reactions are detected as current peaks. When a solution of, for example, the oxidised form is

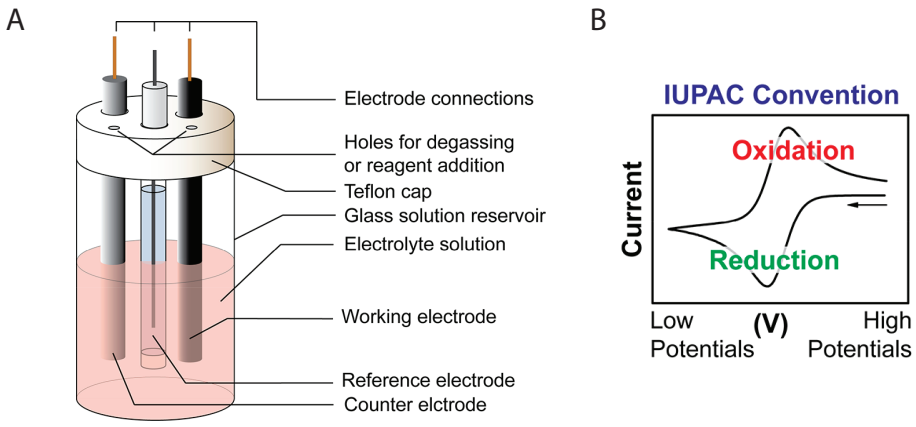

Figure 3.7: *Cyclic voltammetry. A: Three-electrode electrochemical cell suit for cyclic voltammetric measurement B: Voltammogram of a redox probe with an oxidation number change of one. The figure is reproduced from reference [84] with permission from the American Chemical Society.*

scanned to negative potentials, it gets reduced at the working electrode resulting in concentration increase of the reduced form at the surface of the electrode, therefore the mass transport of the oxidised form toward the electrode becomes limiting. When the redox reaction is reversible, similar phenomena occur in the reverse scan and therefore the voltammogram shows a so-called duck-shape. In short, the position and shape of the current peaks provide information on the diffusion of the redox probe near the electrode.

CV measurements, presented in this thesis and in Paper I, Paper III, and Paper IV, were used to characterise the permeability of IL-templated silica thin films. For this, various coordination compounds as redox probes were used with different and characteristic electrochemical properties, namely the positive redox probe $[Ru(NH_3)_6]Cl_3$, the negative redox probe $K_3[Fe(CN)_6]$, and the neutral redox probe FcMeOH. In case of the as-synthesised films, in which the template is still present in the nanochannels, the neutral probe can pass through the channels as it proposedly solubilise in the apolar phase of the template and is able to reach the ITO substrate (which is here also the working electrode) giving rise to redox peaks [85]. Meanwhile, the positive and negative redox probes are blocked by the template to reach the ITO substrate, therefore the recorded voltammogram do not show current peaks. After extraction, the empty silica nanochannels are negatively charged under the circumstances of the measurement, thus, the positive and neutral redox probes are able to give current signal while the negative redox probe is unable to pass through the nanochannels due to electrostatic repulsion [85].

The CV measurements on IL-templated silica thin films, presented in this thesis and in Paper I, Paper III, and Paper IV, were carried out in a three-electrode

system that contained a Ag/AgCl reference electrode (Metrohm), a stainless steel counter electrode, and a bare ITO plate or ITO plate with the deposited silica film on it as the working electrode. The aqueous electrolyte solution contained 0.5 mM redox probe and 0.1 M $NaNO_3$, while the contact area with the solution was 0.2 cm^2. The voltammogram curves were recorded with a μAutolab III potentiostat (Eco Chemie) or a Gamry Interface1000E potentiostat at a scan rate of 20 mV/s.

CV was also applied to measure the electrochemical window of the ionic liquid, HC_8imTFSI, using a three-electrode cell, as presented in Paper IV. For the measurement of ionic liquids, typically a pseudoreference electrode is used, here a Ag wire while the counter electrode was a platinum coil and the working electrode was a bare ITO plate with a circular contact area of 0.2 cm^2. The studied ionic liquid, HC_8imTFSI, functioned also as the electrolyte. The voltammetric curves were recorded with a Gamry Interface1000E potentiostat at a scan rate of 100 mV/s between -1.3 V and 2.1 V (vs. Ag).

3.7 Electrochemical impedance spectroscopy (EIS)

Electrochemical impedance spectroscopy (EIS) is a widely used technique to characterise electrical properties of materials and devices, by studying the impedance function, Z^*. To measure the sample's impedance, an alternating voltage *V(t)* is applied with a constant frequency of $\omega/2\pi$ that induces a current *I(t)* with the same frequency in the sample. Depending on the electrical properties of the sample, phase shift occurs between the applied voltage, *V(t)*, and the measured current, *I(t)*, described with phase angle, ϕ. The voltage and current are convenient to be expressed in complex notation, as well as the complex impedance $Z(t)^*$ [86]:

$$V(t) = V_A \sin(\omega t) \tag{3.10}$$

$$I(t) = I_A \sin(\omega t + \phi) \tag{3.11}$$

$$Z(t)^* = \frac{V(t)}{I(t)} = Z_A \frac{\sin(\omega t)}{\sin(\omega t + \phi)} = Z' + jZ'' \tag{3.12}$$

where V_A and I_A are amplitudes of voltage and current, respectively, ω is radial frequency, *Z'* is the real part of the impedance, and *Z"* is the imaginary part. In practice, the impedance spectrum is obtained by taking measurement points at discrete radial frequency values, (ω), of the alternating voltage. The impedance spectra can be represented on a Lissajous plot or in modern impedance spectroscopy more often on a complex impedance plot (also called Nyquist plot), see Figure 3.8 [86].

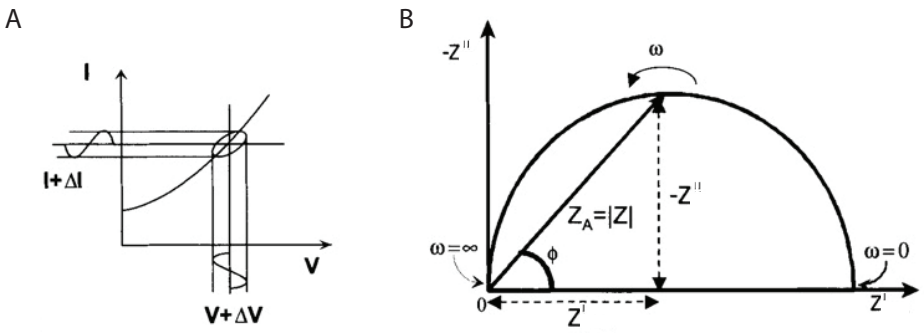

Figure 3.8: *Impedance spectroscopy. A: Impedance data represented on a Lissajous plot showing the measured current as a function of the perturbing voltage. B: Complex impedance plot, also called Nyquist plot. The figure is reproduced from reference [86] with permission from John Wiley & Sons.*

3.7.1 Broadband dielectric spectroscopy (BDS)

Broadband dielectric spectroscopy (BDS) is suitable to determine the intrinsic dielectric properties of a material, like the permittivity, $\epsilon^*(\omega)$, and conductivity, $\sigma^*(\omega)$, spectra that are delivered from the impedance, $Z^*(\omega)$, with the help of well defined sample dimensions (accordingly, BDS instruments have specific design to serve this purpose) [87]. The dissipation factor, tanδ, is related to the real and imaginary parts of both the impedance and the permittivity:

$$tan\delta = \frac{-Z''}{Z'} = \frac{\epsilon''}{\epsilon'} \tag{3.13}$$

Considering the interpretation of the real, Z', and imaginary, Z", parts of the impedance; when tanδ < 1 and Z' > Z" the system is considered more insulating than conducting. Similarly, the real part of permittivity, ϵ', is the relative permittivity while the imaginary part, ϵ", is the dielectric loss or loss factor and the larger values of the dielectric loss suggest a stronger deviation from an ideal dielectric. In relation to the permittivity, the conductivity can be determined as well:

$$\sigma(\omega)^* = j\sigma\epsilon_0\epsilon^*(\omega) \tag{3.14}$$

where ϵ_0 is the permittivity of vacuum. The ionic conducitvity of ionic liquids is obtained from the real part of the conductivity, namely from the plateau region of the $\sigma'(\omega)$ spectrum showing the frequency independent dc conductivity, σ'_{dc}, at which the polarisation effect and ac conductivity contributions are negligible [88].

The broadband dielectric spectroscopic measurements of IL-based materials were carried out on a Novocontrol GmbH instrument. The samples were placed between two gold-plated brass electrodes with a defined circular contact area with

the diametre of 13.5 mm and the thickness of the samples set to 1 mm by using a silica spacer. Data were collected in the frequency range of 10^{-1} - 10^{7} Hz, in given temperature steps and range (see in Paper II and Paper IV), while the stabilisation time was set to 600 s.

3.7.2 Equivalent circuit modelling

Impedance spectroscopic data obtained for an electrochemical cell, to study for example the double layer at an electrode, outer layers of colloidal particles, corrosion or other electrochemical reactions etc., is commonly analysed by fitting with an equivalent electrical circuit model [86, 87, 89, 90]. An important aspect is that equivalent circuits should be selected ideally on the basis of the given electrochemical systems. In some cases, even though the "the best fit" between the model and the experimental data applies, it does not necessarily mean that the developed equivalent circuit model has physical meaning. Therefore, the estimated physical parameters obtained with equivalent circuit modelling need careful interpretation. Common ideal circuit elements are listed in Table 3.2 along with the CPE (constant phase element) which is suitable to model the impedance response of a non-ideal capacitor, also used in Paper IV. In the listed equations R is resistance, V is voltage, I is current, C is capacitance, L is inductance, Q is the constant phase element and α is the exponent.

Table 3.2: *Common ideal circuit elements and the CPE (constant phase element)*

Component	Equivalent Element	Current vs. Voltage	Impedance
Resistor 	R (Ω)	$V=IR$	R
Capacitor 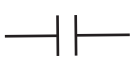	C (F)	$I=CdV/dt$	$1/j\omega C$
Inductor 	L (H)	$V=Ldi/dt$	$j\omega C$
CPE 	Q ($\Omega^{-1}s^{\alpha}$)		$1/Q(j\omega)^{\alpha}$

Impedance measurements, presented in this thesis and in Paper IV, were conducted in a three-electrode cell in which the counter electrode was a platinum coil and a Ag wire was used as the pseudo-reference electrode. Two different working electrodes were used in contact with the studied ionic liquid with a circular contact area of 0.2 cm^2. These were: i) an "ITO+Film", i.e. an ITO substrate covered

with a thin film of porous silica containing vertically aligned nanochannels (to investigate the effect of confinement on the electrochemical behaviour of the ionic liquid) and ii) a bare "ITO", i.e. a bare and neat ITO electrode used as a reference (to study the electrochemical behavior of the bulk ionic liquid). The impedance spectra were recorded with a Gamry Interface1000E potentiostat in the frequency range from 10^{-2} Hz to 10^{6} Hz at room temperature. The sinusoidal potential perturbation had an amplitude of 10 mV (rms). Equivalent circuit modelling was used to estimate the electrochemical properties of the studied electrochemical cells with different working electrodes.

3.8 Nuclear magnetic resonance (NMR)

NMR spectroscopy is a spectroscopic technique that provides chemical information from magnetic resonance of nuclei that can be characterised with a nuclear spin quantum number, I, larger than zero (those with $I = 0$ possess no nuclear spin and are "NMR silent"). Nuclear spins have a magnetic moment and when placed in an external magnetic field, their magnetic moments align relative to this external magnetic field in a discrete number of orientations. Accordingly, due to the resulted split up of the spin states, the nuclei in the external magnetic field can be on $2I+1$ possible spin states populating them according to the Boltzman distribution. The unequal population of the spin states gives rise to a resultant bulk magnetisation vector M_0 (in a Descartes system conventionally along the z-axis). The energy difference between the states is proportional to both the external magnetic field, B_0, (more exactly its magnetic flux density), and to the magnetogyric ratio (γ) characteristic of a given isotope, see Figure 3.9 [81, 91].

To obtain an NMR spectrum, the exciting electromagnetic radiation, used to acquire nuclear spin transition from lower to higher energy level, is on the radiofre-

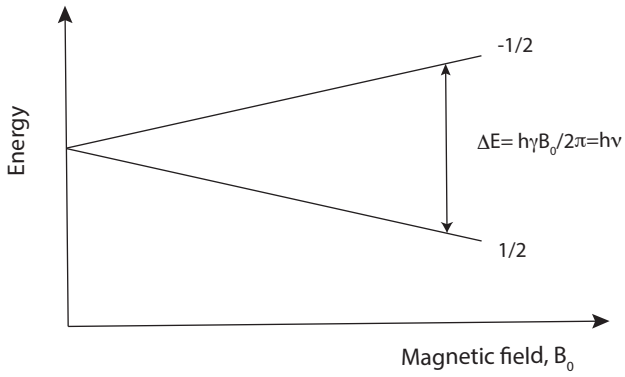

Figure 3.9: *Representation of the increasing difference in the energy levels between splitted nuclear spin states proportional to the external static magnetic field shown for a nucleus with I = 1/2 as an example.*

quency range. As the magnetic resonance frequency is affected by the electronic environment of the nucleus and the presence of magnetic nuclei in its vicinity the NMR spectrum is characteristic to the molecular structure and its chemical environment [81, 91]. Besides providing energy for spin transition, during the method called pulsed-field gradient nuclear magnetic resonance spectroscopy (PFG-NMR), additional rf (radiofrequency) pulse is applied to provide B_1 magnetic field perpendicular to the static field, B_0 (as the rf pulse intrinsically has magnetic component). Accordingly, picturing in a Descartes coordinate system, B_0 causes net z magnetisation, while B_1 rotates the M_0 magnetisation vector toward the x-y plane. The angle through which the M_0 vector turns is dependent on the duration and amplitude of the pulse. In absence of an additional magnetic gradient pulse the perturbed system goes through relaxation processes that results in the decay of the detected NMR signal (electric current signal generated by the rotating M_0 vector that decays as M_0 returns to its equilibrial orientation, also called spin-echo).

In Paper II, NMR spectroscopy was used not only for determining chemical composition but also for studying diffusivity of molecular species containing hydrogen atoms, present in the imidazole/HCimTFSI mixture in bulk and in confining space of mesoporous silica, respectively. For this, PFG-NMR spectroscopy was used. If the sample is also given magnetic gradient pulses in a defined scheme, the diffusing species containing ^{1}H atoms might not get exposed to the same local magnetic field during the pulse sequence as they can diffuse away [91, 92]. Thus, the detected NMR signal change accordingly, described as:

$$I = I_0 \exp\left(-D\left(\gamma\delta G\right)^2\left(\Delta - \frac{\delta}{3}\right)\right) \tag{3.15}$$

where I is the signal intensity, I_0 is the signal intensity at zero gradient strength, G is the gradient strength (in Paper II the changing variable), D is the self-diffusion coefficient, δ and Δ are the duration of the gradient pulses and the time delays between them. The self-diffusion coefficient can be determined by plotting $\ln(I/I_0)$ vs. G^2 that yields a linear plot whose slope is proportional to D [91, 92].

The diffusion NMR experiments were carried out at 30 °C on a Bruker Avance 600 NMR spectrometer equiped with a 5 mm 1H/2H RF double-coil insert and connected to a 60 A gradient amplifier. The relaxation times (T_1 and T_2) were, respectively, obtained by standard inversion recovery and CPMG (Carr-Purcell-Meiboom-Gill) pulse sequences. For the case of liquid samples the gradient pulse length, δ, was set to 1 ms and a diffusion time, Δ, to 100 ms while the gradient strength, G, was ramped uniformly in 16 steps from 0.1 to 12 T/m. Data were collected at each gradient value with a sum of 8 acquisitions and 7 s recycle delay time. For the hybrid samples, the stimulated echo sequence using bipolar pulses was used to suppress the influence of internal background gradients. The gradient pulse length, δ, was equal to 0.37 ms while the diffusion time, Δ, was set to 300

ms, and the gradient strength, G, was ramped uniformly in 16 steps from 0.1 to 17 T/m. Data were collected at each gradient with a sum of 8 acquisitions and 4 s recycle delay time. The gradient strength was calibrated with the self-diffusion coefficient of the standard sample containing HDO in pure D_2O.

4 Results and discussion

4.1 PIL/silica hybrid materials

This chapter is based on two studies of different PIL/silica hybrid materials presented in Paper II and Paper IV. These studies differ substantially in the chemical and morphological character of the confining porous silica matrix. In Paper II the molecular dynamics and related local structure of an imidazole/PIL mixture have been investigated when confined in hydrophobised mesoporous silica particles, by characterisation of a sample series with varying liquid-to-silica ratios. While in Paper II the confining silica matrix has a disordered pore structure containing both mesopores ca. 5 nm and micrometre-scale cavities, in Paper IV the PIL is studied in straight, discrete nanochannels with a pore diameter estimated to be 3.5 nm. These nanochannels are located in a hydrophilic silica thin film ensuring vertical diffusion pathway through the film. The well-defined, ordered morphology of this system enabled the use of equivalent circuit modelling, thus charge transfer and capacitive behaviour of the nanoconfined PIL have been investigated upon applied voltage.

4.1.1 Structure and interactions

In the PIL/silica hybrid material consisting of a liquid phase of imidazole/ HC_8imTFSI mixture ("Im/PIL mixture") and a solid phase of mesoporous silica microparticles hydrophobised with trioctylsilyl-groups ("5-C8-SiO_2") the population of the ionic liquid at different sites is dependent on the liquid-to-silica ratio (Paper II). The liquid-to-silica ratio was expressed as "pore filling" in unit of %, with respect to the volume of the added Im/PIL mixture relative to the available pore volume in the mesoporous silica. To confirm that the Im/PIL mixture penetrated into the pores of the mesoporous silica and distributed evenly, chemical mapping with confocal Raman spectroscopy was used (see Figure 4 in Paper II). A schematic of the prepared sample series is presented in Figure 4.1 A and the in-pore structure in Figure 4.1 B, showing possible locations of the Im/PIL mixture; (i) adsorbed onto the silica surface at pore wall or outer surface of the particle, (ii) located in the pore centre, and (iii) located in the microcavities between the silica microparticles. The SEM characterisation has revealed that the silica microparticles are uniformly spherical with a diameter around 6 μm, thus the cavities in between the particles are in micrometre-scale, while the maximum

in the pore size distibution of the mesopores inside the particles was determined to be 5.6 nm with BET (see Figure 3 in Paper II).

To reveal local structure and related interactions within the pores, X-ray scattering and vibrational spectroscopic experiments were performed on these PIL/silica hybrid materials at room temperature. The changes in the X-ray scattering pattern upon composition is shown in Figure 4.1 C. The neat Im/PIL mixture shows three characteristic peaks, that have been discussed widely for numerous protic and aprotic ionic liquids [1, 2, 26, 93]. Accordingly, the peak centred at 0.84 $Å^{-1}$ arises from all ion-ion alternations, and the peak at 0.34 $Å^{-1}$ arises from chain-chain segregation and corresponds to a scattering length of 1.8 nm indicating that the addition of imidazole does not disrupt the native polar/apolar structuration

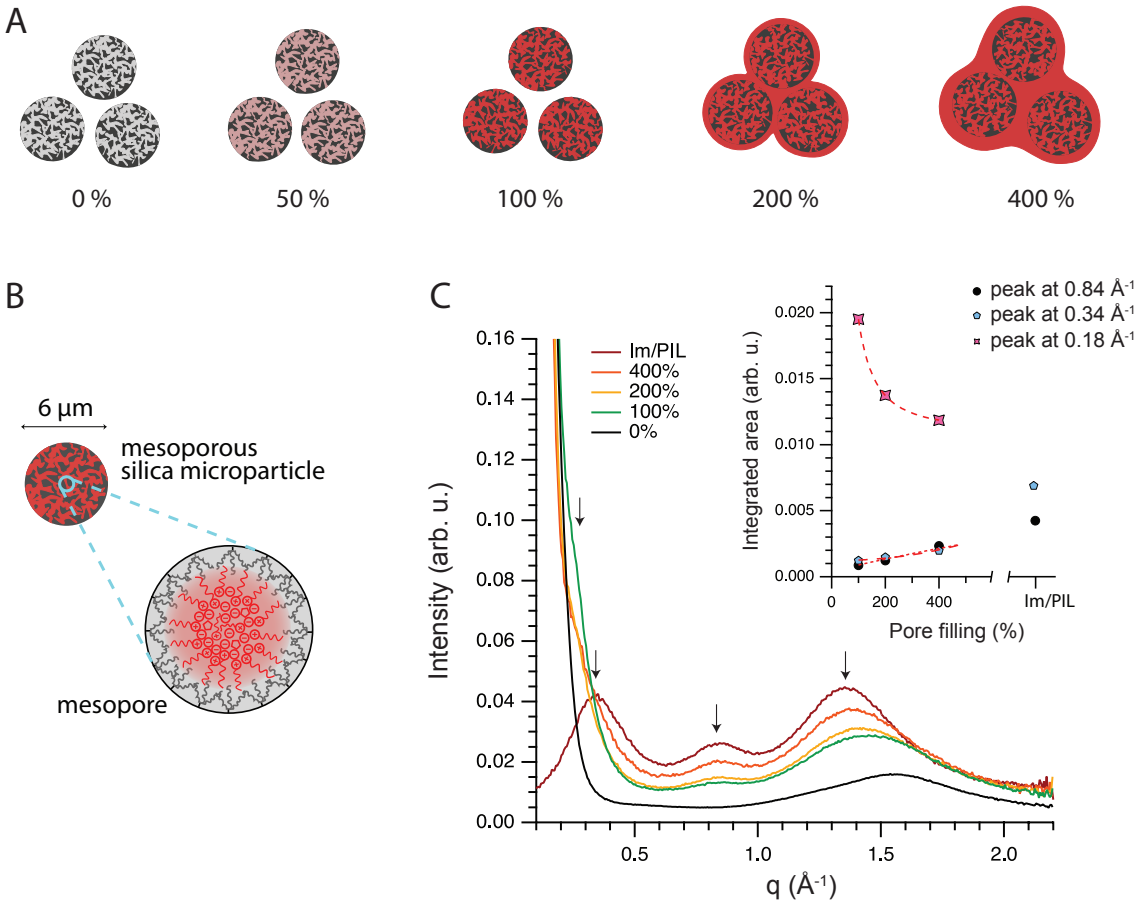

Figure 4.1: *A: Illustration of, from left to right, the bare mesoporous silica microparticles (5-C8-SiO_2) and the same particles filled by an increasing amount of the Im/PIL mixture. B: Illustration of the speculated local structure inside the mesopores. C: Small-angle X-ray scattering intensity collected for the bare silica particles (black trace), different samples with varying pore filling (orange, yellow and green) and the neat Im/PILmixture (dark red). The inset plot shows the integrated areas under selected fit peaks as a function of composition.*

observed for the bulk ionic liquid [2, 94]. Besides, the bare silica microparticles contribute at about 1.6 $Å^{-1}$ with a broader feature and with a strongly increasing scattering intensity in the low-q range (below 0.3 $Å^{-1}$). After multiple-peak fitting of the scattering data, it was found that the intensities of the characteristic peaks (i.e. the integrated areas under the peaks) at 0.34 $Å^{-1}$ and 0.84 $Å^{-1}$ increased with increased pore filling factor, see inset of Figure 4.1 C, but their peak positions remained unchanged indicating that the local ion-ion distances and segregation of alkyl chains are the same inside the mesopores and microcavities as in the neat Im/PIL mixture. Furthermore, in the PIL/silica hybrid materials an additional feature below 0.4 $Å^{-1}$ can be observed, which is not present in the X-ray scattering pattern of the Im/PIL mixture and the neat 5-C8-SiO_2 silica particles, and based on peak-fitting centred at ∼0.18 Å for all compositions, corresponding to ∼3.5 nm real space distance. Its intensity, unlike the peaks at 0.34 $Å^{-1}$ and 0.84 $Å^{-1}$, increased for decreasing filling factors, see the inset of Figure 4.1 C. Based on the X-ray scattering results and the hydrophobic character of the pore wall, it is realistic to assume a local structure inside the mesopores with a monolayer of the amphiphilic cations assembled with their tails oriented toward the pore wall, and a higher density of charges (provided by the cation heads and the $TFSI^-$ anions) towards the centre of the pores in a domain whose size can match the observed distance of ∼3.5 nm (associated to the ∼0.18 $Å^{-1}$ feature). A sketch of this local structure is given in Figure 4.1 B.

Complementarily, vibrational spectroscopy was used to study interaction sensitive vibrational modes that give information on possible interactions in which the IR and Raman sensitive groups of the ionic liquid are involved, the molecular structure of the PIL is shown in Figure 2.1 (and the collected spectra are presented in Figure 13 in Paper II and Figures S7 and S8 in the SI of Paper II). As confocal Raman spectroscopy provides exact information on the location of the obtained spectrum within the sample speciment on the stage, Raman spectra were taken inside the Im/PIL mixture filled silica particles, and in case of samples with pore filling of 200% and 400% also outside of them. Described in more detailed in Paper II, the Raman spectra inside and outside of the silica particles were identical, however, an interesting phenomenon of enhanced Raman intensity was observed inside of the particles. Also, the recorded spectra on the PIL/silica hybrid materials were, independently from the sampling location, practically unchanged compared to the spectrum of the neat Im/PIL mixture. More precisely, the Raman shift range of 240-440 cm^{-1} that contains vibrational modes associated to the to C_1 (*cisoid*) and the C_2 (*transoid*) conformational states of $TFSI^-$ [95, 96] and the expansion-contraction mode of $TFSI^-$ at ∼742 cm^{-1} remain practically unchanged, revealing that the conformational population of $TFSI^-$ and the $TFSI^-$ – imidazolium association were unchanged inside and outside of the mesopores compared to the case of the bulk neat Im/PIL mixture. This also confirms that the $TFSI^-$ anion does not interact significantly with the silica walls,

which agrees with results from X-ray scattering. In line with a previous study by Garaga et al. [48], which revealed that due to what was called by the authors flipped-ion effect in proximity to a hydrophobised silica wall, when the alkyl chain of the imidazolium cation faces the hydrophobic silica wall, the local interaction between the $TFSI^-$ and the imidazolium head remain the same as in the pure PIL or the Im/PIL mixture. In contrast, with untreated silica that offers -SiO^- and -SiOH sites of interactions, a blue shift for the expansion-contraction mode (∼742 cm^{-1}) has been observed [95]. IR spectroscopy was used as well to study the interaction sensitive vibrations of the imidazolium cation, namely its N-H stretch, imidazolium ring stretching, and alkyl chain stretching modes. In the samples with a pore filling equal to or higher than 200%, no shifts could be detected for any of the IR absoption peaks with respect to the spectrum of the neat Im/PIL mixture. However, in the sample with 100% pore filling a small but measurable red shift for the broad N-H stretching mode has been observed (see Figure S8 in the SI file of Paper II). This peak arises mainly from the imidazolium cation, with minor contributions from the imidazole, and its slight red shift is indicative of an average increase in the N-H bond length [5].

The confinement-effect on the properties of the PIL, HC_8imTFSI, was studied in another porous silica matrix as well, more precisely in nanochannels running through a silica thin film deposited on a flat ITO electrode, as presented in Paper IV. The silica matrix has been characterised with CV, GISAXS, and IR (presented in the SI of Paper IV). Based on CV measurements, it has been verified that the silica film covered the entire area of the electrode without defects and that the nanochannels provide a straight diffusion pathway to the ITO electrode. Besides, GISAXS results showed that the individual nanochannels are vertically aligned and straight while their hexagonal lateral order results in a high porosity. In this case, IR spectroscopy was used to ensure that the channels were empty before use. As the nanochannels result from a templating procedure using CTAB (followed by extraction), the diameter of the nanochannels is estimated to be 3.5 nm, while the thickness of the film and hence the length of the nanochannels to be 65 nm [97–99]. To enable sufficient contacts during EIS measurements in the three-electrode cell, a macroscopic layer (on cm-range) of the PIL, HC_8imTFSI, was at place to act as an electrolyte reservoir between the silica film-covered ITO working electrode and the reference and counter electrodes; this phase is referred to as "bulk" PIL.

Information on the local structure and interactions within the nanochannels could be obtained only indirectly, based on the electrohemical parameters estimated with equivalent circuit modelling (which is discussed in-depth in Subchapters 4.1.2. and 4.1.3.) and related literature. Therefore, the in-pore structure described in Paper IV and presented here in Figure 4.2 is a hypothesis. Three different sites of the ionic liquid are distinguised: (i) interfacial, immobile cations, (ii) mobile ions in the centre of the pores, and (iii) ions accumulating at the ITO surface uppon applied voltage. A substantial difference from the PIL/silica hybrid

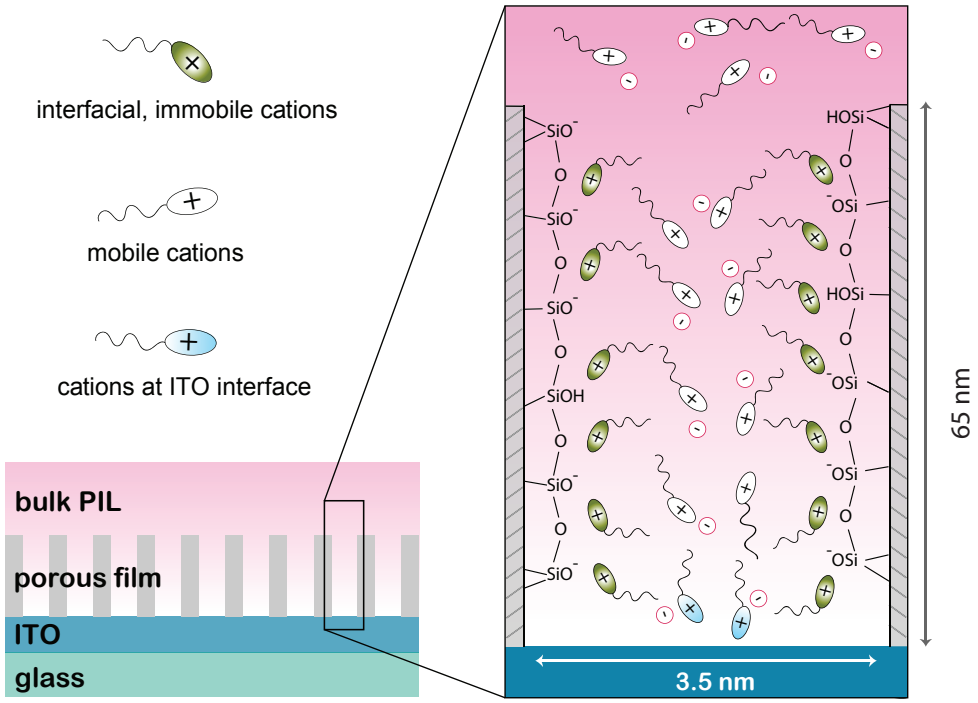

Figure 4.2: *Schematic illustration of the mesoporous silica film deposited on flat ITO electrode (left) and speculated local structure of ionic species inside its nanochannels (right), with the heads of the imidazolium cations interacting strongly with the negatively charged silica walls while their long octyl chains oriented towards the centre of the channel (interfacial cations). The remaining available space defines a straight, oriented pathway for ionic motion towards the ITO electrode and a confined space for charge accumulation at the surface of the ITO electrode upon applied potential.*

materials presented in Paper II is that in this case the confining silica pore had a hydrophilic character having -SiO^- and -SiOH sites. Numerous, congruent studies have demonstrated decreased mobility of ionic liquids in the confining space of such hydrophilic silica pores, which has been explained by strong interactions between the pore wall and the ions [46, 47, 100]. Thus, due to the negatively charged silica pore walls it is expected that an interfacial layer of immobile ions is formed, that consists in imidazolium cations with their aromatic head flatly oriented towards the silica wall while their alkyl chains pointing towards the centre of the pores [46]. In such case, compared to the interfacial cations, the anions are located further away from the silica surface [46, 101]. Notably, the formation of this immobile cationic layer has the double effect of reducing the pore size and of hydrophobizing the solid interface.

4.1.2 Self-diffusion and ionic conductivity in the PIL phase

The transport properties of the Im/PIL mixture while confined in the disordered mesopores of the hydrophobised 5-C8-SiO_2 microparticles, presented in Paper II, were monitored by PFG-NMR measurements and the obtained self-diffusion coefficients are summarised in Table 4.1. For all samples, the self-diffusion coefficients of the imidazolium cation, D_{cat}, were determined directly from the ^{1}H resonance of its CH_2 and CH_3 groups in the octyl chain. Meanwhile, the self-diffusion coefficients of the -NH group, D_{NH}, (to which both -NH groups of imidazole and imidazolium contribute) could be determined only in samples with pore fillings of 200% and 400% due to peak broadening upon decreased liquid-to-silica ratio. In addition, the D_{Im} and D_H values were estimated, as described in more details in Paper II and in reference [5].

Based on the diffusion NMR results, the samples with 50% and the 100% pore filling and the samples with 200% and 400% pore filling, show pair wise similar behaviours. The diffusivity values of the imidazolium cation in samples with a pore filling of 50% and 100% indicate that the nanoconfinement has no adverse effect on diffusivity in the hydrophobised silica mesopores. Such unrestricted diffusion indicates lack of strong cation-silica interactions congruent with vibrational spectroscopic data and literature [48]. It appears also that the liquid phases outside and inside the mesopores have distinct dynamical properties, with a D_{cat} clearly higher outside in samples with pore filling of 200% and 400%. At this stage there is no clear explanation for this difference; although one can assume that it is related to locally different molecular ordering and/or different ionic densities inside

Table 4.1: *Self-diffusion coefficients (in units of 10^{-11} m^2/s) measured for samples of various pore fillings using selected ^1H resonances. [a] Data retrieved from a previous work, see reference [5]. * Estimated values based on certain assumptions (see SI of Paper II).*

Pore filling	D_{cat}	D_{NH}	D_{Im}	D_H	D_H/D_{cat}
0%	–	–	–	–	–
50%	0.95	n.a.	n.a.	–	–
100%	0.87	n.a.	n.a.	–	–
200%	1.63	2.31	2.25*	5.5 *	3.4*
400%	1.66	2.60	2.36*	7.2 *	4.3*
Im/PIL[a]	0.86	1.35	1.24	3.7	4.3

and outside of the microparticles.

Furthermore, the higher diffusivity values of the proton sitting on the -NH group, D_{NH}, compared to the diffusivity values of the imidazolium cations, D_{cat}, suggest the contribution from a proton motion decoupled from molecular diffusion, a transport mechanism different from the purely vehicular one. If we consider estimated values, the exchangeable protons on the -NH group diffuse, on average, faster than their parent molecules, in the hybrid materials investigated here about 3 to 4 times faster than the imidazolium cation (D_H/D_{cat}). This is very similar to the case described by Garaga et al. for the 10 nm large pores [5], and supports the idea presented in their work that the coexistence with mesoporous microparticles can result in enhanced dynamical effects in PILs.

The ionic conductivity of the PIL/silica hybrid materials studied in Paper II were characterised with broadband dielectric spectroscopy as well. The measured ionic conductivities of the samples are shown in Figure 4.3 A as a function of temperature in an Arrhenius plot. In all the studied PIL/silica hybrid materials, conductivity values have a non-linear dependence on inverse temperature, typical for ionic liquids, revealing that even though PFG-NMR indicated a decoupled proton motion, the vehicular mechanism is the dominating charge transport mechanism both in bulk and in confined Im/PIL mixture [102]. Accordingly, the VFT (Vogel-Fulcher-Tamman) equation was used to fit the experimental data points [102], and the fitted variables are summarised in Table 4.2. In the VFT equation, the parameter D is related to fragility while T_0 is a temperature related to the

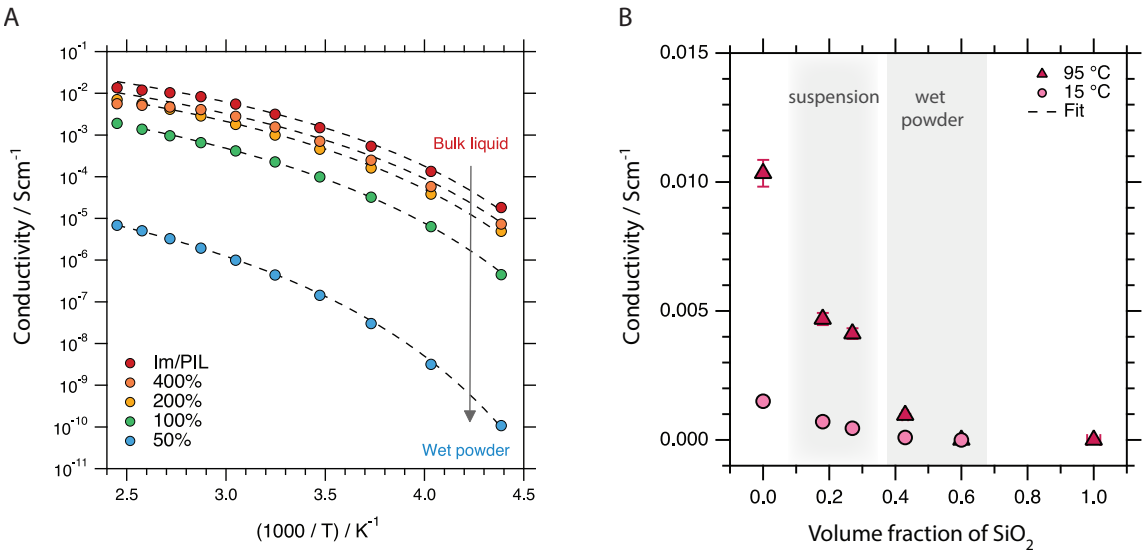

Figure 4.3: *A: Arrhenius plot of conductivity values measured for samples of various pore filling covering the temperature range from –50 to 145 °C. Dashed lines are simple guides to the eye. B: Absolute values of conductivity measured at 15 and 95 °C as a function of the volume fraction of silica.*

Table 4.2: *Values of D, T_0, and σ_∞, as found from fitting the conductivity data with the empirical VFT equation $\sigma_{VFT} = \sigma_\infty \cdot e^{-(DT0)/(T-T0)}$.*

Pore filling	Material Type	σ_∞ (Scm^{-1})	D (–)	T_0 (K)
0%	dry powder	–	–	–
50%	wet powder	0.0002	4.5	175
100%	wet powder	0.03	4.7	155
200%	suspension	0.10	4.3	157
400%	suspension	0.13	4.6	155
Im/PIL	liquid	0.20	4.0	157

glass transition temperature T_g, and σ_∞ is the conductivity extrapolated to infinite temperature. While D does not change significantly with composition and value of T_0 is also very little dependent on the degree of pore filling, σ_∞ drastically decreases with decreasing amount of the liquid phase in the entire studied temperature range. The decreasing conductivity upon higher volume fraction of silica is better illustrated in Figure 4.3 B, for the arbitrarily selected temperatures of 15 °C and 95 °C. This sharp drop of conductivity is significant even after compensation for the molar concentrations and may be attributed to changed or lost connectivity between the ionic species. This might occur at different extent depending on the pore filling ratio, since even at high Im/PIL mixture content the solid phase of porous silica creates longer and likely tortuous ion diffusion pathways while at low pore filling ratios additional discontinuities appear in the longer spatial range as the microcavities between particles remain unfilled.

The effect of confinement on the charge transfer properties and electrical double layer of the PIL, HC_8imTFSI, was studied in the above introduced nanochannels as well, presented in Figure 4.2 and here in Figure 4.4, also discussed in detail in Paper IV. For this, EIS (electrochemical impedance spectroscopy) experiments were performed in a three-electrode cell in which the bulk ionic liquid functioned as electrolyte ensuring contact between the reference electrode and the working electrode. Two different working electrodes were used: i) a bare ITO surface, serving as reference sample and ii) an ITO surface on which a thin film of mesoporous silica had been deposited, containing vertically aligned channel-like pores with an estimated diameter of 3.5 nm. While here the most important findings on charge transfer properties are discussed, the next subchapter (Supchapter 4.1.3) covers the capacitive behaviour of the PIL in the confined space defined by the nanochannels.

EIS results show that within the frequency window 10^{-2} – 10^6 Hz, the Nyquist plot of *Z"* versus *Z'* does not show full semi-circles, and the values obtained for the ITO covered with the thin silica film are lower, Figure 4.5 A. The frequency

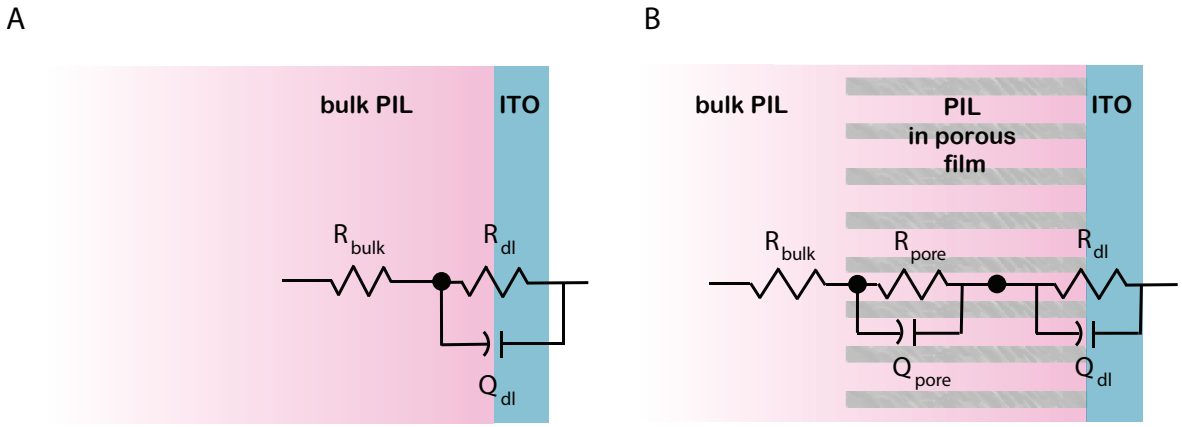

Figure 4.4: *The equivalent circuits used to model the impedance data recorded for the case of a bare ITO interface (A) and an ITO surface covered with a thin film of mesoporous silica containing nanochannels (B).*

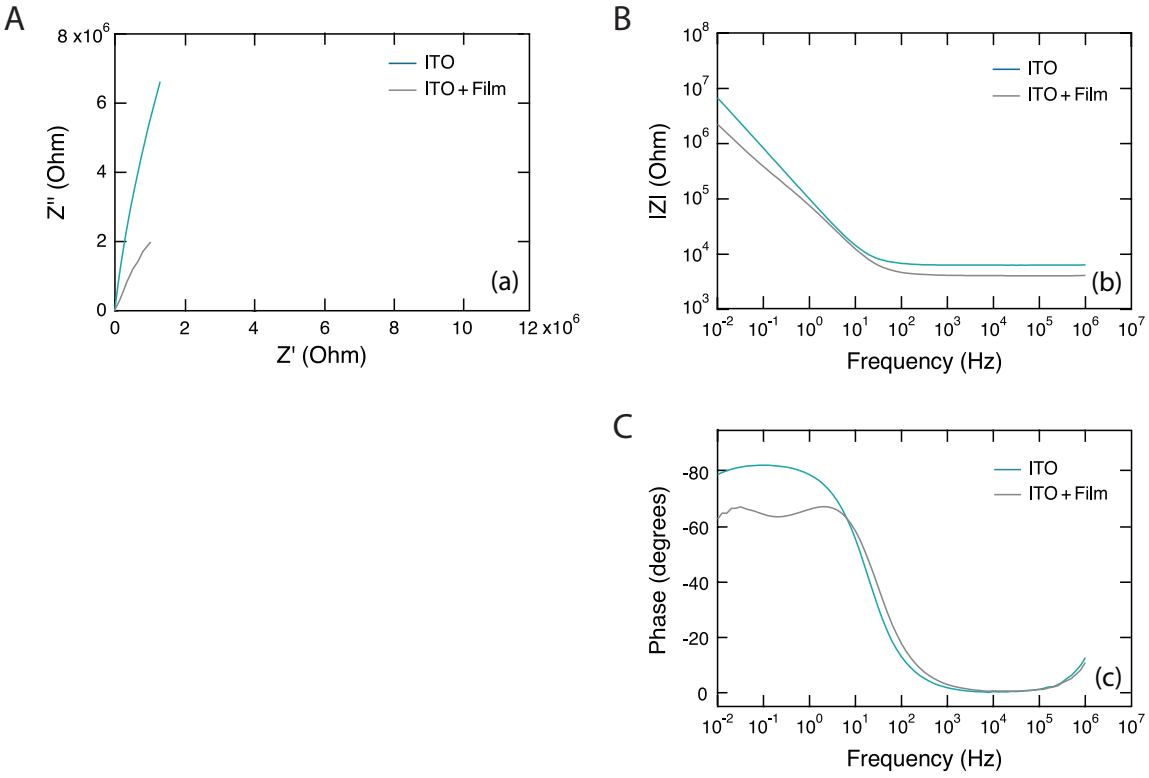

Figure 4.5: *Results from electrochemical impedance spectroscopy (EIS) measurements showing the Nyquist plot of Z" versus Z' (A) and the Bode plot of the modulus of Z as a function of frequency (B) and the frequency dependence of the phase angle (C).*

dependence of the modulus of Z, $|Z|(\nu)$, is shown in Figure 4.5 B in a log ($|Z|$) – log (ν) plot, revealing a linear behaviour below 10^1 Hz and constant values above 10^2 Hz. This plateau in the high-frequency region corresponds to the resistance in the bulk phase of the ionic liquid, while the slope is associated to phenomena occurring at the PIL/ITO interface.

The dependence of $|Z|$ on frequency has been modelled using equivalent circuits, which are illustrated in Figure 4.4, and the fitted parameters are presented in Table 4.3. The equivalent circuit describing the bare ITO surface in contact with the PIL, HC_8imTFSI, can be simplified to only include a bulk resistance (R_{bulk}), and a constant phase element (Q_{dl}) in parallel with a polarisation resistance (R_{dl}). For suitable evaluation of the EIS spectra obtained with the ITO electrode covered by a film of mesoporous silica, it was found that additional elements had to be included in the modelling equivalent circuit. The need of including the additional elements in the equivalent circuit, and thus of time constants, is visible also in the frequency dependence of the phase angle by the deviation from the angle of -80° for the case of ITO with the deposited thin mesoporous film, see Figure 4.5 C. First, an equivalent circuit was considered that is based on the work of Hirschorn et al. [89], suitable to model the surface and normal distribution of time-constants, as presented in Figure S7 in the SI of Paper IV. In the studied PIL/silica hybrid material this distribution originates from the presence of the thin film covering the whole electrode surface and its channel-like pores normally oriented with respect to the flat surface of the electrode. The fitting results have shown that the calculated capacitive contribution of the bulk silica is extremely low (0.0046 μF) and its resistance extremely high (7.5 GΩ), thus the silica component can be neglected and the equivalent circuit can be reduced to the one shown in Figure 4.4 B (the fitting results are also summarised in Table 4.3).

The high value for the in-pore resistance (R_{pore} = 94.4 kΩ), compared to the bulk resistance (R_{bulk} = 4.5 kΩ), can be rationalised by considering that both ions in the core of the channel and ions interacting with the negatively charged silica walls contribute to this fitted parameter. Thus, the high in-pore resistivity proposedly relate to the reduced mobility of ionic liquids in the confining space of hydrophilic silica pores as a consequence of strong interactions between the pore wall and the ions. This has been reported in other IL/silica systems as well, in which the silica pore walls have hydrophilic character [46, 47, 100].

Since PILs are promising candidates for use in proton conducting membranes, their confinement in porous matrices is a strategy to bring them in the solid state and make them useful in electrochemical devices avoiding the issue of leakage. It is worth to mention that there are means to decrease the high in-pore resistance. A straightforward method is the hydrophobisation of the silica walls as it is known that the ionic species of an ionic liquid close to a hydrophobic surface (e.g. modified silica or carbon based tubes) experience weaker interactions and display higher mobility [5, 46–48]. Nevertheless, the presented PIL/silica hybrid

Table 4.3: *Electrochemical parameters estimated by analysis of EIS data for the PIL, HC_8imTFSI, in contact with a bare ITO surface or an ITO surface on which a mesoporous thin film of silica had been deposited (ITO + Film). Note: for the "ITO + Film" case, the porosity was estimated to be 0.57, based on geometrical considerations and GISAXS results, see also Figure S5 in the SI of Paper IV.*

Working electrode	R_{bulk} (kΩ)	R_{pore} (kΩ)	Q_{pore}; (α) ($\Omega^{-1}s^{\alpha}$)	R_{dl} (MΩ)	Q_{dl}; (α) ($\Omega^{-1}s^{\alpha}$)	C_{dl}^{s} ($\mu F/cm^2$)
ITO	6.80			89.0	$1.89{\cdot}10^{-6}$ (0.91)	6.43
ITO + Film	4.50	94.43	$5.59{\cdot}10^{-6}$ (0.90)	8.33	$3.96{\cdot}10^{-6}$ (0.84)	16.29

material containing straight, vertically aligned channel-like pores with a narrow pore-size distribution can be of scientific interest since they enable studying the dynamics of truly and exclusively in-pore ionic species (unlike the case of ionogels or IL-filled mesoporous silica particles in which it can be experimentally difficult to discriminate between ions residing inside and outside the pores as in Paper II) [103].

4.1.3 Capacitive behaviour

Beside studying in-pore charge transfer properties, the electrochemical parameters estimated by equivalent circuit modelling presented in Figure 4.4 and in Table 4.3 (discussed deeper in Paper IV), lead to key findings also on the electrical double layer and the related capacitive behaviour of the PIL, HC_8imTFSI, at the bulk PIL/ITO interface and at the in-pore (nanoconfined) PIL/ITO interface.

The EIS data of the reference sample, bare ITO surface in contact with the PIL, HC_8imTFSI, has been modelled with an equivalent circuit containing a constant phase element Q_{dl} ($1.89\ 10^{-6}\Omega^{-1}s^{\alpha}$, $\alpha = 0.91$), presented in Figure 4.4, from which based on the work of Hirschorn et al. [89], the effective capacitance (C_{dl}) can be estimated using the following relation:

$$C_{dl} = Q_{dl}^{1/\alpha} \cdot \left(\frac{1}{R_{bulk}} + \frac{1}{R_{dl}} \right)^{(\alpha-1)/\alpha} \quad (4.1)$$

This yields a capacitance value of 1.26 μF, which translates into a specific capacitance $C_{dl}{}^{s}$ of 6.43 $\mu F/cm^2$. If the value of 12.16 for the dielectric constant

(ϵ_{PIL}) of the protic ionic liquid HC_8imTFSI is assumed, based on the work of Rybinska-Fryca et al. [104], the thickness (d) of the electric double layer at the ITO interface can be estimated to be 1.7 nm, using the relation

$$C_{dl} = \epsilon_0 \cdot \epsilon_{PIL} \cdot \frac{A}{d} \tag{4.2}$$

Interestingly, this is comparable to the length of the chain-chain nanosegregation observed in bulk HC_8imTFSI by Abdurrokhman et al. [2].

The specific capacitance of 6.43 μF/cm^2 obtained at the bulk PIL/ITO interface is comparable to the values reported in the literature for a variety of other ionic liquids. A comprehensive investigation of the electrochemical properties of a series of PILs has been reported by Lu et al. [105], in which the authors report a double layer capacitance of 15.3 μF/cm^2 using a glassy carbon (GC) working electrode for the protic ionic liquid (Et_2NH)(($BuO)_2POOH$). Another relevant study has presented the use of a (PET)ITO–ionic liquid–ITO(PET) system for sensing changes in mechanical pressure (PET is polyethylene terephthalate)[106]. In that study, the used ionic liquid was 1-butyl-3-methylimidazolium bistriflimide (more precisely, a filter paper imbibed with this ionic liquid, which introduces uncertainty in the contact area and specific capacitance) and the measured capacitance varied between ca. $4{\cdot}10^{-7}$ F for an applied pressure of 10 kPa and ca $3{\cdot}10^{-6}$ F for an applied pressure of 20 kPa.

Similarly to the bulk PIL/ITO interface, the effective double layer capacitance (C_{dl}) at the in-pore PIL/ITO interface has been determined with Equation 4.1, from the CPE element (Q_{dl}), to be 1.8 μF. This can be expressed as a specific capacitance considering that approximately 57% of the total ITO area is exposed to the in-pore ionic liquid phase during the EIS measurement (the porosity of 0.57 has been calculated from geometrical considerations and using structural parameters achieved from GISAXS studies, see Figure S5 in the SI of Paper IV) leading to a value of ca 16 μF/cm^2. Compared to the specific capacitance at bulk PIL/ITO interface (6.43 μF/cm^2), the increased specific capacitance upon nanoconfinement at the in-pore IL/ITO interface suggests a higher charge density within the dielectric double layer. Assuming the local molecular organisation within the pores described above (in Subchapter 4.1.1) it is plausible that the reduced pore width and the presence of oriented and immobile octyl chains induce the mobile cations to adopt a preferred vertical orientation at the ITO interface, with a consequent increased ion density.

Increased capacitance values for ionic liquids in a confined space have been reported by several authors for porous electrodes with unimodal and well-defined pore widths [56, 107–109]. In general, the presented specific capacitance values are in fair agreement with those measured for other ionic liquids; for instance a specific capacitance of ca 7 μF/cm^2 has been measured in ethyl-methylimidazolium-TFSI confined in porous carbon electrode containing 1 nm wide nanopores [56]. Also, various studies have reported ion-exclusion effects as well as denser ionic packing

at the electrode interface for the case of ionic liquids in nano-domains, which may explain our observation of an increased specific capacitance.

It is worth to mention that studying the behaviour of ionic liquids in the nano-space of electrodes, for applications in supercapacitors, is a topic of increasing research interest. By date, related publications have only studied experimentally the capacitive behaviour of short-chain ionic liquids in confinement while in the context of nanoconfinement surface active ionic liquids (SAILs) can be especially interesting as their polar/apolar nanosegregation is comparable to the size of the confining space. As reported for bulk aprotic SAILs, they show distinct ion distribution at the electrode/electrolyte interface which can depend on applied voltage, temperature, and based on computational methods on the geometry of the electrochemical cell [3, 53, 54, 110]. Next to possessing a long alkyl chain (and belonging to the group of SAILs) the studied HC_8imTFSI also belongs to the group of protic ionic liquids, yet another group of ionic liquids that have attracted recent interest for use as capacitor electrolytes. Indeed, they are typically cheaper than aprotic ionic liquids, safer than organic solvent-based electrolytes and still provide wider electrochemical windows than aqueous electrolytes.

4.2 Nanochannel formation with SAILs

This chapter is based on two related studies of aprotic SAIL/silica hybrid materials presented in Paper I and Paper III. In Paper I the possibility of templating a silica thin film with a SAIL, C_{16}mimCl, during EASA method is presented for the first time, focusing on the characterisation of the obtained mesoporous morphology, studying different compositions of the synthesis solution, and discussing important IL-silica interactions related to the observed molecular templating. Consecutively, in Paper III the limitations of this synthesis have been investigated with respect to decreasing the chain length of the SAIL ($C_n$mimCl, $n = 16, 14, 12$) and mixing the templating C_{16}mimCl with its protic analogue, HC_{16}imCl, in the synthesis solution.

The systematic change in the composition of the synthesis solution used during silica deposition with the EASA method resulted in changed chemical and morphological properties of the deposited thin film, discussed in both Paper I and Paper III and here summarised in Figure 4.6. It has been observed that C_{16}mimCl is a suitable molecular template to form vertically-aligned, hexagonally ordered channel-like mesopores in silica films deposited with EASA, thus the thin films with such structures are labelled "hexagonal". In addition, the templating SAIL, C_{14}mimCl, still results in the formation of hexagonally ordered pores, while the abrupt loss in templating function has been observed upon further decrease of the chain length to C_{12}mimCl. Similarly, when the templating SAIL, C_{16}mimCl, was mixed with its protic analogue, HC_{16}imCl, in the synthesis solution at different ratios, the increased ratio of the protic ionic liquid resulted in loss of templated,

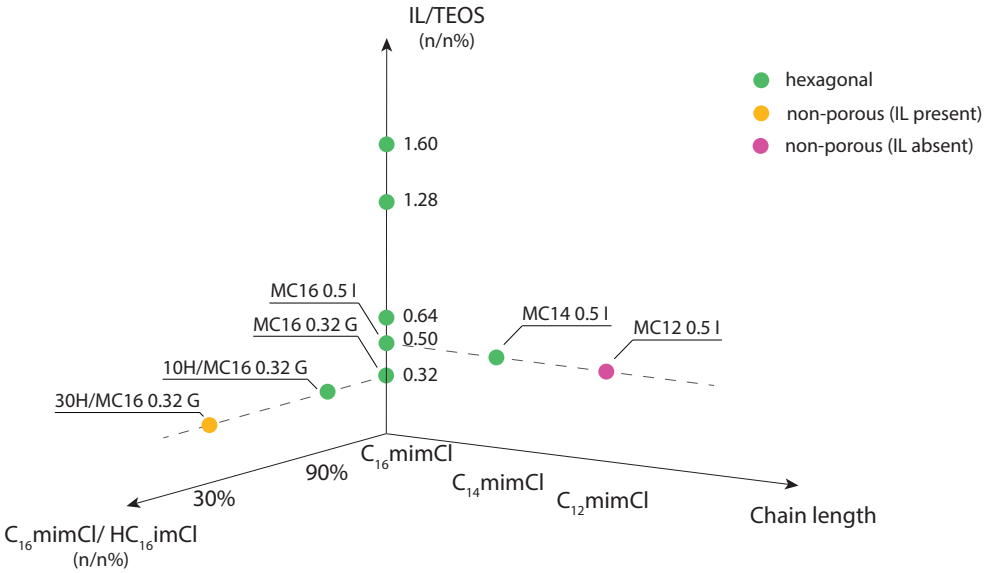

Figure 4.6: *Summary of the obtained pore structures in silica thin films deposited via EASA method from synthesis solutions with varying compositions labelled with their sample names (based on Paper I and Paper III).*

porous structure. While the in detail chemical characterisation, based on IR and XPS measurement results, are presented in Subchapter 4.2.1, the morphology of the deposited film is treated in Subchapter 4.2.2. Additionally, possible template-silica interactions are discussed in Subchapter 4.2.3.

4.2.1 Limitations in chemical composition

Based on the elemental analysis done with XPS measurements (discussed in Paper I and its results summarised in Table S3 in the SI of Paper I), the chloride anion of the templating ionic liquid, C_{16}mimCl, was undetectable in the silica thin films deposited from the synthesis solutions with IL/TEOS molar ratios between 0.32 and 1.28, which formed the typical hexagonal pore structure (Figure 4.6). Besides, in the IR spectra of these samples after extraction, the ν_{O-H} ($\sim$ 3400 cm^{-1}) stretching vibration peak appeared while at the same time the intensity of the ν_{Si-OH} ($\sim$ 950 cm^{-1}) stretching vibration has also increased, reflecting a higher abundance of silanol bonds (Si-OH) in the extracted films, see Figure 6 A in Paper I. Based on these XPS and IR results, it can be assumed that the silanol groups on the silica pore wall of the as-synthesised thin films are deprotonated, having their negative charges neutralised by the $C_{16}mim^+$ cations, as schematically depicted in Figure 4.7. It can also be assumed that at the extraction step, during which the films were treated with hydrochloric acid solution and resulted in the removal

of the $C_{16}mim^+$ cation, the negatively charged silica wall got protonated leading to the intensity rise of the ν_{Si-OH} peak. In addition, dangling silanol groups can be located not only on the pore walls, but also in the bulk silica phase since the ν_{Si-OH} ($\sim$ 950 cm^{-1}) stretching mode was visible in both extracted and non-extracted samples. The full removal of $C_{16}mim^+$ *via* extraction can be confirmed by IR as the alkyl chain ν_{C-H} stretching vibrations (2960 – 2855 cm^{-1}) and the imidazolium ring δ_{ring} bending vibrations (1570 cm^{-1}) disappear from the IR spectra of the extracted samples, Figure 6 A in Paper I. Note that the same method was used in Paper III as well (see here Figure 4.8 and Figure S3 in the SI of Paper III). This also shows that in the hexagonal structure, the $C_{16}mim^+$ cations are located only in the mesochannels of the films and do not get entrapped in the bulk silica network.

Similar to the C_{16}mimCl-templated silica thin films with hexagonal pore structure, the IR spectra of C_{14}mimCl-templated films before and after extraction confirm the presence of the ionic liquid in the film (proposedly the presence of its cation) and its removal by extraction, which indicates that instead of being immobilised in the silica network, it forms pores being accessible to the extraction solution, Figure 4.8 A. Contrarily to the cases of C_{16}mimCl and C_{14}mimCl, the shorter chained ionic liquid C_{12}mimCl was not incorporated in detectable amounts into the silica thin film during EASA, as can be concluded from the absence of its characteristic peaks in the Infrared spectrum of the corresponding film, both before and after extraction. This already indicates a limitation in templating function upon decreasing the chain length of the alkyl-methylimidazolium ionic liquid and therefore in forming a SAIL/silica hybrid material with C_{12}mimCl *via* EASA.

The strong absorption peaks arising from the hexadecyl-chain appear also in the Infrared spectra of thin film samples prepared with varying HC_{16}imCl/C_{16}mimCl ratios; however the presence of the protic ionic liquid HC_{16}imCl could not be explicitly confirmed in samples 10H/MC16 0.32 G NE and 30H/MC16 0.32 G NE, Figure 4.8 B. Nevertheless, the spectra presumably indicate the presence of $C_{16}mim^+$ cations within the structure, that disappear upon extraction revealing

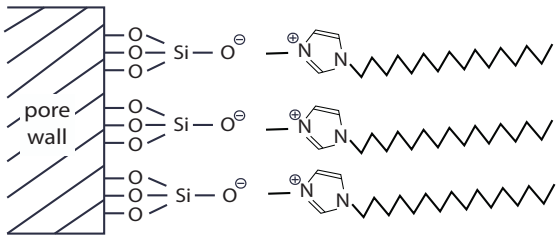

Figure 4.7: *Schematic of the proposed neutralisation of the negatively charged silica wall by the $C_{16}mim^+$ cations located in the nanohannels of the IL-templated silica thin films.*

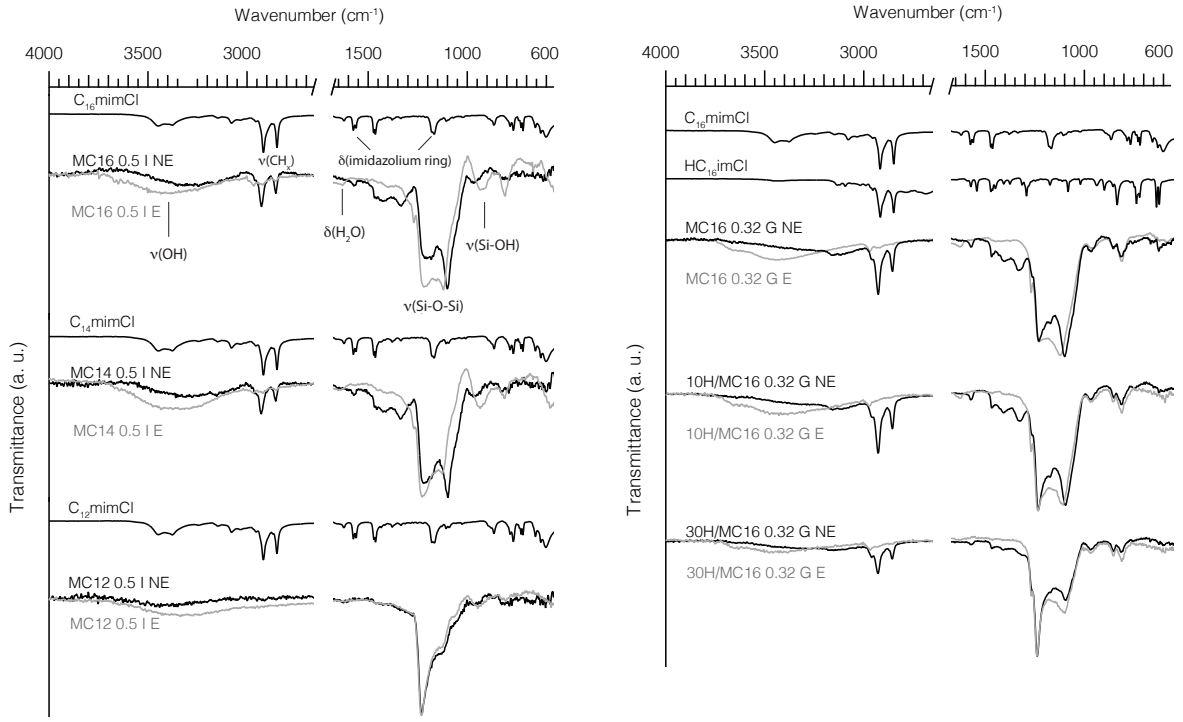

Figure 4.8: *A: Infrared spectra of the silica thin films deposited with EASA method using alkyl-methylimidazolium ionic liquids with varying chain lengths in the synthesis solution. B: Infrared spectra of the silica thin films deposited with the EASA method using mixtures of $HC_{16}imCl$ and $C_{16}mimCl$ with varying molar ratios in the synthesis solution. The annotation "NE" stands for samples before extraction (i.e., not-extracted) while "E" stands for extracted samples, in both graphs.*

that the incorporated ionic liquid is not immobilised within the silica network.

The Infrared spectra obtained on thin films, reported in both Paper I (see Figure 6 in Paper I) and Paper III (see here Figure 4.8 and Figure S3 in the SI of Paper III), have revealed an amorphous structure of the deposited silica films regardless of the initial composition of the synthesis solution. However, distinct differences can be observed in the spectral region between 1250 and 1000 cm^{-1}, a region characteristic of sol-gel derived silica networks, indicating differences in the network structure dependent on the film having hexagonal pore structure or not. It is worth to note, that even though a detailed description of the structural features of the synthesised silica networks can be retrieved from the recorded Infrared spectra, the peak assignment of the 1250-1000 cm^{-1} region is not straightforward and in some aspects still debated [111–114]. The most noticeable difference is the decrease of the absorption peak at 1100 cm^{-1} in the spectrum of the MC12 0.5 I NE sample and 30H/MC16 0.32 G NE samples, Figure 4.8. This peak is characteristic of the stretching modes of siloxane bonds in linear silica units, as

shown in an *in situ* Infrared spectroscopic study on silica condensation which has revealed that as the condensation proceeds the stretching vibration peak of linear silica units decreases simultaneously to the increase of the absorption peak at 1200 cm^{-1}, attributed to the stretching modes of six-fold silica rings [113]. Therefore, it can be proposed that the higher ratio between the Infrared absorption at 1200 cm^{-1} and that at 1100 cm^{-1} indicates that the MC12 0.5 I NE sample consists of a more condensed and/or continuous silica network than the films with hexagonally ordered pores, namely C_{16}mimCl-templated films presented in both Paper I and Paper III and the C_{14}mimCl-templated film (sample MC14 0.5 I). A similar difference between the Infrared spectra of 10H/MC16 0.32 G NE and 30H/MC16 0.32 G NE samples has been observed in parallel with the loss of hexagonal pore structure of the film upon increased ratio of HC_{16}imCl.

4.2.2 Morphology and permeability

Based on morphological characterisation with GISAXS and electron microscopy beside complementary measurements with cyclic voltammetry, presented in detail in Paper I and Paper III, the formation of vertically-aligned, hexagonally ordered mesoporous channels running through the entire silica film thickness were observed in C_{14}mimCl- and C_{16}mimCl-templated films and in the 10H/MC16 0.32 G NE sample (this pore structure is labelled as "hexagonal" in Figure 4.6). In contrary, samples MC12 0.5 I NE and 30H/MC16 0.32 G NE have shown a non-porous structure.

This difference can be well characterised with GISAXS and its results are in line with the above presented IR results. Among the scattering intensities presented in Figure 4.9 (and Figure 4 in Paper I), the films possesing hexagonal pore structure show the following characteristic scattering intensity peaks with the associated Miller indices of the long-range hexagonally ordered pore structure: q_1*(10)*, q_3*(11)*, q_4*(20)*, and q_5*(21)*, with their peak position ratio of $1{:}\sqrt{3}{:}\sqrt{4}{:}\sqrt{7}$ characteristic of the hexagonal p6m symmetry of the channel-to-channel spacing [115, 116]. The cell parameter of the C_{16}mimCl-templated silica films is around 4.4 nm, while the change of the tamplating ionic liquid to C_{14}mimCl resulted in a cell parameter decreased to 4.0 nm. The ratios of the scattering intensities of the (11) and (20) reflections (i.e., the ratio *I(11)/I(20)*) are very close in the C_{16}mimCl- and the C_{14}mimCl-templated films (1.01 and 1.11 respectively, see Table S1 in the SI of Paper III), from which it can be concluded that in these films the morphology of the pores and the silica walls are similar; the only difference being the smaller unit cell parameter and hence an overall smaller pore structure in the C_{14}mimCl-templated film [117]. In addition, the scattering intensity peaks superimposed on the peaks of the planar hexagonal lattice reflections, namely the peaks labeled q_2 and q_6 in Figure 4.9, originate from the porous silica particles located on top of the film's surface [31, 116]. The formation of such particles is common during the

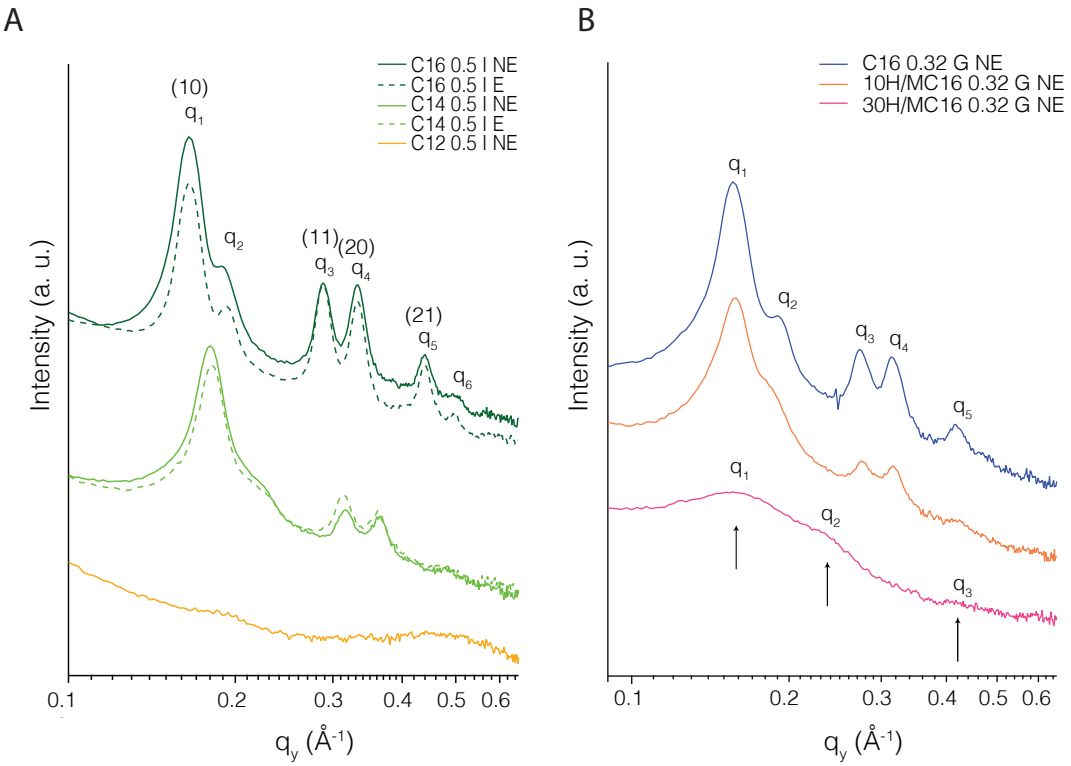

Figure 4.9: *A: X-ray scattering intensities integrated along the horizontal axis attained from the 2D scattering patterns recorded on different mesoporous silica deposited with EASA method using alkyl-methylimidazolium ionic liquids with varying chain lengths in the synthesis solution. B: X-ray scattering intensities integrated along the horizontal axis of the 2D scattering patterns of mesoporous silica thin films deposited with the EASA method in the presence of varying $HC_{16}imCl/C_{16}mimCl$ mixtures. In case of both graph A and graph B the annotation 'NE' stands for samples before extraction (i.e. not-extracted) and 'E' for samples after extraction.*

EASA synthesis of silica thin films, as a consequence of the pH gradient formed at the surface of the working electrode that cause condensation of silica also in the bulk of the synthesis solution close to this surface [116].

Different from the C_{14}mimCl- and C_{16}mimCl-templated films, the use of the shorter-chain SAIL, C_{12}mimCl, resulted in a silica film showing X-ray scattering pattern with lack of any of the intensity peaks characteristic of the hexagonally ordered, vertically aligned mesochannels, Figure 4.9 A. In the full scattering range of the C12 0.5 I NE sample only one weak-intensity ring has appeared with a peak maximum at 0.19 $Å^{-1}$ (d = 3.4 nm). The assignment of this peak is not straightforward as it can originate from both the silica network and the chain-chain separation of self-assembled ionic liquid, which may be present in trace amounts. Altogether, GISAXS and IR results suggest that the silica film deposited *via* EASA using C_{12}mimCl consists of amorphous and condensed, but non-porous silica without the incorporation of the ionic liquid.

The sample 30H/MC16 0.32 G NE also shows a different X-ray scattering pattern than the films with hexagonal pore structure. Even though the presence of the $C_{16}mim^+$ cation within the film can be assumed based on the Infrared absorption peaks of the alkyl chain, which disappear upon extraction indicating that the incorporated cations are not immobilised within the silica network, the X-ray scattering pattern does not show the formation of a hexagonal pore structure. Instead, very wide scattering intensity peaks with nanometre-scale correlation lengths of 4.0 nm, 2.7 nm, and 1.4 nm have been observed. These peaks can originate from the electron-density contrast of apolar/polar nanostructuration of self-assembled cations but also possible repetitiveness of these assemblies. Nevertheless, based on the chemical and morphological characterisation, it has been found that the protic ionic liquid $HC_{16}imCl$ does not function as a soft-templating agent during EASA of silica thin films.

Electron microscopic images of the $C_{16}mimCl$-templated silica thin films after extraction are shown in Figure 4.10, representative of the hexagonal pore structure observed by GISAXS. The TEM image of the cross-sectional sample prepared

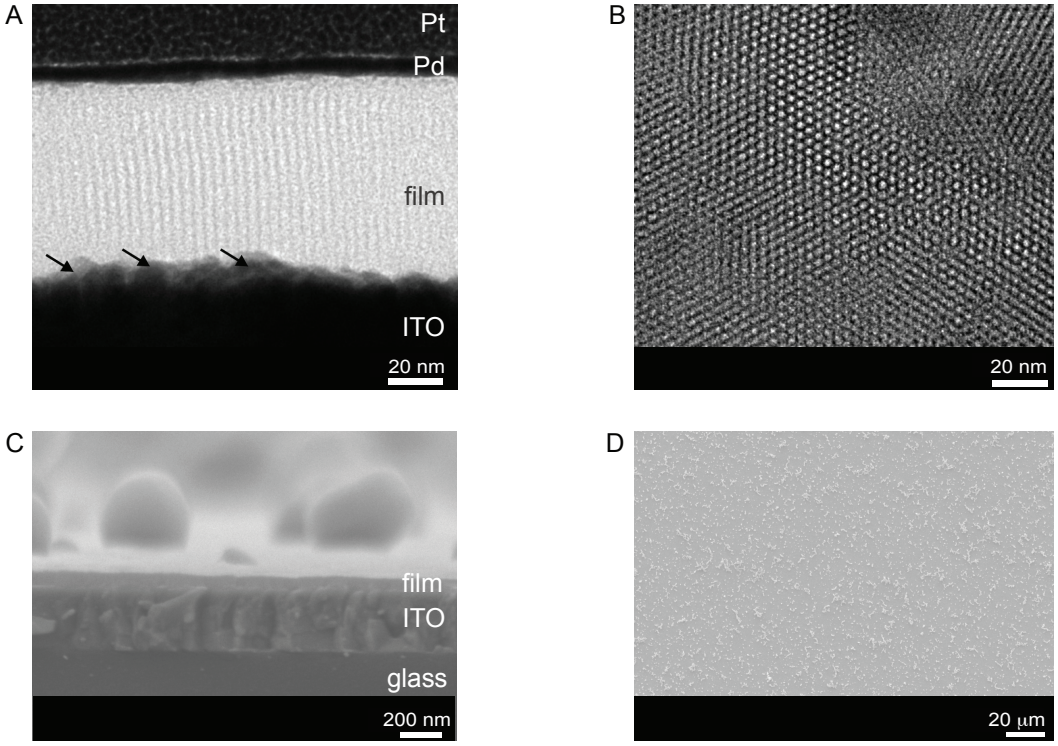

Figure 4.10: *Electron microscopic images of the $C_{16}mimCl$-templated silica thin films after extraction (Paper I). A: cross-sectional TEM image of the sample with IL/TEOS ratio of 0.32 prepared with the lift-out technique. The arrows point to the interface between the thin film and ITO; B: top-view TEM image of the sample with IL/TEOS ratio of 0.32; C: cross-sectional SEM image of the sample with IL/TEOS ratio of 0.32 on its substrate; D: top-view SEM image of the sample with IL/TEOS ratio of 0.32.*

with the lift-out technique, Figure 4.10A, shows that individual channels in the silica film are straight and vertical to the ITO substrate and can reach its surface in direct contact. Additionally, top view TEM image reveals that these channels are not only well-separated, but also hexagonally ordered throughout relatively large domains, Figure 4.10B. The pore width was determined with image processing to be approximately 2.5 ± 0.3 nm. Despite, channels with a similar pore width are called both mesochannels and nanochannels, here the term nanochannel is preferred expressing that the pore diameter is on the nanometre scale. Nevertheless, it has been found that the pore width of the channels is independent on the IL/TEOS ratio (here IL is C_{16}mimCl) used in the synthesis solutions and its size is similar to the size of two adjacent hexadecyl-tails. Thus, it can be assumed that the cations have a core-shell packing within the pores with the hydrocarbon tails forming the core and the charged heads located at the pore wall forming the outer shell [2, 94]. Furthermore, cross sectional SEM image shows that the IL-templated silica thin films are deposited as even, continuous layers without any cavities between the film and the ITO substrate, Figure 4.10 C. Based on the obtained SEM and TEM images the film thickness has been determined to be ca. 65 nm. In addition, on the SEM images the presence of nanoparticles on top of the films can be observed, Figure 4.10 C and 4.10. These are side products of the EASA process, and their presence has been described in the literature also in case of other films prepared *via* EASA [99].

As an additional characterisation method to study the permeability of the films and obtain further information on their channel-like pores, cyclic voltammetry with various redox probes has been applied, the results being presented in Figure 4.11 and Figure 4.12 here and Figure 7 in Paper I. The C_{16}mimCl-templated silica thin films containing hexagonally ordered nanochannels filled with the cation of the ionic liquid are not permeable to the positively charged $[Ru(NH_3)_6]^{3+}$ and negatively charged $[Fe(CN)_6]^{3-}$ redox-active complexes indicated by the lack of redox-peaks on their CV curves revealing that the diffusion pathway of these probes towards the ITO electrode is blocked. This also reveals that the deposited films covered the entire contact area. However, it has been found that the neutral redox probe, α-methylferrocenemethanol which contains a Fe(III)-ion complexed with cyclopentadienyl rings, is able to reach the ITO electrode giving rise to a shifted, but strong oxidation peak. This can be explained with its possible solubilisation in the apolar phase of the assembled cations located in the pores, also observed on CTAB-templated silica films deposited with the EASA method [85]. After extraction, i.e. removal of the cation from the nanochannels, the positive redox probe and the neutral redox probe can pass unhindered through the silica film *via* the emptied channel-like pores giving rise to reduction and oxidation peaks on their cyclic voltammetric curves, which resemble the current response measured with a bare ITO substrate. At the same time, the negative redox probe $[Fe(CN)_6]^{3-}$ could not reach the ITO electrode even after extraction,

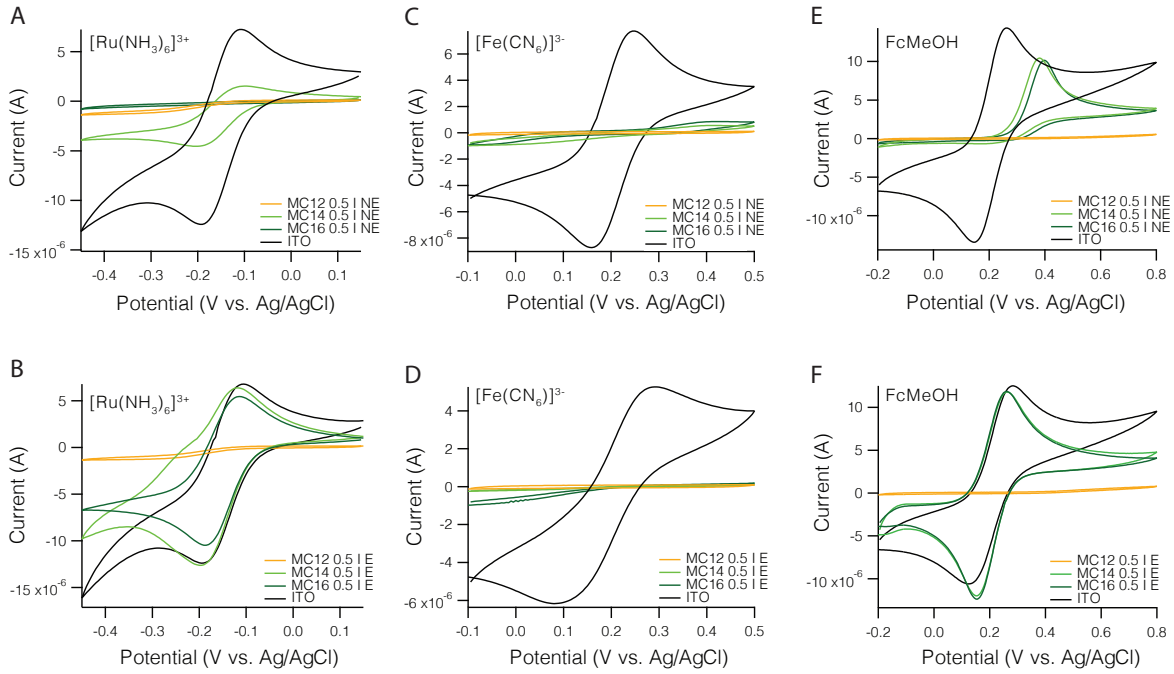

Figure 4.11: *Cyclic voltammetric curves recorded with the redox probe $[Ru(NH_3)_6]Cl_3$ (A-B), $K_3[Fe(CN)_6]$ (C-D), and FcMeOH (E-F) using a bare ITO electrode and ITO electrodes covered with mesoporous silica deposited in presence of alkylmethylimidazolium ionic liquids with varying chain lengths, before (A, C, E) and after (B, D, F) extraction of the ionic liquid.*

due to the negatively charged silica pore walls repelling this redox probe, also indicating a good coverage of the films [85].

Interestingly, even though the C_{14}mimCl-templated and C_{16}mimCl-templated silica thin films show similar Infrared spectra and X-ray scattering patterns, there is a difference in their cyclic voltammetric response. More precisely, the cyclic voltammetric curve obtained with the $[Ru(NH_3)_6]^{3+}$ redox probe on the non-extracted C_{14}mimCl-templated silica film (sample C14 0.5 I NE) shows small but measurable current peaks of reduction and oxidation, suggesting defects in the film, see Figure 4.11. Considering that the cyclic voltammetric curve of the neutral redox probe FcMeOH, obtained on the same sample, shows a shifted oxidation peak, reflecting a hindered diffusion, and that after extraction the $[Fe(CN)_6]^{3-}$ redox probe has not shown Faradic currents, it can be proposed that instead of larger damages (e.g. macroscopic scratches) the size of the defects in the film is rather comparable to the size of the used redox probes. Based on the work of Sibottier et al., it can indicate that the film is thinner and more permeable possibly due to a slower growth in the presence of C_{14}mimCl [118]. Cyclic voltammetric curves obtained on the C12 0.5 I sample before and after extraction, have also evidenced that the formation of a highly condensed, continuous silica film proceeds when the silica film is deposited *via* EASA in the presence of C_{12}mimCl. Independently

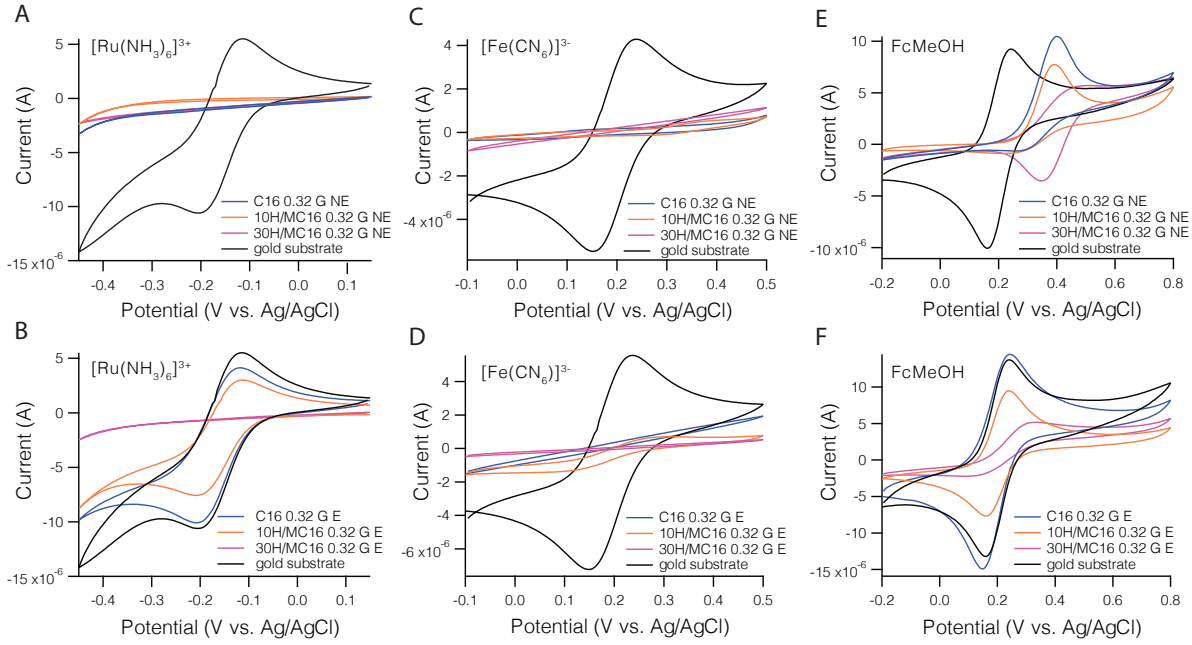

Figure 4.12: *Cyclic voltammetric curves recorded with the redox probe $[Ru(NH_3)_6]Cl_3$ (A-B), $K_3[Fe(CN)_6]$ (C-D), and FcMeOH (E-F) using a bare ITO electrode and ITO electrodes covered with mesoporous silica thin films deposited with the EASA method in the presence of varying $HC_{16}imCl/C_{16}mimCl$ mixtures, before (A, C, E) and after (B, D, F) extraction of the ionic liquid.*

of the type of redox probe used, no Faradic currents were measured neither before nor after the extraction procedure, revealing that the silica thin film acts as a fully covering insulator layer on top of the ITO electrode.

In addition, cyclic voltammetric measurements obtained on the 30H/MC16 0.32 G sample is in line with the Infrared and GISAXS studies. The lack of Faradic peaks on the CV curves reveal that even if the ionic liquid forms pores within the silica film, these do not extend through the entire thickness of the film as the pathway of the redox probes toward the ITO electrode is hindered, Figure 4.12.

4.2.3 Possible interactions during templating

As revealed by the morphological characterisation reported in Paper I and Paper III, C_{14}mimCl and C_{16}mimCl form hexagonally ordered, vertically oriented, channel-like pores in EASA-deposited silica films. This is similar to the hexagonal pore morphology formed by TTAB (tetradecyltrimethylammonium bromide) and CTAB (cetyltrimethylammonium bromide) during silica deposition *via* EASA, previously reported by Walcarius et al. [99, 119, 120]. The similarity of the two groups of amphiphiles, one with imidazolium the other with ammonium head, is intriguing. It is known that the morphology of the silica films deposited with

CTAB is extremely sensitive to synthesis parameters like TEOS concentration, type and amount of co-solvent, salt composition and concentration, which all were studied in detail before fine-tuning them as all of them can influence the self-assembly of CTAB both in bulk and at the electrode surface during deposition [99]. Meanwhile, the study presented in Paper I and Paper III shows that for a selected set of synthesis parameters, the use of the ionic liquid C_{14}mimCl and C_{16}mimCl results in the same hexagonal pore morphology of the film with the only difference that a higher voltage had to be applied during EASA [116, 120]. Similarly, formation of such hexagonal structure has not been viable with either C_{12}mimCl or DTAB (dodecyltrimethylammonium bromide), which instead resulted in silica films not mesostructurally ordered [99]. These similarities indicate that self-assembly of C_{14}mimCl and C_{16}mimCl, and therefore supposedly also their packing parameter, is very similar to that of TTAB and CTAB under the synthesis conditions of EASA and that imidazolium SAILs can be used as templating agents for the formation of nanochannels just as successfully as the members of the TAB family.

Furthermore, in-depth characterisation of the C_{16}mimCl-templated silica thin films presented in Paper I led to the hypothesis that electrostatic attraction appears between the pore forming $C_{16}mim^+$ ions and the negatively charged silica pore wall, which reasonably originates from the electrostatic attraction between the $C_{16}mim^+$ and the network-forming negatively charged silicate oligomers. This is in line with that condensation of the silica network proceeded at basic pH. Furthermore, it can be proposed also that the described electrostatic attraction is the main so-called cooperative interaction during pore formation as C_{16}mimCl and CTAB form nanochannels with high curvature at the same range of template-to-precursor ratios in the synthesis solution. This also suggests that the hydrogen bonds and π-π interactions, which the aromatic imidazolium head is able to establish, remain secondary under the reaction conditions of silica deposition *via* the EASA process. The fact that a protic ionic liquid, HC_{16}imCl, has a negative effect on the pore ordering, discussed in detail in Paper III, and is not able to contribute with an own templating function is in agreement with this as the inefficiency in templating may be correlated to the electrochemical instability of this protic ionic liquid. More specifically, the cathodic potential used for deposition can possibly cause the reduction of the imidazolium cations resulting in loss of their charges and ability to establish cooperative interaction with the silicate oligomers. This hypothesis is raised based on the recorded chronoamperogram during deposition (see Figure 7 in Paper III).

5 Conclusions and outlook

This thesis presents studies of IL/silica hybrid materials made of amphiphilic imidazolium ionic liquids and mesoporous silica. Paper II presents an in-depth study of an imidazole/PIL mixture confined in hydrophobised mesoporous silica microparticles with narrow pores only 5 nm wide, focusing on proton transport mechanisms and correlated local structures. BDS results show that the macroscopically measured ionic conductivity in the hybrid materials is dominated by the vehicular mechanism. Nevertheless, PFG-NMR results also reveal the occurrence of proton motion decoupled from the imidazolium cation that, due to issues of line broadening, could not be investigated for the samples with filling factors of 50 and 100%. In case of the samples with filling factors higher than 100% (in which the Im/PIL mixutre is in excess and located also in between the microparticles) both average proton and ion mobility is enhanced. Nevertheless, the question whether a decoupled proton motion also occurs inside the nanopores remains open. This study also presents that interactions at the molecular level are practically unchanged upon confinement in hydrophobised silica mesopores as compared to the bulk. As the results are in line with those previously reported by Garaga et al. [5], it is assumed that even in the small pores only 5 nm wide the flipped-ion effect occurs. In practice, this effect involves the orientation of non-polar alkyl chain towards the hydrophobic silica pore wall. In such structuration there are weak cation-silica interactions that favor unrestricted diffusion, which is otherwise hindered under the nanoconfinement in untreated, hydrophilic silica pores.

Electrochemical properties of the same PIL in bulk and inside hydrophilic silica nanochannels, with an approximate pore diameter of 3.5 nm, have been presented as well in this thesis, Paper IV. BDS results have revealed that ion conduction in the pure, bulk PIL is dominated by the vehicular mechanism. Besides, the equivalent circuit modelling of the EIS results of bulk and confined PIL have been discussed, revealing higher resistance of the ionic liquid inside the hydrophilic silica nanochannels, which reflects hindered diffusion due to a strong interaction of cations with the negatively charged silica wall. Nevertheless, an enhanced capacitance has also been observed at the in-pore PIL/electrode interface which suggests denser ion packing and higher charge density. This can be attributed to the nanoscale of the pores concomitant to the ability of this ionic liquid to self-assemble according to its amphiphilic nature.

In addition, the use of Im-SAILs as soft-templates for mesoporous silica syn-

thesis has been discussed in Paper I and Paper III. The presented studies extend the possibilities and show the limitations and plausible mechanism of templating silica with Im-SAILs, which is relevant in developing methods for synthesis of ionic liquid-based functional hybrid materials. In our approach, a series of aprotic Im-SAILs and one protic SAIL were studied as possible templates during the deposition of silica thin films with the EASA method. It has been found that C_{14}mimCl and C_{16}mimCl are suitable soft-templates for the formation of vertically aligned, distinct nanochannels with a well defined pore size and a highly packed hexagonal arrangement. Moreover, these nanochannels run through the entire film thickness enabling mass transport through the film and a robust contact with the substrate after removal of the templating ionic liquid. By contrast, C_{12}mimCl and the protic analogue HC_{16}imCl have not shown molecular templating function under the same synthetic conditions used with C_{16}mimCl. Important information on the underlying mechanism of pore formation has been gained as well; based on Paper I, the presented study has revealed electrostatic attraction between the pore forming $C_{16}mim^+$ ions and the negatively charged silica pore wall. This can reasonably originate from the electrostatic attraction between the $C_{16}mim^+$ and the network-forming negatively charged silicate oligomers and this electrostatic attraction is proposed to be the main cooperative interaction during pore formation. Meanwhile, the results of both Paper I and Paper III also indicate that hydrogen bonds and π-π interactions, which the imidazolium head is able to establish, remain secondary during synthesis.

The results obtained through all these studies can inspire further research on new ionic liquid-based functional hybrid materials. Important aspects on designing PIL-based hybrid materials have been revealed. When the desired function of an amphiphilic PIL is to be an electrolyte in a capacitor, pore size of the electrode is an important parameter to consider as increased specific capacitance has been observed in a confining space comparable to the size of the PIL, based on Paper IV. Besides, fast charge transport in the PIL is desired for high power density in possible applications in electrochemical devices such as supercapacitors and fuel cells, in which PILs are used as ion conductors. Based on Paper II and Paper IV, lack of strong interactions between the confining solid state matrix and the PIL is beneficial for unhindered diffusion of ionic species, especially important when the charge transport proceeds through the vechicular mechanism. Based on the revealed possibilities and limitations of preparing an IL/silica hybrid material in a one-step method using the IL as soft-template, presented in Paper I and Paper III, the strong silica-IL interactions, which are essential to form the hybrid material, limit possible applications to the ones in which high mobility of ions is not a requirement. Nevertheless, the obtained knowledge on the silica-templating mechanism of the imidazolium ionic liquids is beneficial for future works considering to synthesise and use IL/silica hybrid materials.

6 Acknowledgements

Funding from the Swedish Foundation for Strategic Reserach (SSF, grant no FFL-15 0092), from the Knut & Alice Wallenberg Foundation (Wallenberg Academy Fellow, grant no 2016-0220) and from the Swedish Research Council (grant no 2018-05207) is greatly acknowledged.

This work was performed at the Division of Applied Chemistry and the Chalmers Material Analysis Laboratory (CMAL) at Chalmers Univerity of Technology, and partially at the Laboratorie de Chimie Physique et Microbiologie pour les Materiaux et l′Environnement (LCPME) in France.

I would like to thank my supervisor, Anna Martinelli for giving me the opportunity to conduct my PhD studies at her group and for providing a supportive and creative environment.

The help and fruitful discussions with Anna Martinelli, Neus Vilà, Antiope Lotsari, Alain Walcarius, Khalid Elamin, Lars Evenäs, and Elisabet Ahlberg are deeply appreciated and acknowledged.

I would also like to thank past and current members of the Martinelli group; Olesia, Khalid, Mohammad, Iqbaal, Eduardo, and Vandna. Also to friends and colleagues at the Division of Applied Chemistry. It is a pleasure to be surrounded with so many great people.

And huge, warm thanks to my family members, especially to Tibor, Vné (Ilona), Zorán, and to my friends, Kata, Gergő, Pati, André, Claudia, and Gio as well as to Eva and Lars for all the encouragment and support. Of course, I would like to express a special thank to my partner, Johan, whose kind and loving nature is a real gift.

References

[1] A. Triolo, O. Russina, H. J. Bleif and E. Di Cola, "Nanoscale segregation in room temperature ionic liquids", *Journal of Physical Chemistry B*, 2007, **111**, 4641–4644 (cit. on pp. 1, 6, 9, 13, 36).

[2] I. Abdurrokhman, K. Elamin, O. Danyliv, M. Hasani, J. Swenson and A. Martinelli, "Protic Ionic Liquids Based on the Alkyl-Imidazolium Cation: Effect of the Alkyl Chain Length on Structure and Dynamics", *Journal of Physical Chemistry B*, 2019, **123**, 4044–4054 (cit. on pp. 1, 6, 9, 11, 13, 36, 37, 46, 54).

[3] Y. Su, J. Yan, M. Li, M. Zhang and B. Mao, "Electric double layer of Au(100)/imidazolium-based ionic liquids interface: Effect of cation size", *Journal of Physical Chemistry C*, 2013, **117**, 205–212 (cit. on pp. 1, 4, 6, 7, 11, 47).

[4] J. Yang, C. Lian and H. Liu, "Chain length matters: Structural transition and capacitance of room temperature ionic liquids in nanoporous electrodes", *Chemical Engineering Science*, 2020, **227**, 115927 (cit. on pp. 1, 11, 12).

[5] M. N. Garaga, V. Dracopoulos, U. Werner-Zwanziger, J. W. Zwanziger, M. Maréchal, M. Persson, L. Nordstierna and A. Martinelli, "A long-chain protic ionic liquid inside silica nanopores: Enhanced proton mobility due to efficient self-assembly and decoupled proton transport", *Nanoscale*, 2018, **10**, 12337–12348 (cit. on pp. 1, 4, 7–10, 26, 27, 38, 40, 41, 44, 59).

[6] T. L. Greaves and C. J. Drummond, "Protic Ionic Liquids: Evolving Structure-Property Relationships and Expanding Applications", *Chemical Reviews*, 2015, **115**, 11379–11448 (cit. on pp. 1, 3, 4, 10).

[7] M. Hasani, L. M. Varela and A. Martinelli, "Short-Range Order and Transport Properties in Mixtures of the Protic Ionic Liquid [C2HIm][TFSI] with Water or Imidazole", *Journal of Physical Chemistry B*, 2020, **124**, 1767–1777 (cit. on pp. 1, 3, 4).

[8] J. Ingenmey, S. Gehrke and B. Kirchner, "How to Harvest Grotthuss Diffusion in Protic Ionic Liquid Electrolyte Systems", *ChemSusChem*, 2018, **11**, 1900–1910 (cit. on pp. 1, 3, 4).

[9] K. D. Kreuer, S. J. Paddison, E. Spohr and M. Schuster, “Transport in proton conductors for fuel-cell applications: Simulations, elementary reactions, and phenomenology”, *Chemical Reviews*, 2004, **104**, 4637–4678 (cit. on pp. 1, 4).

[10] Q. Su, Y. Qi, X. Yao, W. Cheng, L. Dong, S. Chen and S. Zhang, “Ionic liquids tailored and confined by one-step assembly with mesoporous silica for boosting the catalytic conversion of CO2 into cyclic carbonates”, *Green Chemistry*, 2018, **20**, 3232–3241 (cit. on pp. 1, 7).

[11] J. Dupont, “From molten salts to ionic liquids: A "nano" journey”, *Accounts of Chemical Research*, 2011, **44**, 1223–1231 (cit. on p. 3).

[12] I. Abdurrokhman, K. Elamin, O. Danyliv, M. Hasani, J. Swenson and A. Martinelli, “Protic Ionic Liquids Based on the Alkyl-Imidazolium Cation: Effect of the Alkyl Chain Length on Structure and Dynamics”, *Journal of Physical Chemistry B*, 2016, **9**, 1459–1464 (cit. on p. 3).

[13] R. E. Morris, “Ionothermal synthesis - Ionic liquids as functional solvents in the preparation of crystalline materials”, *Chemical Communications*, 2009, 2990–2998 (cit. on p. 3).

[14] R. Hayes, G. G. Warr and R. Atkin, “Structure and Nanostructure in Ionic Liquids”, *Chemical Reviews*, 2015, **115**, 6357–6426 (cit. on pp. 3, 5, 6, 9, 14).

[15] M. P. Singh, R. K. Singh and S. Chandra, “Ionic liquids confined in porous matrices: Physicochemical properties and applications”, *Progress in Materials Science*, 2014, **64**, 73–120 (cit. on pp. 3, 7–9).

[16] A. S. Amarasekara, “Acidic Ionic Liquids”, *Chemical Reviews*, 2016, **116**, 6133–6183 (cit. on pp. 3, 10).

[17] M. Yoshizawa, W. Xu and C. A. Angell, “Ionic Liquids by Proton Transfer: Vapor Pressure, Conductivity, and the Relevance of ΔpKa from Aqueous Solutions”, *Journal of the American Chemical Society*, 2003, **125**, 15411–15419 (cit. on p. 3).

[18] J. P. Belieres and C. A. Angell, “Protic ionic liquids: Preparation, characterization, and proton free energy level representation”, *Journal of Physical Chemistry B*, 2007, **111**, 4926–4937 (cit. on p. 4).

[19] N. Yaghini, V. Gómez-González, L. M. Varela and A. Martinelli, “Structural origin of proton mobility in a protic ionic liquid/imidazole mixture: Insights from computational and experimental results”, *Physical Chemistry Chemical Physics*, 2016, **18**, 23195–23206 (cit. on p. 4).

[20] R. Dutta, S. Kundu and N. Sarkar, “Ionic liquid-induced aggregate formation and their applications”, *Biophysical Reviews*, 2018, **10**, 861–871 (cit. on pp. 4, 6).

[21] H. Cao, Y. Hu, W. Xu, Y. Wang and X. Guo, "Recent progress in the assembly behavior of imidazolium-based ionic liquid surfactants", *Journal of Molecular Liquids*, 2020, **319**, 114354 (cit. on pp. 4, 6, 12).

[22] M. H. Anthofer, M. E. Wilhelm, M. Cokoja, I. I. Markovits, A. Pöthig, J. Mink, W. A. Herrmann and F. E. Kühn, "Cycloaddition of CO2 and epoxides catalyzed by imidazolium bromides under mild conditions: Influence of the cation on catalyst activity", *Catalysis Science and Technology*, 2014, **4**, 1749–1758 (cit. on p. 4).

[23] K. Goossens, K. Lava, C. W. Bielawski and K. Binnemans, "Ionic Liquid Crystals: Versatile Materials", *Chemical Reviews*, 2016, **116**, 4643–4807 (cit. on pp. 4, 6).

[24] A. Vioux and B. Coasne, "From Ionogels to Biredox Ionic Liquids: Some Emerging Opportunities for Electrochemical Energy Storage and Conversion Devices", *Advanced Energy Materials*, 2017, **7**, 1–13 (cit. on pp. 4, 7, 9).

[25] J. Łuczak, M. Paszkiewicz, A. Krukowska, A. Malankowska and A. Zaleska-Medynska, "Ionic liquids for nano- and microstructures preparation. Part 1: Properties and multifunctional role", *Advances in Colloid and Interface Science*, 2016, **230**, 13–28 (cit. on pp. 5, 14, 15).

[26] A. A. Pádua, M. F. Costa Gomes and J. N. Canongia Lopes, "Molecular solutes in ionic liquids: A structural perspective", *Accounts of Chemical Research*, 2007, **40**, 1087–1096 (cit. on pp. 6, 36).

[27] M. Blesic, M. H. Marques, N. V. Plechkova, K. R. Seddon, L. P. N. Rebelo and A. Lopes, "Self-aggregation of ionic liquids: Micelle formation in aqueous solution", *Green Chemistry*, 2007, **9**, 481–490 (cit. on p. 6).

[28] H. Abe, "Phase variety in ionic liquids: Hydrogen bonding and molecular conformations", *Journal of Molecular Liquids*, 2021, **332**, 115189 (cit. on p. 6).

[29] C. J. Bowlas, D. W. Bruceb and K. R. Seddon, "Liquid-crystalline ionic liquids", 1996, 1625–1626 (cit. on p. 6).

[30] M. Antonietti, D. Kuang, B. Smarsly and Y. Zhou, "Ionic liquids for the convenient synthesis of functional nanoparticles and other inorganic nanostructures", *Angewandte Chemie - International Edition*, 2004, **43**, 4988–4992 (cit. on pp. 6, 12).

[31] S. Vavra, N. Vilà, A. Lotsari, A. Walcarius and A. Martinelli, "An imidazolium ionic liquid as effective structure-directing agent for the fabrication of silica thin films with vertically aligned nanochannels", *Microporous and Mesoporous Materials*, 2020, DOI: 10.1016/j.micromeso.2020.110407 (cit. on pp. 6, 12, 14, 15, 25, 51).

[32] J. Zhang, Y. Ma, F. Shi, L. Liu and Y. Deng, "Room temperature ionic liquids as templates in the synthesis of mesoporous silica via a sol-gel method", *Microporous and Mesoporous Materials*, 2009, **119**, 97–103 (cit. on p. 7).

[33] Y. He, M. Tsutsui, Y. Zhou and X. S. Miao, "Solid-state nanopore systems: from materials to applications", *NPG Asia Materials*, 2021, **13**, 1–26 (cit. on p. 7).

[34] A. B. Grommet, M. Feller and R. Klajn, "Chemical reactivity under nanoconfinement", *Nature Nanotechnology*, 2020, **15**, 256–271 (cit. on p. 7).

[35] A. Zou and S. C. Maroo, "Nano-confinement effects on liquid pressure", *Physics of Fluids*, 2021, **33**, DOI: 10.1063/5.0044938 (cit. on p. 7).

[36] W. H. Thompson, "Perspective: Dynamics of confined liquids", *Journal of Chemical Physics*, 2018, **149**, DOI: 10.1063/1.5057759 (cit. on p. 7).

[37] C. Iacob, J. R. Sangoro, W. K. Kipnusu, R. Valiullin, J. Kärger and F. Kremer, "Enhanced charge transport in nano-confined ionic liquids", *Soft Matter*, 2012, **8**, 289–293 (cit. on pp. 7, 9, 10).

[38] X. Zhang, H. Liu and L. Jiang, "Wettability and Applications of Nanochannels", *Advanced Materials*, 2019, **31**, 1–32 (cit. on p. 7).

[39] S. Zhang, J. Zhang, Y. Zhang and Y. Deng, "Nanoconfined Ionic Liquids", *Chemical Reviews*, 2017, **117**, 6755–6833 (cit. on pp. 7–9).

[40] K. Yavir, Ł. Marcinkowski, R. Marcinkowska, J. Namieśnik and A. Kloskowski, "Analytical applications and physicochemical properties of ionic liquid-based hybrid materials: A review", *Analytica Chimica Acta*, 2019, **1054**, 1–16 (cit. on pp. 7, 12).

[41] J. Alemán, A. V. Chadwick, J. He, M. Hess, K. Horie, R. G. Jones, P. Kratochvíl, I. Meisel, I. Mita, G. Moad, S. Penczek and R. F. Stepto, "Definitions of terms relating to the structure and processing of sols, gels, networks, and inorganic-organic hybrid materials (IUPAC recommendations 2007)", *Pure and Applied Chemistry*, 2007, **79**, 1801–1829 (cit. on p. 7).

[42] J. Le Bideau, L. Viau and A. Vioux, "Ionogels, ionic liquid based hybrid materials", *Chemical Society Reviews*, 2011, **40**, 907–925 (cit. on p. 7).

[43] L. Pang, R. Pang, L. Ge, L. Zheng, J. Zhao and H. Zhang, "Trace determination of organophosphate esters in environmental water samples with an ionogel-based nanoconfined ionic liquid fiber coating for solid-phase microextraction with gas chromatography and flame photometric detection", *Journal of Separation Science*, 2016, **39**, 4415–4421 (cit. on p. 7).

[44] Y. He, M. Tsutsui, Y. Zhou and X. S. Miao, "Solid-state nanopore systems: from materials to applications", *NPG Asia Materials*, 2021, **13**, DOI: 10.1038/s41427-021-00313-z (cit. on p. 7).

[45] A. Walcarius, "Electroinduced Surfactant Self-Assembly Driven to Vertical Growth of Oriented Mesoporous Films", *Accounts of Chemical Research*, 2021, **54**, 3563–3575 (cit. on p. 7).

[46] M. D. Elola and J. Rodriguez, "Ionic Mobility within Functionalized Silica Nanopores", *Journal of Physical Chemistry C*, 2019, **123**, 3622–3633 (cit. on pp. 8, 9, 39, 44).

[47] C. Iacob, J. R. Sangoro, P. Papadopoulos, T. Schubert, S. Naumov, R. Valiullin, J. Kärger and F. Kremer, "Charge transport and diffusion of ionic liquids in nanoporous silica membranes", *Physical Chemistry Chemical Physics*, 2010, **12**, 13798–13803 (cit. on pp. 9, 10, 39, 44).

[48] M. N. Garaga, L. Aguilera, N. Yaghini, A. Matic, M. Persson and A. Martinelli, "Achieving enhanced ionic mobility in nanoporous silica by controlled surface interactions", *Physical Chemistry Chemical Physics*, 2017, **19**, 5727–5736 (cit. on pp. 9, 10, 38, 40, 44).

[49] M. N. Garaga, M. Persson, N. Yaghini and A. Martinelli, "Local coordination and dynamics of a protic ammonium based ionic liquid immobilized in nano-porous silica micro-particles probed by Raman and NMR spectroscopy", *Soft Matter*, 2016, **12**, 2583–2592 (cit. on p. 9).

[50] S. Pan, M. Yao, J. Zhang, B. Li, C. Xing, X. Song, P. Su and H. Zhang, "Recognition of Ionic Liquids as High-Voltage Electrolytes for Supercapacitors", *Frontiers in Chemistry*, 2020, **8**, 1–18 (cit. on pp. 10, 11).

[51] T. Stettner and A. Balducci, "Protic ionic liquids in energy storage devices: past, present and future perspective", *Energy Storage Materials*, 2021, **40**, 402–414 (cit. on p. 10).

[52] M. Salanne, "Ionic Liquids for Supercapacitor Applications", *Topics in Current Chemistry*, 2017, **375**, 1–25 (cit. on p. 11).

[53] M. V. Fedorov and A. A. Kornyshev, "Ionic liquids at electrified interfaces", *Chemical Reviews*, 2014, **114**, 2978–3036 (cit. on pp. 11, 47).

[54] M. Z. Bazant, B. D. Storey and A. A. Kornyshev, "Double layer in ionic liquids: Overscreening versus crowding", *Physical Review Letters*, 2011, **106**, 6–9, arXiv: 1010.3490 (cit. on pp. 11, 47).

[55] H. Zhong, F. Xu, Z. Li, R. Fu and D. Wu, "High-energy supercapacitors based on hierarchical porous carbon with an ultrahigh ion-accessible surface area in ionic liquid electrolytes", *Nanoscale*, 2013, **5**, 4678–4682 (cit. on p. 11).

[56] C. Largeot, C. Portet, J. Chmiola, P. L. Taberna, Y. Gogotsi and P. Simon, "Relation between the ion size and pore size for an electric double-layer capacitor", *Journal of the American Chemical Society*, 2008, **130**, 2730–2731 (cit. on pp. 11, 46).

[57] Y. Zhou and M. Antonietti, "Preparation of highly ordered monolithic super-microporous lamellar silica with a room-temperature ionic liquid as template via the nanocasting technique", *Advanced Materials*, 2003, **15**, 1452–1455 (cit. on pp. 12, 15).

[58] R. Ciriminna, A. Fidalgo, V. Pandarus, F. Béland, L. M. Ilharco and M. Pagliaro, "The sol-gel route to advanced silica-based materials and recent applications", *Chemical Reviews*, 2013, **113**, 6592–6620 (cit. on p. 12).

[59] C. J. Brinker and G. W. Scherer, "Particulate Sols and Gels", *Sol-Gel Science*, 1990, 234–301 (cit. on pp. 12, 13).

[60] T. Montheil, J. Martinez and G. Subra, "Inorganic polymerization : an attractive route to biocompatible hybrid hydrogels", 2018, 3434–3448 (cit. on p. 13).

[61] H. Kaper and B. Smarsly, "Templating and phase behaviour of the long chain ionic liquid C 16mimCl", *Zeitschrift fur Physikalische Chemie*, 2006, **220**, 1455–1471 (cit. on pp. 13–15).

[62] Y. Zhou, J. H. Schattka and M. Antonietti, "Room-temperature ionic liquids as template to monolithic mesoporous silica with wormlike pores via a sol-gel nanocasting technique", *Nano Letters*, 2004, **4**, 477–481 (cit. on pp. 13, 14).

[63] A. Vioux, L. Viau, S. Volland and J. Le Bideau, "Use of ionic liquids in sol-gel; ionogels and applications", *Comptes Rendus Chimie*, 2010, **13**, 242–255 (cit. on p. 14).

[64] M. Nayeri, K. Nygård, M. Karlsson, M. Maréchal, M. Burghammer, M. Reynolds and A. Martinelli, "The role of the ionic liquid C6C1ImTFSI in the sol-gel synthesis of silica studied using in situ SAXS and Raman spectroscopy", *Physical Chemistry Chemical Physics*, 2015, **17**, 9841–9848 (cit. on p. 14).

[65] H. Zhang and S. Liu, "Preparation of ordered mesoporous silica materials templated by ionic liquids in alkaline condition", *Journal of Porous Materials*, 2019, **26**, 1–6 (cit. on pp. 14, 15).

[66] T. Wang, H. Kaper, M. Antonietti and B. Smarsly, "Templating behavior of a long-chain ionic liquid in the hydrothermal synthesis of mesoporous silica", *Langmuir*, 2007, **23**, 1489–1495 (cit. on pp. 14, 15).

[67] Y. Zhou and M. Antonietti, "A Series of Highly Ordered, Super-Microporous, Lamellar Silicas Prepared by Nanocasting with Ionic Liquids", *Chemistry of Materials*, 2004, **16**, 544–550 (cit. on p. 15).

[68] M. Etienne, Y. Guillemin, D. Grosso and A. Walcarius, "Electrochemical approaches for the fabrication and/or characterization of pure and hybrid templated mesoporous oxide thin films: A review", *Analytical and Bioanalytical Chemistry*, 2013, **405**, 1497–1512 (cit. on pp. 15, 16).

[69] A. Walcarius and A. Kuhn, "Ordered porous thin films in electrochemical analysis", *TrAC - Trends in Analytical Chemistry*, 2008, **27**, 593–603 (cit. on p. 15).

[70] G. Herzog, E. Sibottier, M. Etienne and A. Walcarius, "Electrochemically assisted self-assembly of ordered and functionalized mesoporous silica films: Impact of the electrode geometry and size on film formation and properties", *Faraday Discussions*, 2013, **164**, 259–273 (cit. on pp. 15, 16).

[71] M. Etienne, A. Goux, E. Sibottier and A. Walcarius, "Oriented mesoporous organosilica films on electrode: A new class of nanomaterials for sensing", *Journal of Nanoscience and Nanotechnology*, 2009, **9**, 2398–2406 (cit. on p. 16).

[72] G. H. Michler, *Electron Microscopy of Polymers*, Springer-Verlag GmbH, Germany, 2008 (cit. on p. 17).

[73] Philip Willmott, *An introduction to synchrotron radiation : techniques and applications*, John Wiley & Sons Ltd, Chichester, 2nd (cit. on p. 18).

[74] H. Schnablegger and Y. Singh, *The SAXS Guide*, Anton Paar GmbH, Graz, 2011 (cit. on pp. 18, 19).

[75] C. S. Kumar, *X-ray and Neutron Techniques for Nanomaterials Characterization*, Springer-Verlag GmbH, Germany, Berlin, 2016 (cit. on p. 19).

[76] S. Hudson, D. A. Tanner, W. Redington, E. Magner, K. Hodnett and S. Nakahara, "Quantitative TEM analysis of a hexagonal mesoporous silicate structure", *Physical Chemistry Chemical Physics*, 2006, **8**, 3467–3474 (cit. on p. 20).

[77] H. J. Chang, T. Y. Chen, Z. P. Zhao, Z. J. Dai, Y. L. Chen, C. Y. Mou and Y. H. Liu, "Ordered Mesoporous Zeolite Thin Films with Perpendicular Reticular Nanochannels of Wafer Size Area", *Chemistry of Materials*, 2018, **30**, 8303–8313 (cit. on p. 20).

[78] M. Thommes, K. Kaneko, A. V. Neimark, J. P. Olivier, F. Rodriguez-Reinoso, J. Rouquerol and K. S. Sing, "Physisorption of gases, with special reference to the evaluation of surface area and pore size distribution (IUPAC Technical Report)", *Pure and Applied Chemistry*, 2015, **87**, 1051–1069 (cit. on p. 20).

[79] P. J. d. P. Atkins, *Physical Chemistry*, W. H. Freeman and Company, New York, 9th edn., 2010 (cit. on pp. 20, 23).

[80] H. Seyama, M. Soma and B. K. Theng, "X-Ray Photoelectron Spectroscopy", *Developments in Clay Science*, 2013, **5**, 161–176 (cit. on p. 22).

[81] Donald L. Pavia, P. Lampman, K. Vyvyan, D. L. Pavia and G. S. Kriz, *Introduction to Spectroscopy*, Brooks/Cole, Cengage Learning, 4th, 2009 (cit. on pp. 23, 32, 33).

[82] M. Tasumi and A. Sakamoto, *Introduction to Experimental Infrared Spectroscopy : Fundamentals and Practical Methods*, John Wiley & Sons Ltd, 2015 (cit. on p. 24).

[83] P. Larkin, *Infrared and Raman Spectroscopy*, Elsevier, 2011 (cit. on p. 25).

[84] N. Elgrishi, K. J. Rountree, B. D. McCarthy, E. S. Rountree, T. T. Eisenhart and J. L. Dempsey, "A Practical Beginner's Guide to Cyclic Voltammetry", *Journal of Chemical Education*, 2018, **95**, 197–206 (cit. on pp. 27, 28).

[85] C. Karman, N. Vilà and A. Walcarius, "Amplified Charge Transfer for Anionic Redox Probes through Oriented Mesoporous Silica Thin Films", *ChemElectroChem*, 2016, **3**, 2130–2137 (cit. on pp. 27, 28, 54, 55).

[86] V. F. Lvovich, *Impedance Spectroscopy Applications o Electrochemical and Dielectric Phenomena*, John Wiley & Sons , Inc ., 2012 (cit. on pp. 29–31).

[87] W. H. Woodward, "Broadband Dielectric Spectroscopy - A Practical Guide", *ACS Symposium Series*, 2021, **1375**, 3–59 (cit. on pp. 30, 31).

[88] M. Shojaatalhosseini, K. Elamin and J. Swenson, "Conductivity - Relaxation Relations in Nanocomposite Polymer Electrolytes Containing Ionic Liquid", *Journal of Physical Chemistry B*, 2017, **121**, 9699–9707 (cit. on p. 30).

[89] B. Hirschorn, M. E. Orazem, B. Tribollet, V. Vivier, I. Frateur and M. Musiani, "Determination of effective capacitance and film thickness from constant-phase-element parameters", *Electrochimica Acta*, 2010, **55**, 6218–6227 (cit. on pp. 31, 44, 45).

[90] J. M. McIntyre and H. Q. Pham, "Electrochemical impedance spectroscopy; a tool for organic coatings optimizations", *Progress in Organic Coatings*, 1996, **27**, 201–207 (cit. on p. 31).

[91] T. D. Claridge, *High-Resolution NMR Techniques in Organic Chemistry*, Elsevier, 1999 (cit. on pp. 32, 33).

[92] E. O. Stejskal and J. E. Tanner, "Spin diffusion measurements: Spin echoes in the presence of a time-dependent field gradient", *The Journal of Chemical Physics*, 1965, **42**, 288–292 (cit. on p. 33).

[93] O. Russina, A. Triolo, L. Gontrani and R. Caminiti, "Mesoscopic structural heterogeneities in room-temperature ionic liquids", *Journal of Physical Chemistry Letters*, 2012, **3**, 27–33 (cit. on p. 36).

[94] A. Martinelli, M. Maréchal, Å Östlund and J. Cambedouzou, "Insights into the interplay between molecular structure and diffusional motion in 1-alkyl-3-methylimidazolium ionic liquids: A combined PFG NMR and X-ray scattering study", *Physical Chemistry Chemical Physics*, 2013, **15**, 5510–5517 (cit. on pp. 37, 54).

[95] M. Nayeri, M. T. Aronson, D. Bernin, B. F. Chmelka and A. Martinelli, "Surface effects on the structure and mobility of the ionic liquid C 6C1ImTFSI in silica gels", *Soft Matter*, 2014, **10**, 5618–5627 (cit. on pp. 37, 38).

[96] A. Martinelli, A. Matic, P. Johansson, P. Jacobsson, L. Börjesson, A. Fernicola, S. Panero, B. Scrosati and H. Ohno, "Conformational evolution of TFSI- in protic and aprotic ionic liquids", *Journal of Raman Spectroscopy*, 2011, **42**, 522–528 (cit. on p. 37).

[97] A. Gibaud, A. Baptiste, D. A. Doshi, C. J. Brinker, L. Yang and B. Ocko, "Wall thickness and core radius determination in surfactant templated silica thin films using GISAXS and X-ray reflectivity", *Europhysics Letters*, 2003, **63**, 833–839 (cit. on p. 38).

[98] C. Despas, N. A. Vodolazkaya, J. Ghanbaja and A. Walcarius, "Preparation of ordered and oriented mesoporous silica thin films bearing octyl or hexadecyl groups by electrochemically assisted self-assembly and evaluation of their transport properties", *Journal of Solid State Electrochemistry*, 2015, **19**, 2075–2085 (cit. on p. 38).

[99] A. Goux, M. Etienne, E. Aubert, C. Lecomte, J. Ghanbaja and A. Walcarius, "Oriented mesoporous silica films obtained by electro-assisted self-assembly (EASA)", *Chemistry of Materials*, 2009, **21**, 731–741 (cit. on pp. 38, 54, 56, 57).

[100] M. N. Garaga, M. Persson, N. Yaghini and A. Martinelli, "Local coordination and dynamics of a protic ammonium based ionic liquid immobilized in nano-porous silica micro-particles probed by Raman and NMR spectroscopy", *Soft Matter*, 2016, **12**, 2583–2592 (cit. on pp. 39, 44).

[101] M. Nayeri, M. T. Aronson, D. Bernin, B. F. Chmelka and A. Martinelli, "Surface effects on the structure and mobility of the ionic liquid C 6C1ImTFSI in silica gels", *Soft Matter*, 2014, **10**, 5618–5627 (cit. on p. 39).

[102] P. Sippel, P. Lunkenheimer, S. Krohns, E. Thoms and A. Loidl, "Importance of liquid fragility for energy applications of ionic liquids", *Scientific Reports*, 2015, **5**, 1–8 (cit. on p. 41).

[103] S. Vavra, K. Elamin, L. Evenäs and A. Martinelli, "Transport Properties and Local Structure of an Imidazole/Protic Ionic Liquid Mixture Confined in the Mesopores of Hydrophobic Silica", *Journal of Physical Chemistry C*, 2021, **125**, 2607–2618 (cit. on p. 45).

[104] A. Rybinska-Fryca, A. Sosnowska and T. Puzyn, "Prediction of dielectric constant of ionic liquids", *Journal of Molecular Liquids*, 2018, **260**, 57–64 (cit. on p. 46).

[105] X. Lu, G. Burrell, F. Separovic and C. Zhao, "Electrochemistry of room temperature protic ionic liquids: A critical assessment for use as electrolytes in electrochemical applications", *Journal of Physical Chemistry B*, 2012, **116**, 9160–9170 (cit. on p. 46).

[106] Q. Yang, Z. Zhang, X. G. Sun, Y. S. Hu, H. Xing and S. Dai, "Ionic liquids and derived materials for lithium and sodium batteries", *Chemical Society Reviews*, 2018, **47**, 2020–2064 (cit. on p. 46).

[107] X. Q. Zhang, A. H. Lu, Q. Sun, X. F. Yu, J. Y. Chen and W. C. Li, "Unconventional Synthesis of Large Pore Ordered Mesoporous Carbon Nanospheres for Ionic Liquid-Based Supercapacitors", *ACS Applied Energy Materials*, 2018, **1**, 5999–6005 (cit. on p. 46).

[108] P. Wu, J. Huang, V. Meunier, B. G. Sumpter and R. Qiao, "Complex capacitance scaling in ionic liquids-filled nanopores", *ACS Nano*, 2011, **5**, 9044–9051 (cit. on p. 46).

[109] Z. Lian, H. Chao and Z. G. Wang, "Effects of Confinement and Ion Adsorption in Ionic Liquid Supercapacitors with Nanoporous Electrodes", *ACS Nano*, 2021, **15**, 11724–11733 (cit. on p. 46).

[110] X. Mao, P. Brown, C. Červinka, G. Hazell, H. Li, Y. Ren, D. Chen, R. Atkin, J. Eastoe, I. Grillo, A. A. Padua, M. F. Costa Gomes and T. A. Hatton, "Self-assembled nanostructures in ionic liquids facilitate charge storage at electrified interfaces", *Nature Materials*, 2019, **18**, 1350–1357 (cit. on p. 47).

[111] P. Innocenzi, "Infrared spectroscopy of sol â€" gel derived silica-based films : a spectra-microstructure overview", *Journal of Non-Crystalline Solids*, 2003, **316**, 309–319 (cit. on p. 50).

[112] R. Lenza and W. Vasconcelos, "Structural evolution of silica sols modified with formamide", *Materials Research*, 2001, **4**, 175–179 (cit. on p. 50).

[113] E. M. Björk, P. Mäkie, L. Rogström, A. Atakan, N. Schell and M. Odén, "Formation of block-copolymer-templated mesoporous silica", *Journal of Colloid and Interface Science*, 2018, **521**, 183–189 (cit. on pp. 50, 51).

[114] S. Portal and R. M. Almeida, "Variable incidence infrared absorption spectroscopy of gel-derived silica and titania films", *Physica Status Solidi (A) Applied Research*, 2004, **201**, 2941–2947 (cit. on p. 50).

[115] J. Choi, I. Gunkel, Y. Li, Z. Sun, F. Liu, H. Kim, K. R. Carter and T. P. Russell, "Macroscopically ordered hexagonal arrays by directed self-assembly of block copolymers with minimal topographic patterns", *Nanoscale*, 2017, **9**, 14888–14896 (cit. on p. 51).

[116] Y. Guillemin, M. Etienne, E. Aubert and A. Walcarius, "Electrogeneration of highly methylated mesoporous silica thin films with vertically-aligned mesochannels and electrochemical monitoring of mass transport issues", *Journal of Materials Chemistry*, 2010, **20**, 6799–6807 (cit. on pp. 51, 52, 57).

[117] M. Zienkiewicz-Strzałka, M. Skibińska and S. Pikus, "Small-angle X-ray scattering (SAXS) studies of the structure of mesoporous silicas", *Nuclear Instruments and Methods in Physics Research, Section B: Beam Interactions with Materials and Atoms*, 2017, **411**, 72–77 (cit. on p. 51).

[118] E. Sibottier, S. Sayen, F. Gaboriaud and A. Walcarius, "Factors affecting the preparation and properties of electrodeposited silica thin films functionalized with amine or thiol groups", *Langmuir*, 2006, **22**, 8366–8373 (cit. on p. 55).

[119] A. Walcarius, E. Sibottier, M. Etienne and J. Ghanbaja, "Electrochemically assisted self-assembly of mesoporous silica thin films", *Nature Materials*, 2007, **6**, 602–608 (cit. on p. 56).

[120] S. Ahoulou, N. Vilà, S. Pillet, D. Schaniel and A. Walcarius, "Coordination Polymers as Template for Mesoporous Silica Films: A Novel Composite Material Fe(Htrz)3@SiO2 with Remarkable Electrochemical Properties", *Chemistry of Materials*, 2019, **31**, 5796–5807 (cit. on pp. 56, 57).